Performance Enhancement of Organic Photovoltaic Cells through Nanostructuring and Molecular Doping

Dissertation

zur Erlangung des akademischen Grades

d o c t o r r e r u m n a t u r a l i u m

(Dr. rer. nat.)

im Fach Physik

eingereicht an der

Mathematisch-Naturwissenschaftlichen Fakultät

der Humboldt-Universität zu Berlin

von

Herrn M.S.-Physik Shuwen Yu

Präsident der Humboldt-Universität zu Berlin
Prof. Dr. Jan-Hendrik Olbertz

Dekan der Mathematisch-Naturwissenschaftlichen Fakultät
Prof. Dr. Elmar Kulke

Gutachter/innen: 1. Prof. Norbert Koch
2. Prof. Beate Röder
3. Prof. Dieter Neher

Tag der mündlichen Prüfung: 27.02.2015

Abstract

The present work mainly focuses on improving the performance of OPVCs by tailoring the donor-acceptor interface geometry and by tuning the electrical properties of interfaces with p-type molecular doping.

Crystalline and uniform nanocolumns of pentacene (PEN) and diindenoperylene (DIP) were fabricated by glancing angle deposition (GLAD), forming an interdigitated donor/acceptor heterojunction with [6,6]-phenyl-C_{61}-butyric acid methyl ester (PCBM) and/or fullerene as the electron acceptor. The short circuit current of nanocolumn-based OPVCs increased significantly compared to planar heterojunction OPVCs made from the same materials. The performance improvement of OPVCs had been verified to be contributed decisively by the donor-acceptor interface area enlargement because of reduced impact of short exciton diffusion length in organic materials.

P-type molecular doping as applied in polyfuran (PF) based OPVCs was investigated by using tetrafluorotetracyanoquinodimethane (F4-TCNQ) as the dopant for various doping ratios. Ultraviolet photoelectron spectroscopy (UPS) was applied to analyze the energy level shift with increasing doping ratio leading to the enlargement of the open circuit voltage in OPVCs, from 0.2 V to close to 0.4 V. Combining this observation with the results of doped polymer films, their morphology and absorption behavior, a net dipole pointing towards the donor material at the donor-acceptor interface of OPVCs is proposed. Overall, this work demonstrates the potential of both the GLAD technique and molecular electrical doping for improving the performance of OPVCs.

Keywords: organic photovoltaic cells, glancing angle deposition, nanocolumn structure, donor/acceptor interface, molecular doping

Kurzfassung

Die vorliegende Arbeit beschäftigt sich mit der Leistungssteigerung organischer Solarzellen durch Änderung der Geometrie an der Donor-Akzeptor Grenzfläche und dem Einstellen der elektronischen Eigenschaften von Grenzflächen durch molekulares p-Dotieren.

Kristalline und gleichmäßige Nanosäulen aus dem organischen Halbleiter Pentazen wurden durch glancing angle deposition (GLAD) hergestellt, die einen ineinandergreifenden Heteroübergang zu Methanofulleren [6,6]-Phenyl-C_{61}-Butansäure Methylester (PCBM) als Akzeptor ermöglichten. Die Kurzschlussspannung der nanosäulenbasierten Solarzellen war signifikant erhöht im Vergleich zu planaren Heteroübergängen zwischen denselben Materialien. Die Leistungssteigerung der Solarzellen konnte maßgebend der vergrößerten Grenzfläche zugewiesen werden, wegen des verringerten Einflusses der kurzen Exciton Diffusionslänge.

Molekulares p-Dotieren mit Tetrafluorotetracyanoquinodimethan (F4TCNQ) als Dotand in polyfuranbasierten Solarzellen wurde für verschiede Dotierkonzentrationen untersucht. Ultraviolettphotoelektronenspektroskopie wurde verwendet, um die Veränderungen der Energieniveaus mit zunehmender Dotierkonzentration zu analysieren, welche zu einer Vergrößerung der 0,2 V Kurzschlussspannung auf bis zu 0,4 V führte. Nach Kombination dieser Beobachtung mit Ergebnissen an dotierten Polymerfilmen, insbesondere bezüglich deren Morphologie und Absorptionsverhalten, wurde vorgeschlagen, dass ein resultierender Dipol an der Donor-Akzeptorgrenzfläche präsent ist. Zusammenfassend zeigt die vorliegende Arbeit das Potential sowohl der GLAD Technik als auch des molekularen, elektrischen Dotierens für die Leistungsverbesserung organischer Solarzellen

Stichwörter: organische Solarzellen, glancing angle deposition, Nanosäulen Donor-Akzeptorgrenzfläche, molekulares Dotieren

Contents

Chapter 1

Introduction

The industrial revolution brought human beings advanced technologies and new life styles, but at the same time, it also led to high-energy consumption. Every day people are becoming more aware of the crucial requirement for sustainable energy production in order to maintain daily activities. Since the world became fully aware of the shortage of natural fossil fuels, the development of global warming and the associated pollution of the environment, renewable and low pollution substitutes have been actively sought. Solar energy is one of the most abundant renewable energy resources. With an estimated 885 million TWh reaching the Earth's surface every year, this form of energy would go a long way towards satisfying the world's enormous energy needs. Furthermore, the conversion of solar energy to electricity is carbon-free and harmless to the environment. Hence, solar energy is considered as a favorite candidate for replacing traditional fossil fuel energy production. In order to utilize solar energy efficiently, improvement of power conversion efficiency (PCE) in photovoltaic (PV) cells is necessary. Nowadays, great efforts have been made to do so for organic and inorganic PV cells, from lab research to industrial manufacturing. The laboratory records of solar cell PCE are 44.7% and 12% for inorganic and organic PV cells respectively.[Green, 2014] However, the price of PV generated electricity is still not low enough to replace other energy resources. Therefore, lower price for high conversion efficiency, long lifetime and stable PV cells will be the research focus right now and in future.

Organic photovoltaic cells have a strong potential to complement the usage of solar energy inorganic PV cells, owing to their advantages such as the possible fabrication on flexible substrates and large-scale surfaces. Furthermore, they usually possess high absorption and the huge variety of tailoring materials with optimized optical and electrical properties could cover the entire visible light range and even the infrared region. Printing techniques have facilitated low-cost manufactories. Besides, the research of OPVCs is also inspired by the development of organic light emitting diodes that are used in mobile phone displays.

The first generation of OPVCs comprised of a single organic semiconductor layer with two metal electrodes referred to as a sandwich structure. The PCE of these devices was less than 1% as a result of the low dielectric constant of organic semiconductors.[Ghosh, 1973, Tang, 1975] In 1979, C.W. Tang presented the concept of the planar heterojunction OPVCs (Fig.1.1a) employing copper phthalocyanine as an absorber and perylene carboxylic derivative to assist the excitons separation.[Tang, 1986, Tang, 1979] Soon the PCE of heterojunction OPVCs reached 2% with different organic semiconductors. Later in 1992, bulk heterojunction OPVCs (Fig.1.1b) made from solution processing were reported by Sariciftci

et al.[Sariciftci, 1992] The principle involved the mixing of the donor and acceptor materials in solution, making a donor-acceptor blend structure that could solve the problem of short exciton lifetime. Nowadays, PCE of bulk heterojunction OPVCs can exceed 10%.[You, 2013a, You, 2013b, Green, 2013] The current record in PCE is 12% as Heliatek reported in 2012. However, unlike for inorganic PV cells, there are still many unsolved problems of OPVCs, such as issues with doping mechanisms in organic semiconductors. Therefore, further research may lead to further improvements in the PCE of OPVCs.

Energy conversion in OPVCs comprises of four processes: (I) the generation of excitons (electron-hole pairs) by light absorption (exciton generation rate: η_A), (II) excitons diffusion to donor-acceptor interface, (III) dissociation at the donor-acceptor interface (exciton dissociation efficiency: η_{ED}) and (IV) dissociated charges transported to respective electrodes and collected as output photocurrent (charge transfer efficiency: η_{CT} and charge collection efficiency: η_{CC}). The internal quantum efficiency η_{IQE} can be described by the expression:

$$\eta_{IQE} = \eta_A \cdot \eta_{ED} \cdot \eta_{CT} \cdot \eta_{CC} \tag{1.1}$$

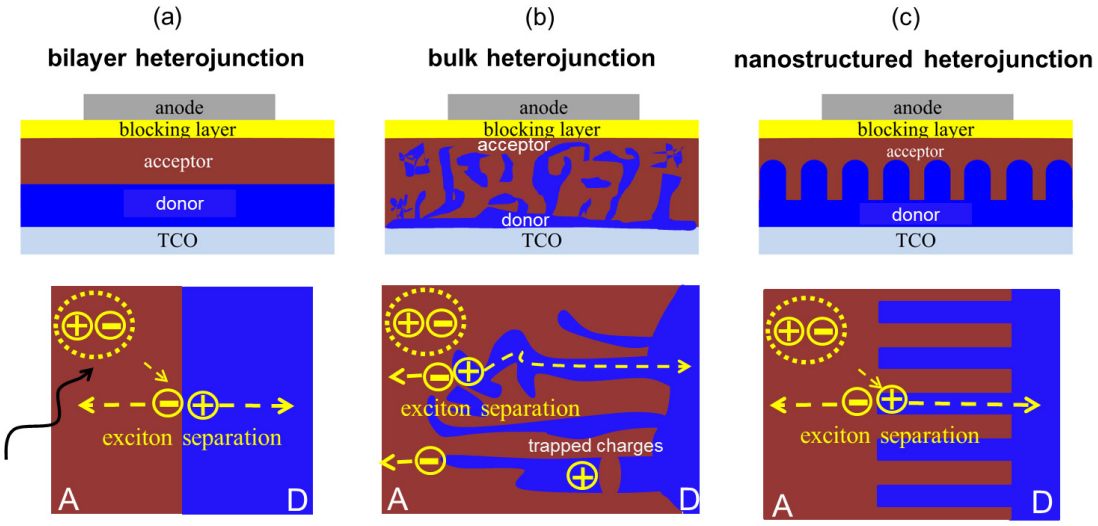

Fig.1.1 Schematic representation of OPVCs with bilayer heterojunction (a), bulk heterojunction (b) and vertically aligned nanostructured heterojunction devices (c) and their donor-acceptor interfaces configuration respectively including exciton creation and dissociation processing. Plus (+) denotes positive charge; minus (-) denotes negative charge; dot-line circled plus and minus denotes electron-hole pairs. A denotes electron acceptor; D denotes electron donor; yellow dash-line arrows denote the charges transport pass way.

The external quantum efficiency η_{EQE} is given as

$$\eta_{EQE} = (1 - R)\eta_{IQE} \tag{1.2}$$

where R is the reflectivity of the substrate-air interface.

In principle, each of these efficiencies suggests an individual route for device optimization. However, the improvement of either efficiency may lead to a decrease in the other. Indeed, the most critical two steps for the energy conversion of OPVCs are light absorption and exciton dissociation. Considering the numerous species of synthesized organic materials it is not difficult to improve the light absorption efficiency of OPVCs by exploring new organic materials with large absorption co-efficiency and small band gap. The exciton dissociation in fact includes two steps: exciton diffusion (L_D) and dissociation, and η_{ED} can be limited in both steps. In addition, there is an inherent tradeoff between the light absorption (thickness dependent) and exciton diffusion efficiency. In order to solve the conflict, besides utilizing new organic materials with large exciton diffusion length (for instance highly ordered crystalline structure), an alternative option is employing more sophisticated device architectures such as metal-organic-metal sandwich structures, bilayer heterojunction structures and bulk heterojunction structures.[Tang, 1975, Tang, 1986, Yu, 1995] With these state of the art structures, outstanding improvement of PCE has been achieved. The introduction of the heterojunction concept in OPVCs was inspired by inorganic solar cells, creating an electron-donor/electron-acceptor interface in the vicinity of which exciton dissociation has been verified. In the manner of a PN junction, recombination of dissociated charges was hindered and consequently, the exciton dissociation efficiency was increased. However, for many organic semiconductors, their exciton diffusion length was shorter than the active absorber thickness. A large fraction of photogenerated excitons recombined before they were transported to the donor/acceptor interface. As a result, the exciton diffusion efficiency was limited. In this stage, the trade-off between absorption and exciton dissociation efficiency became the obstacle towards improving the PCE of OPVCs. Later, the breakthrough of PCE was implemented by employing bulk heterojunction as shown in Fig1.1b, in which the interpenetrating network of donor/acceptor structure was achieved through the phase separation of the mixture of donor and acceptor polymers. Two main advantages of this structure are i) enlarged the donor/acceptor interface area and ii) reducing the limitation of short exciton diffusion length when increasing absorber thickness to absorb more light. Furthermore, the bulk heterojunction could also be fabricated with vacuum deposition (co-deposition) with conjugated molecules, which has been demonstrated as a successful approach for improving the PCE of OPVCs.[Wagner, 2010, Gruber, 2013, Xiao, 2013] Nevertheless, there are still unavoidable problems impeding further performance improvement like low charge-carrier mobility, exciton quenching and morphological issues such as dead-ends in the conduction pathway. Recently, an idealized bulk heterojunction comprising crystalline, vertically aligned ordered nanostructure was applied to overcome those limitations. As shown in Fig.1.1c, well controlled nanocolumns could also create the interdigitated and laterally structured configuration of separate donor/acceptor phases, and the contorted and resistive conducting pathway occurring in bulk heterojunction architecture could be eliminated successfully.[Lunt, 2011, Yu, 2011] In addition, the morphological characteristics of donor and acceptor are independent, meaning there is negligible concern with the phase separation processing and it is possible to quantitatively evaluate the influence of interface area.

The leitmotif of this work is the optimization of the bilayer heterojunction device architecture, more specifically the donor-acceptor interface of OPVCs in order to improve the PCE using two different approaches. The first approach involves increasing the short circuit current (J_{sc}) via maximizing the active donor-acceptor interface area by growing a columnar structure using glancing angle deposition (GLAD) in a vacuum. By using appropriate deposition parameters pentacene (PEN) and diindenoperylene (DIP) grow in nanocolumn structures on ITO or PEDOT:PSS coated ITO substrates. The interdigitated donor-acceptor structure of OPVCs is realized by spin coating PCBM on top of PEN columns or depositing C60 on top of DIP columns structure respectively. The second approach requires the enlargement of the open circuit voltage (V_{oc}) by tuning the energy level alignment through molecular doping. The doping process is achieved by mixing the strong dopant small molecule F4-TCNQ with polyfuran in THF solvent with different monomer ratios. The OPVCs based on doped polyfuran films are realized by depositing C60 on top. Taking into consideration the results of morphology, electrical and optical properties of the doped polyfuran layer, the increase of V_{oc} in these OPVCs is proposed that originates from a net interface dipole raising the photovoltaic gap which directly impacts the value of V_{oc}.

The organization of this work is as follows. Chapter 2 starts with an overview of the fundamental properties of conjugated organic semiconductors and aspects of the basic principles of charge carrier transport, doping and film formation. After that, an overview of OPVCs operation principles is presented and the methods used to analyze the performance of OPVCs are also outlined. In chapter 3, the principles of the experimental methods like spin coating and GLAD are described. Additional experimental analysis methods and facilities such as scanning electron microscopy (SEM), scanning force microscopy (SFM) and ultraviolet/visible absorption (UV-VIS) spectroscopy will be covered. Furthermore, section 3.2 will outline the materials used in this work including organic materials, electrode and substrates.

In Chapter 4 the experimental results and discussion will be presented. In section 4.1, firstly the morphology of pentacene columnar structure prepared by GLAD is investigated by SEM. By manipulating the experimental parameters, a vertically aligned, homogeneous crystalline pentacene columnar structure on ITO substrate is made to form interdigitated heterojunction combined with PCBM as acceptor spin-coated. Compared with planar bi-layer structure, the interface area of interdigitated structure is successfully enlarged owing to the infiltration of PCBM into the gaps of pentacene nanocolumn as revealed by SEM results. The OPVCs is fabricated based on the columnar pentacene/PCBM heterojunction and the J-V performance is measured in the vacuum. With regard to the performance of OPVCs employing pentacene columnar structure, the J_{sc} is significantly increased matching expectations. The remarkable improvement of J-V characteristics verifies that utilizing vertical aligned columnar structure can effectively improve the performance of OPVCs by maximizing the donor-acceptor interface area and eliminating charge transport and exciton diffusion bottlenecks. Although the preparation of the perfectly interdigitated heterojunction

via vacuum depositing C60 as the acceptor was fail, it motivated further study of optimized nanocolumn morphology.

Section 4.2 presents different morphological properties of vertically aligned nanocolumn structure with another molecule diindenoperylene grown by GLAD, as well as its application in OPVCs. AFM and SEM were used to quantitatively analyze the donor/acceptor interface area and evaluate the quality of the interdigitated heterojunction. X-ray diffraction and ultraviolet/visible absorption spectroscopy were carried out to help identify the DIP molecular orientations. In comparison to bilayer heterojunction devices, the power conversion efficiency of OPVCs employing DIP columnar structure is increased, despite the fact that the DIP volume in columnar structured OPVCs is much less as shown from the quantitative analysis of absorption spectra. The performance improvement of OPVCs can be linked to both the enlarged donor-acceptor interface area and the enhanced light absorption.

Section 4.3 presents another promising method: doping, to improve the characteristics of OPVCs. The morphological, optical and electrical properties of pristine and F4-TCNQ doped polyfuran are studied with AFM, ultraviolet/visible absorption spectroscopy and ultraviolet photoelectron spectroscopy respectively. The conductivities of doping polyfuran are also investigated. Polyfuran with different F4-TCNQ doping percentage as electron donor is used to fabricate OPVCs with fullerene acting as the acceptor. Upon increasing the doping ratio, the photovoltaic gap of OPVCs is increased significantly, resulting in larger V_{oc}, as verified by UPS results. This phenomenon might be induced by net dipoles between doping polyfuran and fullerene with a positive end at polyfuran. At the end, doping polyfuran as an electron transport layer is used in OPVCs to assist in optimizing the performance of OPVCs based on ZnPc/C60. Through successfully eliminating the S-shape of devices based on ZnPc/C60 heterojunction and additional absorption in blue region, the power conversion efficiency has been improved remarkably.

Chapter 5 gives a summary of this work and an outlook on further work.

Chapter 2

Fundamentals

In this chapter, the necessary physical fundamentals are summarized for the understanding and discussion of the experimental results, such as charge transport and doping of organic semiconductors. The film formation models for vacuum and solution based depositions are also described. Furthermore, the operation of organic photovoltaic cells and other basic principles are illustrated.

2.1 Conjugated organic semiconductors

Conjugated organic semiconductors (COS) have been investigated for several decades. In the 1960s interest reached a new level following the discovery of electroluminescence. Later, the application of organic semiconductors in the field of organic electronics drew large attention, in particular, both in academia and industry where many are trying to implement and optimize organic light emitting diodes and organic photovoltaic cells.

COS, of which there are two types - low molecular weight materials and polymers, refer to organic materials exhibiting semiconductor properties owing to their electron configuration of atomic carbon in the ground state ($1s^2 2s^2 2p^2$). The first and second s-orbitals are fully occupied by two different spin electrons and the remaining two electrons take up either two of three degenerated p-orbitals. One s- and two p-orbitals can form three hybrid orbitals in the same plane, named sp^2-hybridisations. In molecules the overlapped sp^2-hybrid orbitals from adjacent carbon atoms form σ-bonds, while the third p-orbital kept perpendicular to the sp^2 plane can lead to the formation of π-bonds. Take as an example the most simple aromatic molecule benzene where all carbon atoms are sp2 hybridized (see Fig.2.1). This means that two out the three p-orbitals are hybridized with the s orbital forming three equivalent ones with the third p-orbital perpendicular to the plane of the hybridized three. The three in plane hybridized orbitals form σ -bonds with adjacent neighbors and the p_z orbitals form π-bonds respectively, retaking a delocalized electron cloud. In addition, all six π-bonds are equivalent. In comparison to σ-bonds, π-bonds are much weaker due to significantly less overlap of the neighboring p-orbitals as a result of their parallel orientation. This leads to a delocalized electron clouds mainly localized above and below the molecular plane. In this case, negatively charged π-clouds on either side of the symmetry plane are compensated by the positive charges of the atomic nuclei in the molecular plane. As a result, there are two opposite dipole pointing toward the centered molecular plane canceling the dipole moment,

resulting in quadrupolar and higher order moments, and π-type molecular orbitals (bonding π- antibonding π^*) are formed with spatially extended atoms. In the ground state, all orbitals are fully filled with electrons up to the highest occupied molecular orbital (HOMO), and all orbitals are empty from the lowest unoccupied molecular orbital (LUMO).

One theoretical mode to describe the molecular orbitals was developed through solving the Schrödinger equation $H\psi = E\psi$, called linear combination of atomic orbitals (LCAO).[Atkins, 2006] Consider the simplest case of one electron that can be found belonging to two atomic orbitals ψ_{A1s} and ψ_{B1s} respectively, with the total electron wavefunction given by the equation

$$\psi = \mathrm{N}(\psi_{A1s} \pm \psi_{B1s}) \tag{2.1}$$

where N is normalized factor. When a large molecule or even polymer are then considered, the general form of the sum wavefunction extending to all orbitals in the molecule would be

$$\psi = \sum_i c_i \psi_i \tag{2.2}$$

where $|c_i|^2$ denotes the proportion of atomic orbital i in the bonds, representing bond polarity information in the molecule. However, computation of electron wavefunctions for large weight molecules in reality with this mode is impossible due to the complex electron-electron interactions in a many body system. In addition, this mode is restricted to the linear molecules. Therefore the approach is unable to solve nonlinear cases like conjugated molecules since further approximation is required. Erich Hückel suggested, for conjugated molecules, that carbon atoms be treated equally, neglecting the influence of the alternative single and double bonds along the carbon atoms chain. In this way, all σ–bonds are considered fixed, the Coulomb integral α related to π-bonds can then be taken as equal. Consider once again benzene as an example. By employing Hückel approximation, the energies of benzene six π-bonds could be obtained from diagonalizing the Hamiltonian matrix[Atkins, 2006, Huckel, 1931]

$$H = \begin{pmatrix} \alpha & \beta & & & & \beta \\ \beta & \alpha & \beta & & & \\ & \beta & \alpha & \beta & & \\ & & \beta & \alpha & \beta & \\ & & & \beta & \alpha & \beta \\ \beta & & & & \beta & \alpha \end{pmatrix} \tag{2.3}$$

where the eigenvalues are $\mathrm{E} = \alpha \pm 2\beta, \alpha \pm \beta, \alpha \pm \beta$ respectively, α denotes Coulomb integral and β denotes resonance integral. As indicated in Fig.2.2, all bonding energies are filled such that the energy level $\alpha + \beta$ is the highest occupied molecular orbital, and symmetrically while $\alpha - \beta$ denotes the lowest unoccupied molecular orbital.

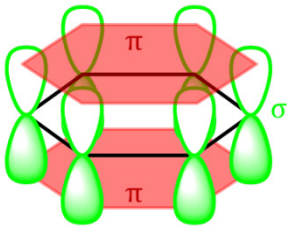

Fig.2.1 Schematic of sp^2 hybridization in benzene molecule and formation of π -bonds and σ-bonds.[Atkins, 2006]

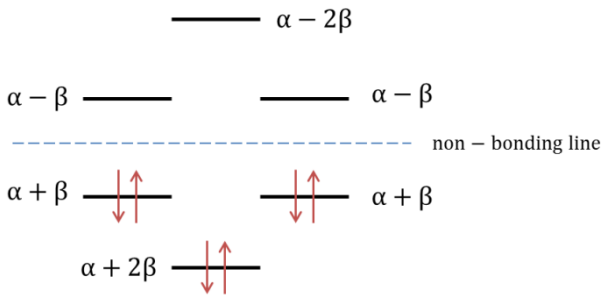

Fig.2.2 Electronic structure of the benzene molecules π-electrons [Atkins, 2006].

Molecular solids are mainly bound by Van der Waals forces as a result of dipole-dipole interactions by charge fluctuation causing non-permanent dipole moments. The dipole-dipole interaction energy can be given by the equation [Atkins, 2006]

$$V = \frac{\mu_1 \mu_2 f(\theta)}{4\pi\varepsilon_0 r^3} \tag{2.4}$$

where μ_1, μ_2 are dipoles of two molecules respectively, r is the distance between two dipoles average, ε_0 is the vacuum permittivity and $f(\theta)$ is the dipole orientations dependent function. Comparing with covalent bonding, the weak bonding forces of Van der Waals type forces give rise to low melting points and lower hardness, and in particular a big difference for both charge transport and optical properties.

The optical absorption characteristics of COS are dominated by their optical gap which is related to the extension of the π- π^* transitions. Upon optical excitation electron-hole pairs are created which usually localize on one molecule or a few monomer units of a polymer chain (Frankel exciton) due to the strong coulomb attraction. Frankel exciton is often found in organic semiconductor where molecules are not packed densely. If the exciton's electron hole spacing is larger, extending over many molecular units, such a large distance electron-hole pair is called a Wannier exciton[Wannier, 1937] (see Fig. 2.3).

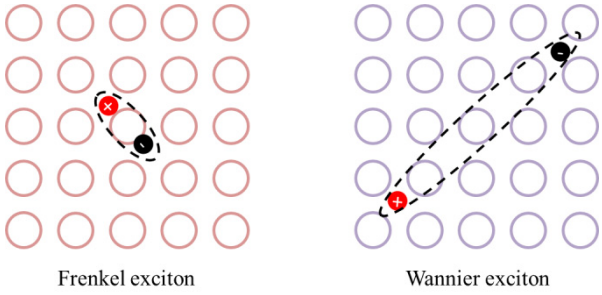

Fig.2.3 Excitons with different radii, diagrams of Frenkel exciton (left) and Wannier exciton (right).[Schwoerer, 2005]

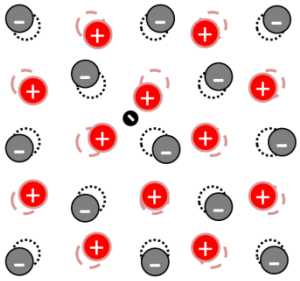

Fig.2.4 Schematic representation of a polaron. The black minus is conduction electron; dash circles are original lattice sites; grey minus are repulsed electrons; red plus is an attracted hole.

Another important effect that needs to be addressed is the polaronic effect that is typically observed in ionic and highly polar semiconductors like π-conjugated polymers. This effect was first introduced by Landau in 1933[Landau, 1933] to describe electron movement on a polarized lattice. The formation of polaron can be explained in the following manner. The Coulomb interaction between a conduction electron (hole) and surrounding lattice can deform the lattice environment, attracting holes (electrons) to the surrounding lattice sites close to the conduction electron (hole) and pushing the residual sites electrons (holes) away as shown in Fig.2.4. In π-conjugated polymers, the intersubbands are created due to the rearrangement of charges distribution, which can be found from ultraviolet/visible absorption spectroscopy (detailed discussion in section 4.3).

2.1.1 Charge carrier transport

Through years of development, conjugated organic materials have been based preferentially upon either holes (positive polarons) transport or electron (negative polarons) transport (In fact, organic materials could transport both holes and electrons[Sirringhaus,

2003]), and in most cases, the distinction relies on the relative ease of charge injection from electrodes used in devices rather than the actual charge transport capability of the materials. For instance, for organic photovoltaic cells, diindenoperylene (DIP) is usually referred to as a donor (for hole transport), e.g. when combined with fullerene acting as the acceptor (electrons transport); However, in combination with α-sexithiophene (6T), DIP can also act an acceptor.[Hörmann, 2011a]

Normally electronic transport properties can be described with the carrier mobility (μ) given by the Einstein-Smoluchowski equation in the absence of external potential,

$$\mu = \frac{eD}{k_B T} \tag{2.5}$$

where D is charge diffusion coefficient of the materials, k_B is Boltzmann constant and T is temperature. Additionally, μ can be defined by the electric field-induced velocity v and the applied electric field E,

$$\mu = v/E. \tag{2.6}$$

Similar to observations for inorganic semiconductors,[Glaeser, 1966b] upon temperature increase, the charge carrier mobility OSCs is reduced due to increased phonon scattering.[Warta, 1985] Subsequently, the local polarization interactions increase resulting in the width of the bands narrowing [Holstein, 1959a, Holstein, 1959b, Hannewald, 2004, Koch, 2006]. It turns out to be polarization networks in which polarons jump from one unit to their adjacent units. This process of charge transport is named polaron-hopping transport which recently has been shown to happen in a number of materials, such as amorphous materials and polymer thin films. Considering also the coherent electron transport (tunneling effect), the final mobility can be given as a sum of these two contributions,

$$\mu = \mu_{tun} + \mu_{hop} \tag{2.7}$$

The first term denotes the contribution of coherent electron transport dominating at low temperature, and the second term represents the domination of hopping transport in high temperature region. [Glaeser, 1966a, Emin, 1975] For instance, in the case of strong electron--photon couplings (see Fig.2.5), there are three regions: (i) at low temperature ($T \ll T_1$), the mobility is dominated by tunneling, decreased upon temperature increasing, (ii) in the intermediate region ($T_1 < T < T_2$), hopping transport starts to dominate, and the integral mobility starts to increase gradually with temperature raise and (iii) in the third region of very high temperature ($T \geq T_2$), the mobility starts to decrease due to the interruption of high thermal energy. The thermal energy is high enough to dissociate polarons leading to the occurrence of the scattering between residual electrons and thermal photons. Consequently, the conductivity is decreased.[Coropceanu, 2007b]

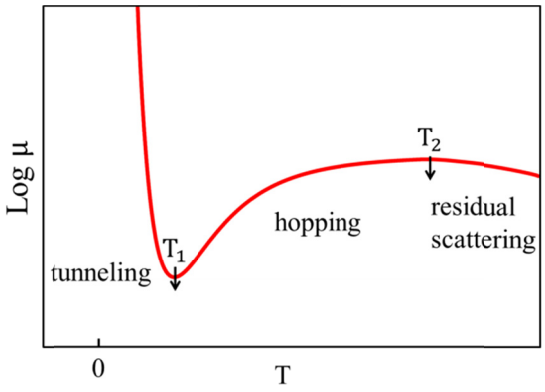

Fig. 2.5 Prediction of the temperature dependent of mobility based on the Holstein polaron mode for the case of strong electron-photon couplings. i) $T \ll T_1$, tunneling transport acts as domination; ii) $T_1 < T < T_2$, hopping transport dominates is in domain; iii) $T \geq T_2$, the thermal energy needs to be considered due to its high energy which might dissociate polarons. This figure is reproduced based on the paper.[Coropceanu, 2007b]

High charge carrier mobility poses stringent requirements on the chemical structure, packing and orientation of the molecules or polymer chains, as well as impurities and static energetic disorder.[de Boer, 2004, Chang, 2004, Adam, 1994, Sheraw, 2003, Mas-Torrent, 2004, Jurchescu, 2004, Zen, 2004, Dieckmann, 1993, Dunlap, 1996, Bässler, 1993] It is impossible to have one model covering the whole range of charge carrier mobility mechanisms due to the complicated interplay of these parameters. Thus, appropriate theoretical models of charge transport in organics are required.

One systematic model used to describe the charge transport theory was first reported by Holstein in 1959, called Bloch-wave band mode.[Holstein, 1959a, Holstein, 1959b] Although this model was only able of describing the mobility in the system of the narrow electronic bands and also limited to a specific temperature range, it was still broadly used for understanding the initial simple cases.[Moses, 2006, Li, 2007, Kakuta, 2007, Ostroverkhova, 2006, Fischer, 2006, Fratini, 2009] In the simple one dimensional case, the mobility of hopping can be described as,

$$\mu_{hop} = \frac{ea^2t^2}{k_B T\hbar^2\omega}\left[\frac{\pi}{\alpha csch\left(\frac{\hbar\omega}{2k_BT}\right)}\right]^{\frac{1}{2}} exp\left[-2\alpha tanh\left(\frac{\hbar\omega}{4k_BT}\right)\right] \tag{2.8}$$

and the tunneling mobility (coherent charge transport) is given by

$$\mu_{tun} = \frac{ea^2}{k_BT}\omega\left[\frac{\alpha}{\pi}\text{csch}\left(\frac{\hbar\omega}{2k_BT}\right)\right]^{\frac{1}{2}}\exp\left[-2\alpha\text{csch}\left(\frac{\hbar\omega}{2k_BT}\right)\right] \tag{2.9}$$

where a is the spacing between molecules, t is the absolute value of the transfer integral for electrons or holes, $\hbar\omega$ is the energy of an optical phonon and $\alpha = E_p/\hbar\omega$ is the ratio of the polaron binding energy to an photon energy $\hbar\omega$ representing the electron-photon coupling strength.[Warta, 1985, Coropceanu, 2007b, Brutting, 2012] Equation 2.9, which is based on the assumption of narrowing band, is normally used to analyze the coherent charge transfer at low temperature.

When intermolecular distances and orientations in organic thin films vary as in molecular doped polymers, static disorder dominates the charge transport properties. Upon increasing the amount of disorder, more and more band states present in highly ordered materials become localized, turning charge transport in the hopping regime with charges migrating between interacting molecules. One applicable model describing hopping in a manifold of sites is the Gaussian disorder model. The hopping rate was simplified by Miller and Abrahams[Miller, 1960, Bassler, 2012] and given by the expression

$$\kappa_{ij} = \nu \cdot \exp(-2\gamma R_{ij}) \begin{cases} \exp\left(-\frac{\epsilon_j - \varepsilon_i}{k_B T}\right) & \epsilon_j > \varepsilon_i \\ 1 & \epsilon_j < \varepsilon_i \end{cases} \tag{2.10}$$

where ν is the attempt hopping frequency, R_{ij} is the separation between sites i and j, γ is the overlap factor and, ε_i and ϵ_j are the site energies. The first exponential term represents the overlap of the wave function between state i and j associated with the tunneling effect. The second exponential term is the Boltzmann factor for a jump to higher energy level and equal to 1 for a jump to lower energy site. This mode enables the description of the case of weak electron-photon coupling and low temperatures, indicating that upwards hops are temperature activated and downwards hops are temperature independent.

Another simplified mode to describe the semi-classical electron-transfer rates in highly disorder organic semiconductor system was given by Marcus,[Marcus, 1993]

$$\kappa_{ij} = \frac{t^2}{\hbar}\left[\frac{\pi}{k_B T \lambda}\right]^{\frac{1}{2}} \exp\left[-\frac{(\lambda + \epsilon_j - \varepsilon_i)^2}{4\lambda k_B T}\right] \tag{2.11}$$

where λ is intramolecular reorganization energy. This mode is suitable for large electron--photon couplings and high temperature due to the introduction of λ.

In reality, hopping is well accepted to describe the motion of charge carriers, owing to the static, energetic and positional disorder in low-mobility organic semiconductors.[Brutting, 2012] However, new developed organic materials with high mobility of 1 cm^2/VS cannot be simply explained with one model[Anthony, 2010]. Thus, understanding charge carrier transport requires a combination of the Bloch-wave band model and the hopping model, which has previously been discussed in detail [Brutting, 2012]. Experimentally, the charge carrier mobilities of organic materials, which can be prepared as thin films, may be

investigated using several methods such as time-of-flight measurement, space charge limited current method in diode measurement and field-effect transistor measurement.

2.1.2 Doping organic semiconductors

Doping was used as one of the most efficient strategies for realizing device functionality in organic semiconductors (OSCs) for several decades as inspired by the doping of inorganic semiconductors. [Akamatu, 1954, Lüssem, 2013] Ideally, doping OSCs was expected to achieve the same functions of inorganic counterparts, such as increasing conductivity and tuning the position of Fermi-level for a single layer. In fact, doping led to an increase in conductivity for OSCs as verified by many methods such as filling of shallow traps or by introducing additional traps, [Gao, 2003, Arkhipov, 2005a, Arkhipov, 2005b, Krellner, 2007, Yim, 2008, Sun, 2009, Zhang, 2010, Rivnay, 2011, Mityashin, 2012, Nicolai, 2012, Olthof, 2012, Pingel, 2012]. This conductivity increase is demonstrated in Fig.2.6 where there increase is almost linear with the doping ration increase in the low doping region. The function of tuning energy level is still under investigation.

In general, the doping process in OSCs is similar to that for inorganic counterparts, in that dopants are mixed with the host material becoming ionized. Afterwards holes (electrons) are donated to the host material leading to the creation of electrons (holes). However, the indeed doping behavior is different caused by the complex charge transport characteristics, as discussed in section 2.1.1.

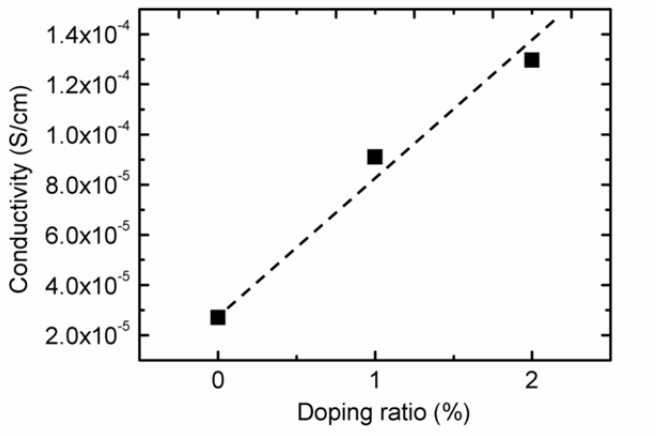

Fig.2.6 Conductivity of polyfuran film with increased doping ratio. The dopant is tetrafluorotetracyanoquinodimethane (F4-TCNQ). The doping ratio 1% refers to the additional of 1 F4-TCNQ molecule per 100 periodic polyfuran monomer units.

In early research, the doping of OSCs was inspired by the doping of inorganic semiconductors, utilizing iodine or bromine as dopants. However, when applied to organic electronic devices, the devices exhibited short life-time induced by instabilities of the doping atom in OSCs caused for example by diffusion. [Akamatu, 1954, Yamamoto, 1979] Later, small metal atoms, for instance lithium, were used as dopants with such doping OSCs systems also suffering instability issues like diffusion.[Kido, 1998, Walzer, 2007, Parthasarathy, 2001] In order to solve the problem mentioned above, large atoms or even molecules provide a suitable alternative. Therefore, molecular doping OSCs were developed in an attempt to realize controllable and stable doping.[Kearns, 1960, Nollau, 2000b, Zhang, 2009, Salzmann, 2012a, Aziz, 2007] Karl Leo and his co-workers did systematical research both on p-type and n-type doping to understand the molecular doping behavior and presented stable doping of OSCs with small molecules and successfully applied this to fabricate organic electronic devices. [Reineke, 2009, Lüssem, 2013, Pfeiffer, 1998, Maennig, 2001, Nollau, 2000a]

One model (see Fig.2.7) used to describe the organic doping is integer charge transfer. For p-type doping, an electron transfers from the HOMO of the host to the LUMO of the dopant, creating a localized charge on the dopant and a coulombically bound hole or mobile hole in the OSCs matrix. In this case, the electron affinity (EA) of the p-type dopant must be higher than the ionization energy (IE) of the host. Similarly, for n-type doping, the dopant donates an electron from its' HOMO to the LUMO of the host, thereby creating a hole. (In reality, n-type doping was not commonly used as p-type doping because few molecules could satisfy the energy level requirement that the LUMO of the dopant molecule needs to be higher than the HOMO of the host molecule).

Figure 2.8 illustrates another recently reported model for molecular doping in OSCs.[Aziz, 2007, Salzmann, 2012a, Pingel, 2010, Mendez, 2013, Heimel, 2012] This model suggested that frontier molecular orbital hybridization could happen between the HOMO of OSCs and the LUMO of dopants for a p-type doping, which led a middle state with a reduced energy gap composed of hybrid orbitals. The middle state was named as charge-transfer complex. In such a state, free charge can be produced by intermolecular excitation. For instance, doping 2,7-didecy(1)benzothieno(3,2-b)(1)benzothiophene (BTBT) with tetracyanochinodimethan (TCNQ) and its fluorinated derivatives, orbital hybridization between the BTBT HOMO and the LUMO of the TCNQ derivatives results in the formation of a charge-transfer complex with a reduced energy gap. That extra absorption peak in the infrared region corresponds to low energy transitions that can be deduced based on the model with Hückel-like treatment.[Salzmann, 2012a, Huckel, 1931] The band gap energy can be obtained from the secular equation

$$E = \frac{1}{2}\left[(E_{\mathrm{H-O}} + E_{\mathrm{L-D}}) \pm \sqrt{(E_{\mathrm{H-O}} - E_{\mathrm{L-D}})^2 + 4\beta^2}\right] \tag{2.12}$$

where $E_{\mathrm{H\text{-}O}}$ is energy level of OSCs HOMO, $E_{\mathrm{L\text{-}D}}$ is energy level of dopant LUMO and β is the intermolecular resonance integral. According to equation 2.12, the complex band gap energy strongly depends on the $E_{\mathrm{L\text{-}D}}$.

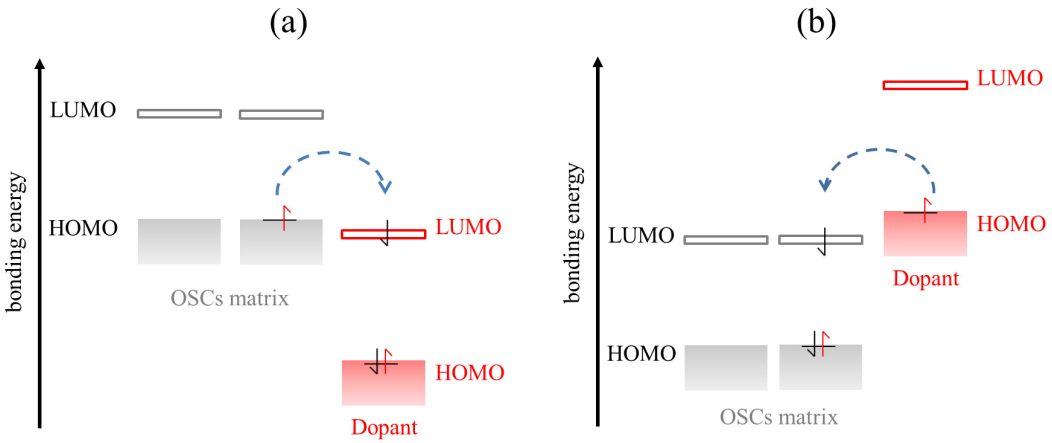

Fig.2.7 Schematic representation of molecular doping mode: integer charge transfer mode. (a) p-type doping; (b) n-type doping. LUMO denotes the lowest unoccupied molecular orbitals, HOMO denotes the highest occupied molecular orbitals. OSCs are organic semiconductors, red balls with plus inside denote positive charges, blue balls with minus denote negative charges. Dash-line balls with minus denote the original position of negative charges before doping.

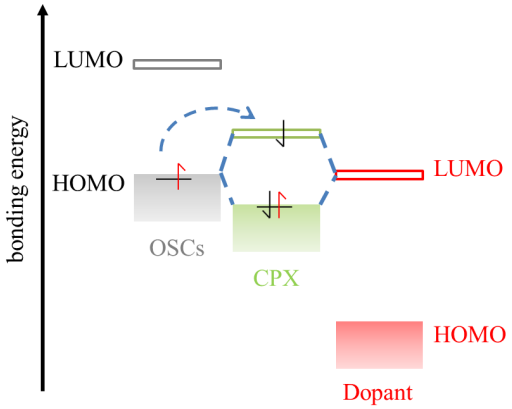

Fig.2.8 Schematic representation of alternative molecular doping mode: charge transfer complex mode. LUMO denotes the lowest unoccupied molecular orbitals, HOMO denotes the highest occupied molecular orbitals. OSCs are organic semiconductors, CPX denotes the energy levels of charge transfer complex, red ball with plus inside denote positive charges, blue ball with minus denote negative charges. Dash-line balls with minus and plus denote the final positions of negative and positive charges after doping. The figure is reproduced from the paper [Mendez, 2013].

Doping efficiency is mainly determined by the ionization rate of the dopant in OSCs. Commonly, it is given by the ratio of free charge carriers to the number of dopants. As a result

of the low dielectric constant in OSCs, strong Coulomb interaction between ionized dopants and the charge transferred to the host can hinder them from turning to free charges, which means not every ionized dopant can generate a free charge. Thus, doping efficiency in OSCs is much lower than that in inorganic semiconductors. In addition, as demonstrated in the second model, the ionization rate of the dopant is strongly affected by the magnitude of hybridization which can be determined by the individual energy levels of OSCs and dopants, as well as the molecular structures at the nodal.[Coropceanu, 2007a, Salzmann, 2012a, Mendez, 2013, Lüssem, 2013, Walzer, 2007] For instance, the IE of zinc phthalocyanine was 5.28 and EA of tetrafluorotetracyanoquinodimethane (F4-TCNQ) was 5.24. Assuming the charge transfer rate of ZnPc/p-type dopant F4-TCNQ was 1; when using TCNQ whose EA was 4.5 eV instead of F4-TCNQ as dopant, the charge transfer rate decreased to 0.2.[Gao, 2002, Brutting, 2012]

2.2 Organic thin film fabrication

The fundamental properties of organic thin film are strongly dependent upon the film structure. [Koma, 1995, Kowarik, 2008b, Kowarik, 2008a, Dürr, 2002, Hinderhofer, 2012b, Kim, 2012, Gruber, 2013, Oh, 2011, Noriega, 2013] Recently, a rapid increase in research activity on organic thin films was triggered by their successful application in electronics and optoelectronics, as well as their further application potential.[You, 2013b, Søndergaard, 2013, Reineke, 2009] In order to optimize the film structure to satisfy the stringent requirements when trying to enhance the performance of an organic electronic device, a thorough understanding of the physics of growth processes is essential to accurately control over the dynamics of films formation. In terms of the growth method, thin film preparation can typically be completed in two ways: vacuum deposition and solution processing. In this section, first the dynamic processing of film formation on the substrate and the models of film growth are presented. Furthermore, the importance of molecular orientation with respect to the substrate normal is emphasized. Second, the fundamental principle and procedure of film formation from solution processing are both introduced.

2.2.1 Vacuum deposition

Organic molecular beam deposition (OMBD) has been used as a well-established vacuum deposition method to prepare organic thin film since 1985.[Koma, 1985, Masahiko, 1989] Compared to other techniques, the OMBD has the advantages of accurate thickness control, and clean environment and substrate, which both are important for investigating the film formation mechanism and fundamental properties.

The micro view of film formation process by OMBD is now outlined. Assuming a sublimed molecule impinges on a given substrate surface with a certain velocity, either an elastic or inelastic collision can occur. In the case of an elastic collision no energy is transferred, but during inelastic collision the molecule may gain or lose energy. Of course when the molecule is losing energy its probability of being absorbed at the surface is higher. The absorbed molecules lack the energy to escape the sorbent surface where they only can diffuse, exhibiting a random walk-like path until they dissipate all their energy or are bonded through nucleation and stabilized on the surface. Upon deposition multiple dynamic processes can occur such as inter-layer diffusion, intra-layer diffusion and dissociation of previously formed molecular nucleation as shown in Fig.2.9. Hence, the final film morphology is impacted by several dynamic processes, depending on the interaction between the substrate and absorbed molecules. [Venables, 1984, Forrest, 1997]

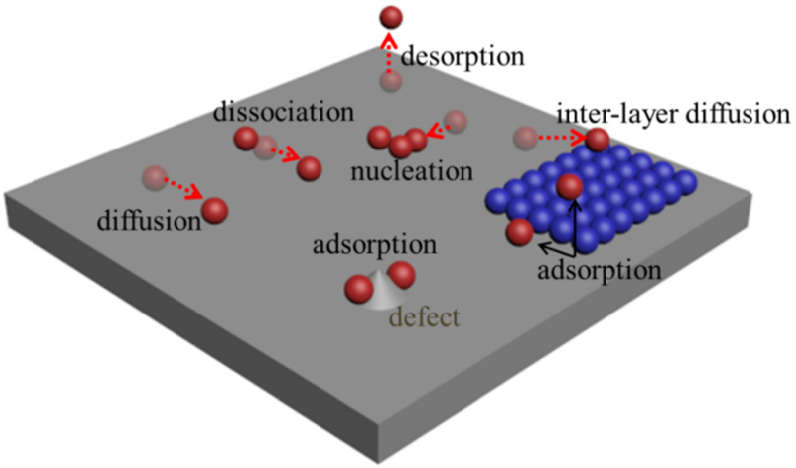

Fig.2.9 Simplified schematic representation of dynamic process of molecular deposition on a given substrate in vacuum. The blue balls are molecules initially on the substrate; red balls are new in-coming molecules; half transparent red balls are the original molecule positions before motion. Diffusion, dissociation, desorption, growing on nucleation/defects and inter-layer diffusion are depicted respectively. Reproduced from [Schreiber, 2004]

The forces keeping molecules stable on the substrate surface are relevant for the bonding energy, physisorption (physical absorption) or chemisorption (chemical absorption). The term physisorption, the realm of low bonding energy, is mainly mediated by van der Waals force that originates from the induced molecular dipole. This means that there is nearly no disturbance on the molecular and electronic structure for absorbed molecules. For convenience, Lennard-Jones Potential is used to describe the physical absorbed interaction:

$$\varepsilon(r) = -4\varepsilon_0 \left[\left(\frac{\sigma}{r}\right)^6 - \left(\frac{\sigma}{r}\right)^{12} \right] \tag{2.13}$$

ε_0 is potential energy at the minimum, r is the distance between substrate surface and the absorbed molecules and σ is effective molecular diameter.[Ibach, 2006] The first term represents attractive potential induced by van der Waals force, and the second term is the Pauli repulsive potential that dominates at small distances. In contrast, the chemisorption usually refers to high bonding energy between absorbed molecules and given substrate surface, induced by electron density rearrangement, which can consist of covalent or ionic bonds.

There are three primary growth modes (see Fig 2.10) on substrates that differentiate how small clusters develop into films.[Barabási, 1995, Pimpinelli, 1998, Schreiber, 2004] If the bounds between individual molecules are stronger than the bounds between molecules and the substrate, then additional molecules prefer to attach to the existing clusters at the substrate, growing to form three-dimensional islands. This mode is referred to as island growth mode (Volmer-Weber growth mode). The other extreme case is that the molecular binding energies

are equal to, or less than, the molecule-substrate interaction strength. As a result, the molecules tend to fill all voids and complete a monolayer on the substrate before starting to grow another monolayer. Intuitively one calls this layer-by-layer growth mode (Frank-van de Merwe growth mode). The intermediate case is a combination of the last two. After initially forming a (few) monolayer(s), further layer growth becomes unfavorable due to the weaker molecule-substrate interaction the farther away the new layer is. Consequently, islands start to form after a certain amount of full monolayers were grown.

Molecular anisotropic features (e.g. rod-like molecules like pentacene and diindenoperylene) need to be considered in the processing of single molecule growth to form films on the substrate. This is relevant since experimental observations reveal that the molecular orientation relative to the substrate can strongly affect the many physical properties of organic films. [Gruber, 2013, Kowarik, 2009, Tripathi, 2006, Heinrich, 2007, Salzmann, 2012b] For instance, there is a large difference between the absorption coefficient of diindenoperylene lying phase and the standing phase because its' transition dipole moment is polarized along the molecular long axis (detail discussion in Section 4.2). [Heinemeyer, 2008b] Fig.2.11 shows the angle dependent absorption measurement of 100 nm diindenoperylene thin film on indium tin oxide substrate. As can be seen, the absorbance peaks in the range of 400-600 nm are significantly increased upon increasing the angle between the incident light beam and the surface normal, meaning that on the substrate, most of diindenoperylene molecules adopt "standing" orientation.

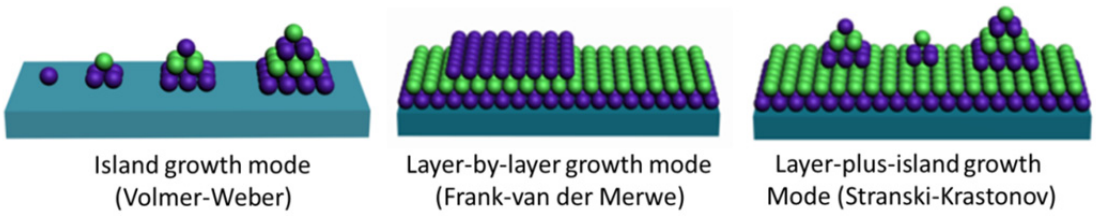

Fig.2.10 Different molecular growth models by physical deposition in vacuum. Sketch of island growth, layer-by-layer grow and layer-plus-island growth models. Green and purple balls represent molecules.

For simplification, the molecular orientation with respect to the substrate surface normal was described in two cases. First if the van der Waals interaction, often existing among molecular semiconductors, exceeds the interaction between molecules and the substrate, then the following scenario may take place. One single molecule reaching at the substrate surface exhibits lying orientation. When several molecules meet this molecule in the process of diffusion on the substrate surface, they can form a stable agglomeration and tilt out of the substrate plane,[Meyer zu Heringdorf, 2001b] as shown in Fig.2.12a and b. In another case, when the interaction between molecules and the substrate is substantial enough in the first monolayer, such as for conjugated molecules on clean metal surfaces, the molecular

orientation is confined by this interaction. However, once film thickness increases to a realm, the interaction between molecules deposited later and the substrate gets weaker, and as such the van der Waals interaction dominates once again resulting in "standing" molecules on top of lying molecules (see Fig.2.12c). [Glowatzki, 2007, Ziroff, 2010, Koch, 2007b, Bröker, 2010]

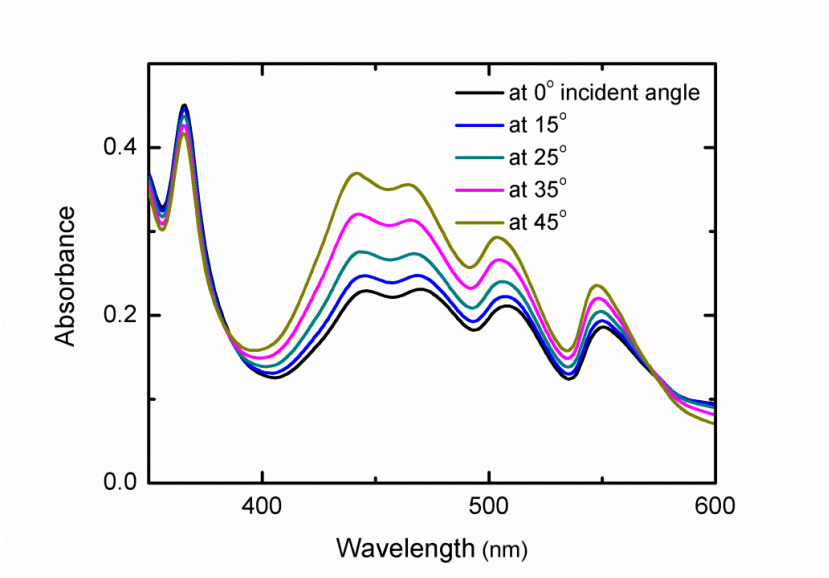

Fig.2.11 Ultraviolet/Visible spectra of 100 nm thick diindenoperylene thin film vacuum deposited on indium tin oxide substrate. The sample was placed perpendicular to the incident light beam when using 0 degree.

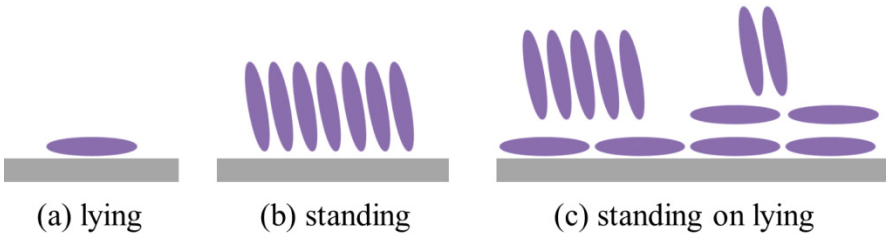

Fig.2.12 Schematic presentations of molecular orientation on the substrates. (a) A single molecule lies on the substrate. (b) A group of molecules exhibit a "standing" orientation due to the van der Waals interaction among molecules being stronger than the interaction between molecules and the substrate. (c) The interaction between molecules and the substrate is stronger than the van der Waals interaction in the first monolayers and molecules adopt a lying orientation. The top molecules have weaker interactions with the substrate and thus exhibit a "standing" orientation. Reproduce from [Wilke, 2013]

2.2.2 Solution processing

Growth characteristics of polymer films are also very important as for the case of molecular films, determining optical and electrical properties as discussed previously. However, unlike for small molecules, thermal evaporation is not applicable to highly conjugated polymers because of instability (decomposition and degradation) at high temperature. Therefore, organic thin films consisting of conjugated polymers are typically formed from solution processing such as spray or spin coating and droplet casting. Generally, the complicated processes of polymer film formation from homogeneous dissolved polymeric solutions can be described as follows. The solution is deposited onto the substrate and then spread out across the substrate (depending on the preparation method used). When the solvent dries out, it first turns to a gel state with entangled polymer chains leading to an increase in the viscosity. A solid film results with further drying. [Felton, 2013]

The spreading process of the solution on the substrate surface is related to the wetting properties of the solution such as the surface tension and the characteristics of the substrate surface i.e. roughness and hydrophobicity. Two typical wetting models are shown in Fig.2.13 (a) and (b). The entangled polymer structure in the gel state is induced by polymer chains interpenetrating each other as a result of the hydrodynamic interaction between the polymer and the solvent during a local increase in viscosity. [Bauer, 1998] Furthermore, the evaporation rate of the solvent is also crucial in the film formation process. For instance, if the evaporation rate is too high, the droplets may dry before spreading over the whole substrate surface leading to a small crystalline size. On the other hand, the solid polymer film might be re-dissolved and resulting in a large crystalline size due to the relative high local concentration. This will occur if the evaporation rate is too low.

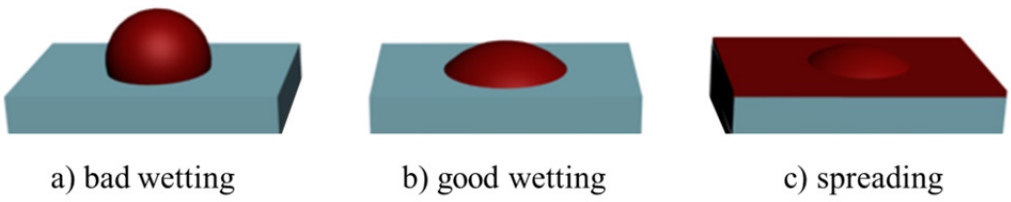

Fig.2.13 Diagram of two types wetting models in film coating process. a) Bad wetting. b) Good wetting. (c) Spreading. The dark green square denotes the substrate; red wine quasi-sphere/film denotes the solution.

The formation of a polymer film is dependent upon the interplay of the macromolecules with the substrate, preparation methods, as well as processing conditions such as air pressure and humidity. For instance, PEDOT:PSS polymer film is coated on top of ITO substrate as a

hole transport layer to smooth the substrate surface. The work function of PEDOT:PSS can be increased with an annealing process that aims to remove the residual water in the polymer film.[Koch, 2007d]

2.3 Organic photovoltaic cells

This section will introduce the theoretical fundamentals and operation mechanisms of OPVCs. First from microscopic point of view, the basic principles of energy level alignment in the device are introduced and the modes for understanding exciton generation, transfer and dissociation processing are illustrated. Next the idealized equivalent circuit mode and other important parameters for analyzing the OPVCs performance are described.

2.3.1 Operation mechanism of OPVCs

Separated charge carriers are transported towards the respective electrodes. The general structure of OPVCs consists of one or more thin organic layers between two metal or conductive electrodes with different work functions. In the work presented in this thesis, two organic thin layers (bilayer) acting as active absorbers are employed as donor and acceptor materials respectively. The operation of OPVCs can be described as follows as shown in Fig.2.14,

i). Excitons are generated in absorbers by illumination.

ii). Excitons diffuse to the donor/acceptor interface

iii). Excitons at the donor/acceptor interface are separate to free electrons and holes.

iv). Separated charge carriers are transported towards the respective electrodes.

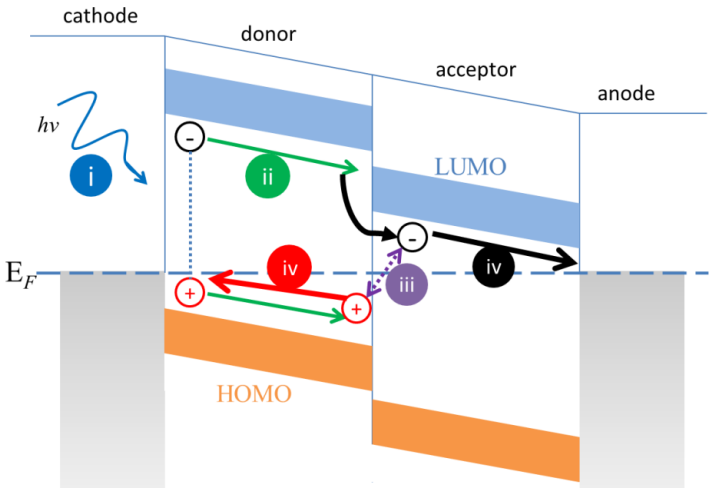

Fig.2.14 Diagram of three-step operation principle of a bilayer heterojunction OPVs. Orange/blue boxes denote HOMO and LUMO of organic materials respectively and hν denotes energy of photon. E_F is the substrate Fermi level.

Using the discussion presented above, the basic principles for the design of high efficiency OPVCs can be easily summarized. First strong absorbing materials combined with high quantum efficiency are preferred, ideally covering the entire range of the solar spectrum. Second, before separating excitons to charge carriers at the interface of the donor/acceptor layers, it is necessary that excitons have a sufficient diffusion length in order to be transported to the interface. The exciton diffusion in organic film is very complicated, and normally the excitons diffusion length is used to quantitatively describe the excitons diffusion processing. However, there are many factors which could impact the excitons diffusion length, such as the material's chemical structure and crystallization and molecular orientation.[Menke, 2014] The exciton dissociation process is in principle governed by the energy-level offset at or in vicinity of the donor/acceptor interface.[Sariciftci, 1992, Sariciftci, 1993, Stübinger, 2001, Koch, 2007a] After exciton dissociation, charge carrier transport with inhibited recombination requires high charge carrier mobility as is discussed in section 2.1.1.

a. Energy level alignment

As mentioned previously, the electronic structure of the interfaces within the OPVCs plays an important role in device performance. For instance, the energy offset between the HOMO of the donor and the LUMO of the acceptor governs exciton dissociation to free charges and hence has a direct impact on the possible V_{oc} of OPVCs [Wilke, 2012]. Also the energy level alignment between electrodes and the organic films could lead to barriers that hinder the collection of dissociated charges from the OPVCs.

(i) Electrode/organic interface

In general, the simplest model describing the interface energetics is vacuum level (E_{vac}) alignment (Schottky-Mott limit). In this case, no internal dipolar layers arise after molecular deposition on the substrate. Then electron and hole injection barriers (EIB and HIB) at electrode/organic interfaces can be estimated from separately determining the electrode work function (ϕ), and the electron affinity (EA) as well as ionization energy (IE) of the organic materials (*c. f.* Fig.2.15a) respectively using the expressions EIB= ϕ-EA and HIB=IE- ϕ. However, the model is only applicable to certain interfaces. Routinely one observes physicochemical process at the interface, leading to vacuum level shifts. Calculation of the barrier heights via the above equations breaks down for this situation,[Witte, 2005, Kahn, 2003a, De Renzi, 2005, Koch, 2003]. As shown in Fig.2.15b, the values of EIB and HIB can be changed by the vacuum energy shift $\Delta\phi$ so that $\mathrm{EIB}' = \phi' - \mathrm{EA}$ and $\mathrm{HIB}' = \mathrm{IE} - \phi'$ where $\phi' = \phi - \Delta\phi$. The charge injection barrier depends on the specific contact materials. For instance, if using a higher ϕ electrode ($\phi > \mathrm{IE}$), in order to establish thermodynamic equilibrium, charge transfer from molecules to electrode will occur at the interface. However, this normally results in the alignment of the HOMO below the Fermi Level again, leading to small HIB (Fig.2.15c). However the exact energy level alignment is dependent on many aspects as contaminations of the surfaces that are not presented in detail here.

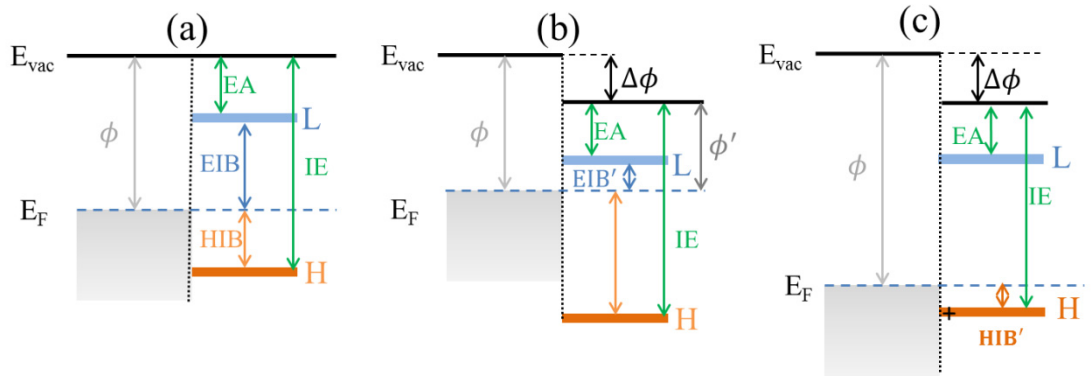

Fig.2.15 Schematic energy level diagrams for interfaces between electrodes and organic materials. (a) Vacuum level alignment. (b) Low work function contact ($\Delta\phi$). (c) High work function contact. ϕ is electrode work function, E_F is electrode Fermi level, L is LUMO of organic semiconductor, H is HOMO of organic semiconductor, EA is electron affinity of organic semiconductor, IE is ionization energy of organic semiconductor, EIB and EIB' are electron injection barriers, and HIB and HIB' are hole injection barriers.

In this work, the bottom electrode used for device fabrication is PEDOT:PSS. Different to metal electrodes, the interaction between polymer electrodes and molecules is quite weak. Several studies on energy level alignment between PEDOT:PSS and some organic semiconductors presented a comparably simple rule showing that the employment of a higher work function PEDOT:PSS electrode ($\phi >$ IE) could effectively reduce the HIB to a few hundreds meV (polaron relaxation energy). [Koch, 2007b, Rentenberger, 2006, Koch, 2005, Wagner, 2010, Wilke, 2011, Wagner, 2012] One model explaining such behavior is the integer charge transfer model, where pinning occurs between substrate Fermi level and positively charged states formed by positive polarons in the organic materials.[Fahlman, 2007, Braun, 2009, Brutting, 2012]

(ii) Organic/organic interface

For simplification, the Schottky Mott limit can be adopted to study the energy level alignment at organic/organic interfaces also if no strong chemical interaction occurs (see Fig.2.16). After depositing the second molecule semiconductor on top of initial molecule, vacuum level pinning occurs with no associated energy level shift. The energy offset between the HOMO level of first organic semiconductor and LUMO level of second organic semiconductor is defined as the photovoltaic gap (E_{pvg}), which plays a crucial role on photogenerated exciton dissociation in OPVCs, which is given by the expression:

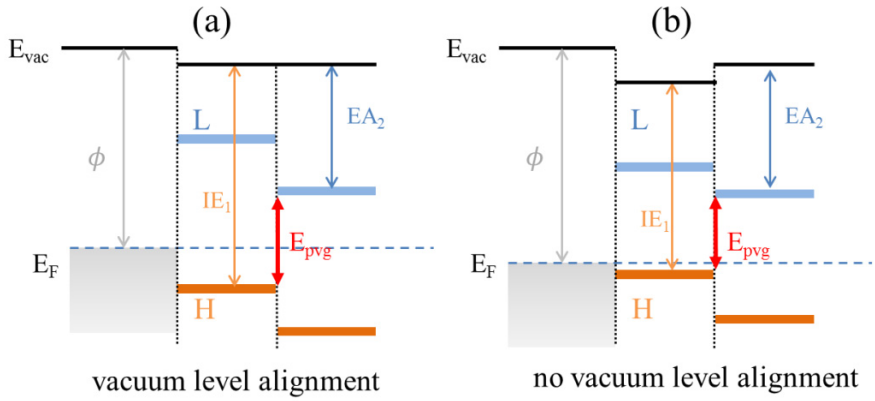

Fig.2.16 Schematic energy level diagrams for interfaces between organic and organic semiconductors on substrates. (a) Vacuum level alignment. (b) Non vacuum level alignment. IE_1 is ionization energy of first organic semiconductor, EA_2 is electron affinity of second organic semiconductor, E_{pvg} is photovoltaic gap. The small interface dipole at organic/organic interface is due to polarization effect.

$$E_{\text{pvg}} = IE_1 - EA_2 \tag{2.14}$$

Furthermore, the energy level alignment at organic/organic interface can also be affected by the morphologies and molecular orientation of the organic layers, as well as substrate energy level pinning conditions.

b. Photogeneration

The absorption probability of an incident photon of energy hv can be described by the absorption coefficient $\alpha(hv)$ which can be determined by ultraviolet/visible absorption spectroscopy. This is discussed in greater detail in next chapter. When the photon energy is larger than the absorber's optical gap, excitons can be generated. The light intensity, and hence also the photogenerated charge carriers, decreases exponentially with sample depth z, but for an infinitesimal thick organic layer the probability of absorbing photons can be taken to be equivalent. The absorption coefficient in organic film is therefore given by:

$$\alpha(\hbar v) \approx A^*\left(hv - E_g\right)^{\frac{1}{2}} \tag{2.15}$$

where A^* is a constant and E_g is the optical gap energy. The photogeneration (G) of electron-hole pairs (excitons) on an area A thereby can be obtained by integrating over the film thickness,

$$\mathrm{G(z)} = A^* \int \left(1 - r(\lambda)\right) f(\lambda)\alpha(\lambda)e^{-\alpha z} d\lambda \tag{2.16}$$

where λ is incident light wavelength, $r(\lambda)$ is the reflectance and $f(\lambda)$ is the incident photon flux.[Brabec, 2003]

c. Recombination

Generated electrons and holes can recombine during transportation and do not contribute to the output electrical current. Energy generated by electron-hole annihilation can be redirected in two manners called radiative recombination and non-radiative recombination. In a non-radiative recombination, the energy is taken up by generated phonons owing to atomic vibrations or other charge carriers who can lose their energy via scattering.[Brabec, 2003] This process is only predominant when there are abundant mediate states in the energy gap. In contrast, radiative recombination generates photons once again.

One well accepted model for describing the charge carrier recombination was introduced by Langevin in 1903.[Langevin, 1903, Foertig, 2009, van der Holst, 2009] The recombination rate is given by the equation,

$$R_L = \frac{e(\mu_e+\mu_h)}{\epsilon_r\epsilon_0}\left(n_e n_p - n_i^2\right) \tag{2.17}$$

where μ_e and μ_h are electron and hole mobility respectively, ϵ_r is the relative dielectric constant of the semiconductor, ϵ_0 is the vacuum permeability, n_e and n_p are the charge carrier concentration of photogenerated electrons and holes and n_i is the intrinsic charge carrier concentration. This model assumes that the recombination of charge carriers only occurs when the mean-free path of charge carriers is smaller than Coulomb radius r_c,

$$r_c = \frac{e^2}{4\pi\epsilon_r\epsilon_0 k_B T} \ . \tag{2.18}$$

Theoretically, in the work presented here, it is found that employing high charge carrier mobility organic materials as absorbers can be very helpful towards hindering the photogenerated charge carrier recombination in OPVCs. Additionally, in real organic electronics, the recombination also takes place at the interface of grain boundaries, the contacts between organic materials and electrodes, as well as at the defects in the organic materials.

d. Exciton diffusion

The photogenerated excitons (electron-hole pairs) can be separated to free electrons and holes at or around the interface of the donor/acceptor layers where the Coulomb interaction can be overcome by the electrical field produced by the donor/acceptor heterojunction, and thus effectively contribute to the net electrical current,. Therefore, the randomly produced excitons in the organic layer are transferred to the interface where separation can occur. There

are two types of theories used to describe the energy transfer of exciton migration in organic semiconductors, Förster and Dexter transfer.

The Förster transfer rate is given by Förster transfer refers to the non-radiative transfer taking place via dipole-dipole interaction between the electronic states of the "host" molecules and the "neighboring" molecules.[Förster, 1959, Ahn, 2007, Feron, 2012] Here, the "host" molecule is the energy donor that contains the exciton, and the "neighboring" molecule is the molecule that will accept energy. The transfer process can be described as follows. Due to light absorption in a "host" molecule, the molecule is excited to the higher vibrational level of its first electronic excitation state and subsequently converted to lower vibrational levels of the same electronic state to reach thermal equilibrium. When the energy difference for one of thermal relaxation is equivalent to one possible absorption transition of a "neighboring" molecule with a sufficiently strong dipole-dipole interaction, the same processes give rise to a transfer of excitation energy from the "host" molecule to the "neighboring" molecule. Naturally, excitation transfer between highly ordered comparable molecules can occur simultaneously and therefore, in solid films, the excitation can migrate from the absorbing molecule to another molecule over tens of nanometers away before recombination.[Förster, 1959] The Förster transfer rate is given by

$$k_{FT} = \frac{1}{\tau_0}\left(\frac{R_0}{r}\right)^6 \tag{2.19}$$

where τ_0 is the fluorescence lifetime of the exciton, r is the distance between "host" molecule and "neighboring" molecule, and R_0 is the Förster transfer radius,[Förster, 1959] which is defined as:

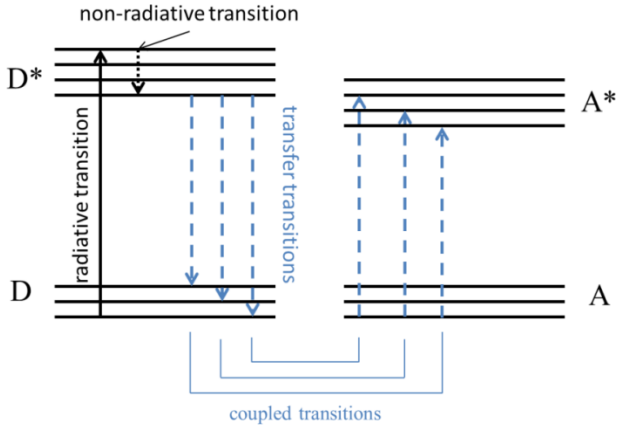

Fig.2.17 Diagram of simplified model of Förster transfer. D denotes donor molecule and A denotes acceptor molecule. [Förster, 1959]

$$R_0^6 = \frac{9000ln10\phi\kappa^2}{128\pi^5 n^4 N_A}\int_0^\infty f_s(v)\epsilon_A(v)\frac{dv}{v^4} \quad (2.20)$$

where ϕ is the fluorescence quantum yield, k is the orientation factor between the "host" and "neighboring" molecule, n is the refractive index, N_A is Avogadro's number, v is the frequency of light, $\epsilon_A(v)$ is the peak-normalised fluorescence spectrum of the donor and $f_s(v)$ is the absorption spectrum of the "neighboring".

Considering highly ordered molecular packing, the intermolecular spacing is very small, and their Coulombic interaction may no longer be determined by dipole-dipole interaction. Additionally, Förster transfer is forbidden for triplet exciton transfer; thus Förster transfer model is not applicable. Another model, the Dexter transfer model, allows for a description of the energy transfer process in terms of electron exchange directly, which requires the molecular orbitals to overlap.[Dexter, 1953] The transfer rate decays exponentially with increasing distance between two molecules, and remains constant within the typical distance (d) of one nanometer. A thickness dependent expression for the transfer rate is

$$k_D(d) = K \cdot J \cdot \exp\left(-\frac{2d}{L}\right) \quad (2.21)$$

where K relates to orbital interaction, J is nominalized spectral overlap integral and L is the van der Waals radius.[Dexter, 1953, Menke, 2014] One simplified representation is shown in Fig.2.18 describing the process of electron transfer through the physical exchange of electrons in the Dexter transfer model. Thus, exciton transfer can be described as an ensemble of self-energy transfer hopping events in one unit lattice.[Powell, 1975]

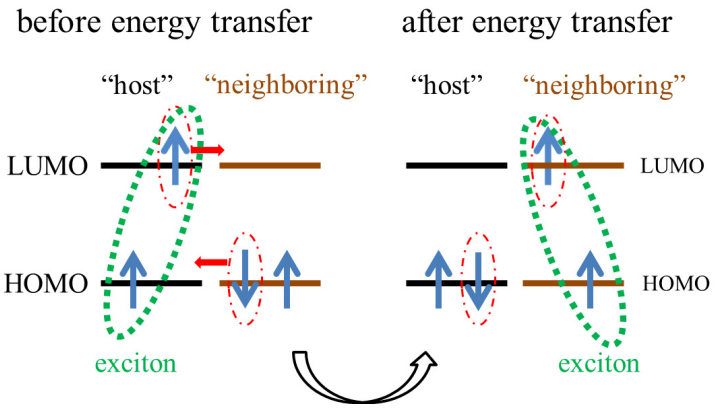

Fig.2.18 Simplified schematic representation of triplet Dexter transfer.

e. Exciton dissociation

In general, when excitons diffuse to the donor/acceptor interface without recombining, they can be separated to free charges. Alternatively, they can recombine to the ground state. In order to obtain high efficiency of OPVCs, the exciton dissociation rate must be high and stable, and recombination should be inhibited. However, the mechanism of exciton dissociation across the donor/aceeptor interface into free charge carriers is still under debate. [Sano, 1979, Braun, 1984, Barth, 1997, Peumans, 2004, Wojcik, 2009, Deibel, 2010]

In order to separate the excitons to free charges, the binding energy of exactions must be overcome. Normally, the binding energy of a delocalized exciton is given as $E_b = e^2/(4\pi\varepsilon_r\varepsilon_0 r)$, where r is the exciton radius. After the excitons are successfully separated, one of two situations can develop - either the excitons are separated into free charges or they form charge transfer excitons.[Frankevich, 1992, Deibel, 2009, Mihailetchi, 2004, Zhu, 2009, Nenashev, 2011, Arkhipov, 2004] In 1938, the first model used to describe the probability of charge-pair separation were reported by Onsager.[Onsager, 1938] Later, Braun optimized this model by considering the external application of an electrical field in the well-known Onsager-Braun model in which the balance of charge pair recombination and dissociation rates are combined giving the expression [Braun, 1984]

$$k_{diss} = \frac{\langle\mu\rangle e}{\langle\varepsilon_r\varepsilon_0\rangle} \cdot \frac{3}{4\pi a^3} \cdot \exp\left(-\frac{E_b}{k_B T}\right) \cdot \left[1 + b + \frac{b^2}{3} + \frac{b^3}{18} + \cdots\right] \tag{2.22}$$

where $\langle\mu\rangle$ is the average mobility of charge carriers, a is the thermalisation radius, E_b is the Coulomb binding energy with $E_b = e^3E/8\pi\langle\varepsilon_r\rangle\varepsilon_0 k_B^2 T^2$ in the Taylor expansion of a first order Bessel function. The model is not capable of capturing the geminate pair dissociation of materials with high charge carrier mobility due to the assumption that the mean free path of charges is much smaller than the length scale of dissociation process.

In order to solve this limitation of the Onsager-Braun model, some corrections were applied by taking into consideration hopping transport with disorder density of states and the energetics at heterojunction interfaces.[Peumans, 2004, Barth, 1997, Wojcik, 2009, Deibel, 2010, Nenashev, 2011, Rubel, 2008] The dissociation probability is given as a function of three factors: the recombination rate, particular energies of localized states and certain transition rates between hopping sites. The dissociation probability is expressed as

$$k_{dis} = 1 - \frac{\sum_{j=i}^{n-1} \frac{1}{a_{j(\varepsilon)}} \exp\left[\frac{E_j(\varepsilon) - E_1}{k_B T}\right]}{\tau_0 + \sum_{j=i}^{n-1} \frac{1}{a_{j(\varepsilon)}} \exp\left[\frac{E_j(\varepsilon) - E_1}{k_B T}\right]} \tag{2.23}$$

where $1/\tau_0$ is the recombination rate of the initial electron transition in going from site 1 to the origin, j and n are hopping sites, and E_j is the site energy.[Rubel, 2008] According to recent experimental findings, a large energy-level offset at organic-organic heterojunction and the maximization of the interface area can both benefit exciton dissociation.[Snaith, 2002, Deibel, 2010]

2.3.2 Electrical characterization of OPVCs

a. Photocurrent, dark current and open circuit voltage

The photocurrent in organic semiconductors is generated by the collection of separated charges as a result of the photovoltaic effect, which is dependent on the incident light. An important parameter for OPV cells is the short circuit current, which is related to the light density and photocurrent density as follows:

$$J_{\mathrm{sc}} = q \int b_{\mathrm{s}}(\lambda) QE(\lambda)\, d\lambda \tag{2.24}$$

where q is electrical charge, $b_{\mathrm{s}}(\lambda)$ is the incident photon flux density and $QE(\lambda)$ is the quantum efficiency (QE) of the cells. The QE is the ratio of the number of charge carrier collected by electrodes to the number of total incident photons, relevant for the characteristics of materials such as absorption coefficient and efficiency of exciton dissociation.

The dark current density (J_{dark}) flowing through the OPV cells in the opposite direction to the photocurrent that is dependent on an external applied bias in the dark. The current density under dark conditions for a photovoltaic cell behaves like an ideal diode such that:

$$J_{\mathrm{dark}}(V) = J_0\left(e^{qV/nk_BT} - 1\right) \tag{2.25}$$

where J_0 is a reverse saturation current density which is temperature dependent, k_B is Boltzmann's constant, T is temperature and *n* is the ideality factor of the diode. For a diode in the exponential region at moderate voltage, the current density in low voltage region is mainly influenced by the shunt resistance, while in high voltage region it is impacted by the series resistance. The ideality factor of the diode can be determined from derivation of the logarithm J-V current (see Fig.2.19):[Schroder, 2006]

$$\mathrm{n} = \frac{q}{\ln(10)K_BT} \cdot \frac{1}{\frac{d(\log I)}{dV}} \tag{2.26}$$

In the upper region (A) in Fig. 2.19, the relationship between the current density and the applied voltage is approximately linear,, which can be used to estimate the series resistance of the diode. For ideal OPV cells (*n*=1), the overall current is approximately equal to the sum of dark current and photocurrent. This summation is known as the superposition approximation and given by the equation [Fredrik A. Lindholm, 1979]

$$J(V) = J_{\mathrm{sc}} - J_0\left(e^{qV/nk_{\mathrm{B}}T} - 1\right) \ . \tag{2.27}$$

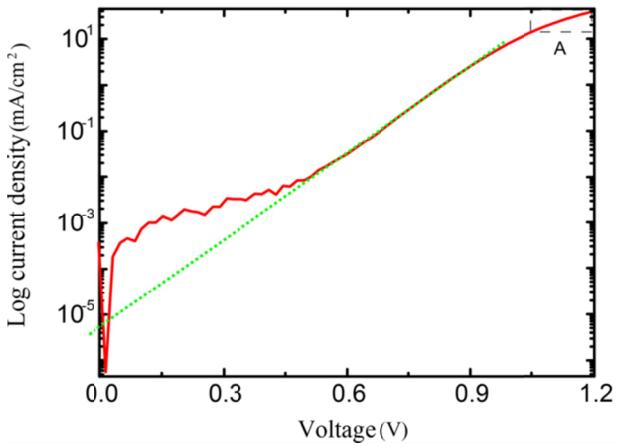

Fig. 2.19 Log-linear plot of the J-V curve for a diode. The green dash line is the slope of current density in high voltage region, which can be used to derive the ideal factor for a diode. The region A is the linear region from which the series resistance can be determined.

When the performance of OPVCs is analyzed, another important parameter the open circuit voltage (V_{oc}) is considered, defined as the maximum output potential difference under illumination when the electrodes are isolated from each other, which means there is no current flow in the device. For the ideal diode, V_{oc} is calculated from

$$V_{oc} = \frac{nkT}{q} \ln\left(\frac{J_{sc}}{J_0} + 1\right) . \tag{2.28}$$

Combining equations (2.24) and (2.28), V_{oc} increases logarithmically with light intensity and is limited by the QE which directly determines the J_{sc}.

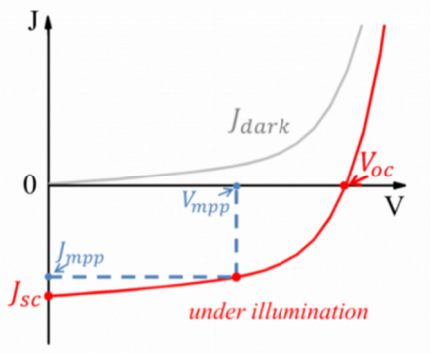

Fig.2.20 I-V characteristics under illumination and dark. J_{dark} is the current density of OPVCs under dark conditions, J_{sc} is short circuit current density, V_{oc} is open circuit voltage, J_{mpp} is the current density of maximum output power point, and V_{mpp} is the voltage of maximum output power point.

The effective operating regime of an OPV cell is in the range of positive bias, from 0 to V_{oc} and the power is given by $P = J \times V$. As shown in Fig.2.20, there is a maximum value η for $J \times V$ under illumination that is used to define the PCE which is given by

$$\eta = \frac{V_{\mathrm{mpp}} J_{\mathrm{mpp}}}{P_{\mathrm{in}}} \tag{2.29}$$

where P_{in} is the effective incident light power, V_{mpp} is the voltage of maximum output power point and J_{mpp} is the current density of maximum output power point. The PCE is also closely related to the fill factor (FF) defined by the ratio,

$$\mathrm{FF} = \frac{V_{\mathrm{mpp}} J_{\mathrm{mpp}}}{V_{\mathrm{oc}} J_{\mathrm{sc}}} \ . \tag{2.30}$$

The PCE can be expressed with FF as,

$$\eta = \frac{FF\ V_{oc} J_{sc}}{P_{in}} \ . \tag{2.31}$$

FF represents the diode properties of the PV cells. In general, a large series resistance and a relevant small shunt resistance can reduce the FF.

b. Idealized Equivalent circuit mode

The series resistance (R_{s}), composed of the resistance of the active organic absorbers and contacts between organic and electrodes, is a very important parameter which affects the maximum power and causes degradation of PV cells. The main impact of R_{s} is in reducing the FF. Therefore it needs to be kept as small as possible (see Fig.2.21a for details).The shunt resistance (R_{sh}) is also a cause for significant power losses. In particular it has a relatively stronger impact under low light intensity (see Fig.2.21b). As low shunt resistances provide an alternate current path for the photocurrent, the leads to a reduction in the output current.

In order to understand and easily analyze these characteristics of PV cells, an idealized equivalent circuit model for a bilayer device is used as depicted in Fig.2.22. [Sze, 2007] This model consists of a photon-induced current generator (J_{ph}), a diode, a shunt resistor (R_{sh}), and a series resistance (R_{s}). Frequently, R_{sh} and R_{s} are assumed to be constant, but in reality, they depend on the device current density. This is highlighted in Fig.2.19 where the slopes of J-V curve in the low and high voltage region are different, corresponding to different resistances upon the voltage increases. Considering the realistic influence of resistances on the OPVCs performance, R_{sh} and R_{s} can be approximately evaluated by J-V curve fitting. R_{sh} domains in the low voltage region, thereby can be obtained by fitting around zero bias and R_{s} is significant in high voltage region that enables the fitting around zero current density. The expressions of resistance calculation are [Schroder, 2006],

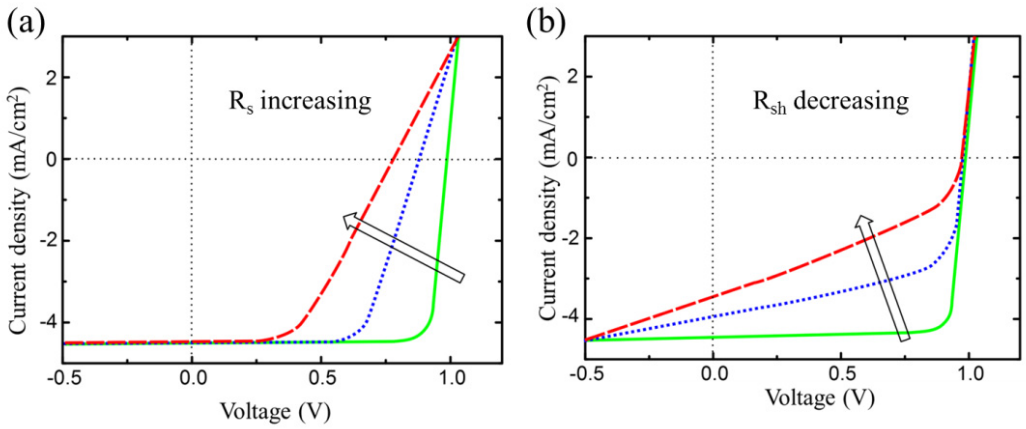

Fig.2.21 Qualitative representation of the impact of R_{sh} and R_s on the J-V performance of OPVCs. (a) The slope of the current density in the high voltage region is reduced when R_s is increased. (b) The slope of the current density in the low voltage region is increased when R_{sh} is decreased. [Nelson, 2003]

$$R_s = \frac{1}{2}\left[\frac{V_1 - V_{oc}}{AJ_1} + \frac{V_{oc} - V_2}{A(-J_2)}\right] \tag{2.32}$$

$$R_{sh} = \frac{1}{2}\left[\frac{V_3}{A(J_3 - J_{sc})} + \frac{-V_4}{A(J_{sc} - J_4)}\right] \tag{2.33}$$

where A is the device active area. A sample fit is shown in Fig.2.23.

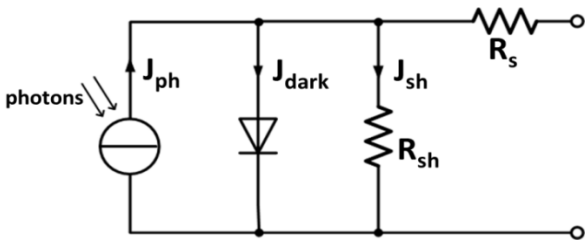

Fig.2.22 Diagram of ideal equivalent circuit model for OPVCs. J_{ph} is the photogenerated current density, J_{dark} is the dark current density of the diode, J_{sh} is the leak current density, R_{sh} is the shunt resistance and R_s is the series resistance.

With all parameters evaluated, the current density of PV cells can be generalized from the Shockley equation [Bube, 1981],

$$J = \frac{R_{sh}}{R_s+R_{sh}}\left\{J_0\left[exp\left(\frac{q(V-JR_sA)}{nk_BT}\right)-1\right]+\frac{V}{R_{sh}}\right\}-\left(J_{ph}-\frac{V}{R_{sh}A}\right) \quad (2.34)$$

where A denotes the area of the cell and J_0 is the reverse saturation current density. [Barry P. Rand and Diana P. Burk, 2007, Potscavage, 2008]

Overall, this model provides a direct and easy way to quantitatively understand the physical defects when a device shows performance worse than expectation, which can be very helpful to find ways to improve the PCE. Another method used to evaluate the R_s is fitting the dark J-V performance as shown in Fig.2.12 according to the modified Shockley equation,

$$J = J_0\left\{\exp\left[\frac{e(V-JR_s)}{nkT}-1\right]\right\} \quad (2.35)$$

where n can be obtained from equation (2.17) and the J_0 can be found from the extrapolation of linear region to zero bias. Thus, R_s can be given by the equation

$$R_s = \frac{V}{J}-\frac{nkT}{eJ}\left(\ln\frac{J}{J_0}+1\right) \quad (2.36)$$

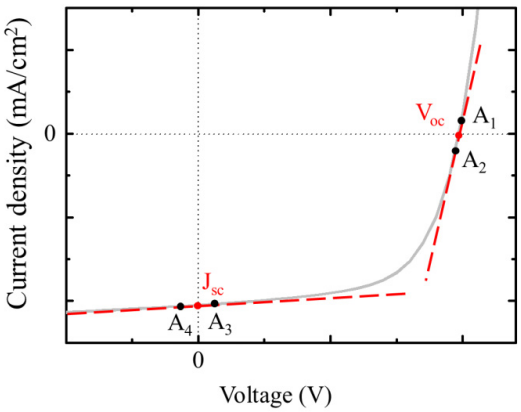

Fig. 2.23 Representation of approximate evaluation slopes of J-V curve under illumination. The series resistance is given by the slope of J-V curve around zero current density and shunt resistance is given by the slope of J-V curve around zero bias. A_1, A_2, A_3 and A_4 are the data points on J-V curve around V_{oc} and J_{sc} respectively.

Chapter 3

Methodology and materials

This chapter will introduce the methodologies used to fabricate organic films and to analyze the performance of these devices, as well as all materials used for films and devices fabrication. Spin coating is used to prepare organic films from solution and GLAD is used to fabricate vertical aligned nanocolumn structure to be used in the fabrication of OPVCs. Scanning electron microscopy and atomic force microscopy are the two main methods for investigating films topography. Ultra-violet/visible absorption microscopy is to explore the absorption behavior of different materials and different film architectures.

3.1. Methodology

3.1.1 Spin coating

Spin coating has been employed in the preparation of thin film coating with soluble materials for many years. The procedure offers better controllability during coating, good reproducibility, is applicable for large area substrate and is low cost. The process of film formation by spin coating is illustrated in Fig. 3.1. The excess solution on the flat surface of the substrate is ejected upon acceleration by plane rotation due to the action of centrifugal force, resulting in the formation of a homogeneous thin film of coating material at high speeds. The final thinning of the film follows the same steps as in polymer thin film formation.

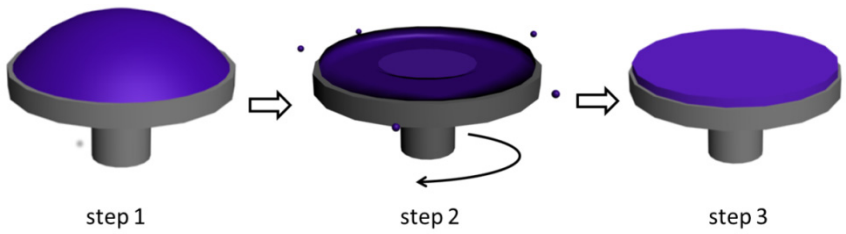

Fig.3.1 Schematic drawing of spin-coating process. Step 1: depositing the solution on the plane. Step 2: acceleration to the setting rotation speed and film thinning by radial flow of the solution. Step 3: thin film formed with further drying.

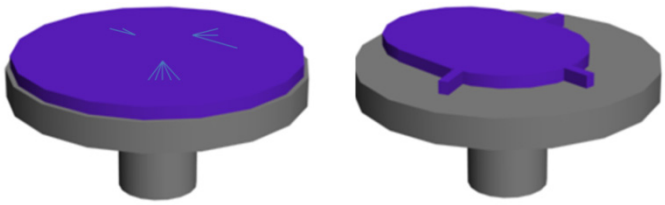

a) steaks in the film b) nonuniform film

Fig.3.2 Schematic drawing of the deviation from ideal spin coating; a) Steaks in the film most likely induced by unclean matter on the substrate. b) Non-uniform film due to the imperfect wetting characteristics.

The first report with regards to a theoretical model for the spin coating process was presented by Emslie et al in 1958, [Emslie, 1958] in which they showed a reasonable correlation between spin coating process and the resulting film thickness, although some impacts on the thickness during spin-coating were ignored. An improved model was later formulated that considered rest impact factors, showing correspondence between simulation and experimental results.[Meyerhofer, 1978, Jenekhe, 1984, Flack, 1984, Sukanek, 1985, Bornside, 1987, Lawrence, 1988] To simplify the simulation process, spin coating was divided into two stages. In the first stage, the solvent evaporation is neglected, therefore, the solution concentration is constant. Thus the rate of the change of film thickness h can be described by [Emslie, 1958]

$$\frac{\mathrm{dh}}{\mathrm{dt}} = -\frac{2\rho\omega^2 h^3}{3\eta_0} \tag{3.1}$$

where t is rotation time, ρ is solution concentration, η_0 is initial solution viscosity and ω is rotation speed. In the second stage of the simulation process, solvent evaporation is considered, and consequently, the film thickness is calculated from [Bornside, 1987]

$$h_f = (1 - x_0)\left[\left(\frac{3\eta_0}{2\rho\omega^2}\right)k(x_1^0 - x_{1\infty})\right]^{\frac{1}{3}} \tag{3.2}$$

where x_0 is the initial solvent mass fraction (SMF) in the solution, $x_{1\infty}$ is SMF in equilibrium state with that of in gas phase and k is mass transfer coefficient.

Through comparison of results from simulations and experiments, the polymer film thickness fabricated by spin coating is shown to be primarily controlled by the solution viscosity, the rotation rate of the plane, as well as polymer concentration in solution which is related to viscosity. Using a faster rotation speed or lowering the viscosity of the solution can lead to thinner films. Furthermore, other parameters that could influence the film formation include solvent evaporation rate, the initial amount of solution and the history of acceleration

prior to the final rotation speed, etc. In addition, film formation is also affected by the substrate conditions such as the cleanness and hydrophobicity of the substrate, as illustrated in Fig.3.2.

3.1.2 Glancing angle deposition

Glancing angle deposition (GLAD) is a physical vapor deposition technique that exploits ballistic self-shadowing effects during island growth and is used to fabricate high ordered nanostructure arrays originating from oblique angle deposition. The oblique angle deposition (see Fig.3.3) was first used by Knorr and Hoffman to produce magnetic anisotropy in iron films. [Knorr, 1959] Subsequently it was applied to produce inorganic porous microstructures through the precise control of substrate rotations as stipulated for GLAD,[Robbie, 1995, Messier, 1997]. The application of GLAD in fabricating organic nanostructure has drawn broad attention since Hrudey et al. presented results concerning the anisotropic optical properties for arrays constructed of tris(8-hydroxyquinoline)aluminum.[Hrudey, 2006a, Hrudey, 2006c]

The mechanism for column structure formation is a complex process that can be affected by many factors, such as substrate roughness, rotation rate, temperature, diffusion properties on the target substrate of evaporated materials, vapor beam incident angle, deposition rate and vacuum pressure. These factors interact and contribute together to the final morphology of column structure, meaning that it is difficult to have one appropriate mode covering all factors. Therefore, the mechanism with limited assumptions is reviewed here.

In the first stage of oblique incident angle deposition on a stationary substrate, film nucleation randomly form on the substrate surface, growing into small columns and developing shadows as shown in Fig.3.4a. During subsequent deposition, a large fraction of the flux is captured by taller grains that continue growing at the expense of their dying neighbors (see Fig.3.4b). The shadowing effect was verified as a key parameter in oblique angle deposition since 1960 reported by Smith and his co-workers[Smith, 1960] indicating that on a stationary substrate, the valleys formation between columns was induced by the shadow of neighboring atoms. Due to the oblique incident angle, the evaporated atoms are unable to reach the space on the substrate under the shadow of the columns (see Fig.3.5b). In the meantime, Smith *et al* also found that the tilted angle β of the column were always smaller than the oblique incident angle α. In a small oblique angle ($< 60°$), the relationship between α and β follows the tangent rule [Nieuwenh.Jm, 1966],

$$\tan\alpha = 2\tan\beta. \tag{3.3}$$

If the oblique angle was increased to larger than $60°$, ballistic model was applied[Tait, 1993],

$$\beta = \alpha - \arcsin\left(\frac{1-\cos\alpha}{2}\right) \tag{3.4}$$

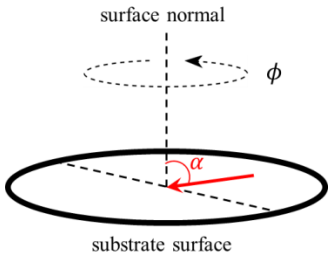

Fig. 3.3. Definition of oblique incident angle deposition. The red line with arrow end is the evaporated molecular beam and the angle between the beam and surface normal α is defined as incident angle, the substrate could be rotated above its surface normal, the substrate rotation rate is ϕ.

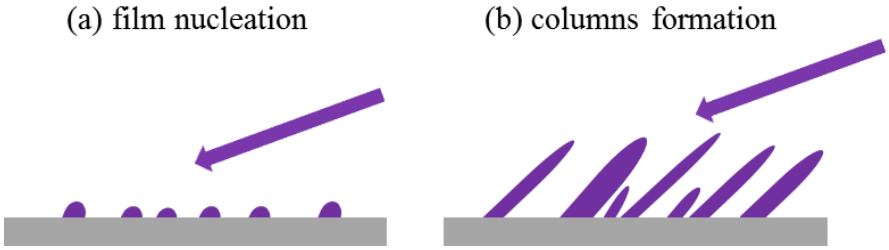

Fig.3.4 Schematic representation of columns formation procedure. (a) Film nucleation formed on the substrate at the beginning of evaporation. (b) Development of column structures.

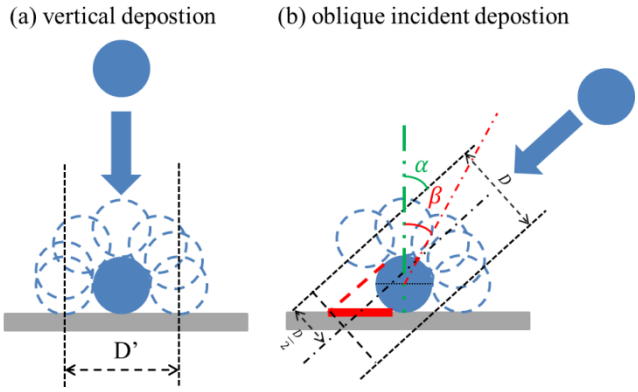

Fig.3.5 Schematic representation of growth modes of (a) vertical deposition and (b) oblique incident deposition and ballistic mode[Dirks, 1977]. Blue discs denote atoms, blue dash circles denote the possible attaching positions for coming atoms, grey squares denote substrate, green dash-dot line denote surface normal, α is the incident angle, β denote the column tilt angle, D is the center diameter of the possible positions and the thick red line on the substrate denotes the shadow space. This figure is reproduced from [Abelmann, 1997b]

Another explanation for the phenomenon (when $\beta < \alpha$) was proposed by Kambersky et al.[Kambersky, 1961] suggesting that all atoms with an oblique incident angle moved towards the surface normal when they reach the column tops due to the retaining parallel momentum to the substrate surface. However, this explanation is unable to distinguish between the contribution to movement from either parallel momentum or random diffusion. In any case, as mentioned previously, these modes are only capable of giving a first approximation of column formation with oblique incident angle deposition. The approximation is limited as β is dependent on many other features during preparation such as surface roughness, temperature and evaporation rate, etc.[Nakhodkin, 1972, Hashimoto, 1982, Hagemeyer, 1993, Lintymer, 2003]

A column deposited by oblique incident angle on a stationary substrate always shows textural anisotropy due to the shadow effect. If continuous substrate rotation rate were to be applied in conjunction with oblique incident angle then the shadowing anisotropy can be corrected, thus leading to vertically aligned column structures[Zhang, 2007a, Robbie, 1996, Abelmann, 1997a]. The diameter of a GLAD column is to some extent larger than that prepared without substrate rotation. By taking into consideration the surface diffusion, the column diameter can be described by a power law [Karabacak, 2003, Cetinkaya, 2008, Kaminska, 2005],

$$w(t, \alpha) \propto t^{p(\alpha)} \tag{3.5}$$

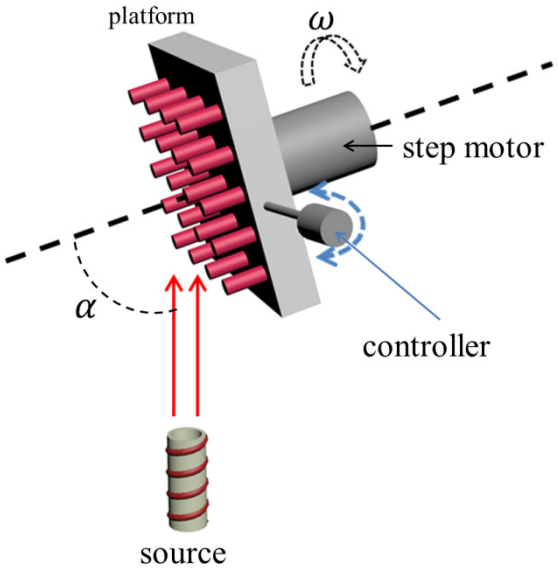

Fig. 3.6 Schematic drawing of GLAD system in vacuum chamber. The bottom crucible is source heated with a tungsten filament, the back rod is the step motor controlling substrate rotation about the surface normal and the side rod is the controller attached on the substrate platform that tunes the angle of oblique incident molecular beam α.

where w denotes column width, t denotes film thickness and p is a growth coefficient depending on the incident angle α and the material. However, the relation between growth coefficient and incident angle is still not clear and must be defined on a case by case basis. As such, the final column diameter is difficult to measure. In addition, the crystal structure of materials is also affected by the depositing incident angle, leading to changes in the crystal main axis as a result of GLAD to comparison to negligible effects from vertical deposition. In vertical deposition there is only a reference plane-substrate surface, while in GLAD the oblique incident beam acts as an additional reference plane. During deposition, the crystal orientation with respect to both reference planes is important. [Volmer, 1921] The origin of this phenomenon is the subject of much debate. One suggestion is that it can be induced by the surface dynamic equilibrium as qualitatively measured by the condensation coefficient [Francombe, 1964]. Another study has emphasized the preferential growth orientation, called evolutionary selection, as the main cause of this phenomenon [van der Drift, 1967].

Due to limited physical knowledge, the mechanism for column structure formation is still not fully understood. A universal rule that summarizes the large collection of experimental observations is difficult to define as there are always exceptional observations disobeying the former modes. To enhance the controllability of the morphology of column structures formed, further experimental and theoretical studies are necessary.

In this work, a home-made glancing angle deposition system was used as shown in Fig.3.6. The substrate is fixed on a platform attached to a controller that was used to manipulate the incident angle of the molecular beam α. On the back of the platform, a step motor was mounted to control the substrate rotation rate ω about the surface normal. In most cases, the deposition was started under high vacuum condition ($< 10^{-6}$ mbar). Under exceptional conditions, the pressure was decreased to 10^{-3} mbar by filling the chamber with Argon gas to reduce the mean free pass of evaporated molecules.

3.1.3 Scanning electron microscopy

The first reported application of scanning electron microscope (SEM) was in 1942 by Zworykin, who presented topographic contrast provided by emitted secondary electrons. [Goldstein, 2003] In 1965, the first commercial SEM was developed by Pease and Nixon with significant improvement of the spatial resolution.[Breton, 1999] Nowadays, the SEM is an extremely useful approach for imaging and analyzing the structure and surface morphology of materials. A simplified SEM instrument structure is shown in Fig.3.7a.

In the SEM, a focused electron beam interacts with a specimen leading to a number of particle and radiation emissions such as backscattered electrons (BSEs), secondary electrons (SEs) and x-rays, etc. (see Fig. 3.7b). Electrons produced at a cathode are accelerated through a voltage difference of 0.1-50 KV between the cathode and the anode of the device. The electron probe that reaches the surface has a diameter of 1-10 nm, with the diameter

controlled by a series of electromagnetic lenses in conjugation with apertures.[Reimer, 1998] "Scanning" is achieved by controlling the magnetic field generated by the coil system that allows for the sweeping of the focused electron beam across the specimen surface. The incident electrons interact with the sample and in doing so lose some of their kinetic energy due to elastic or inelastic collisions. This then leads to the emission of electrons and x-rays from the sample.[Reimer, 1998] Among the varieties of electron emissions, SEs are produced as a result of the inelastic collisions between incoming electrons and weakly bound electrons in the conduction band. The SEs are collected with the Everhart-Thornley detector and subsequently used to create images of the topographic features of the specimen. Image quality is a function of the SEs yield, enhanced edge effect emission (Fig. 3.8) and small particles, and partial collection due to the shadow on the surface.

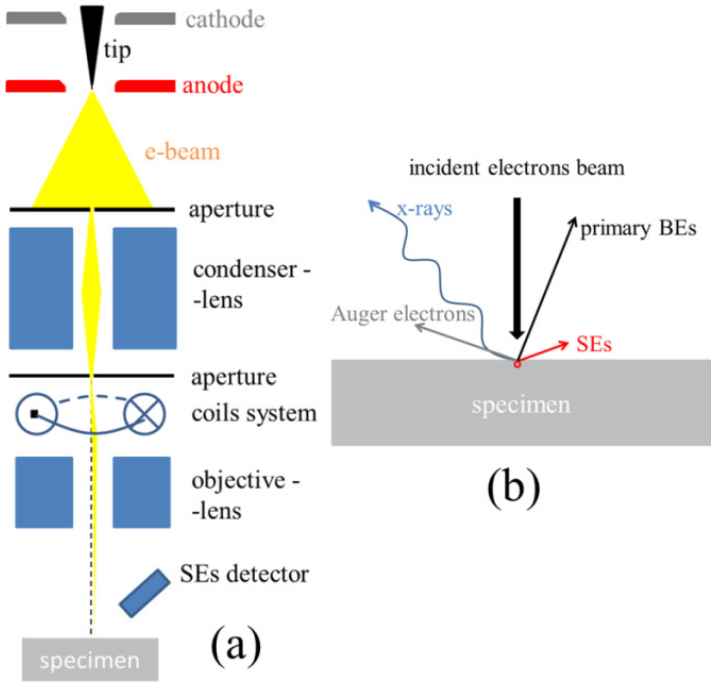

Fig.3.7 (a) Schematic representation of the SEM instrument. Bottom grey square is the specimen placed in vacuum. The SEs detector is the secondary electron detector, yellow beams are (manipulated) electron beam, the upper black triangle tip is electron gun tip in between a cathode and anode, the condenser-lens and apertures are used to assist to focus the electron beam and control the electron beam radius, coils system in the middle is to tune the direction of electron beam which is used to change to investigation position on specimen. (b) Primary interaction between incident electrons and the specimen. The SEs are the secondary electrons and BEs are the backscattered electrons.

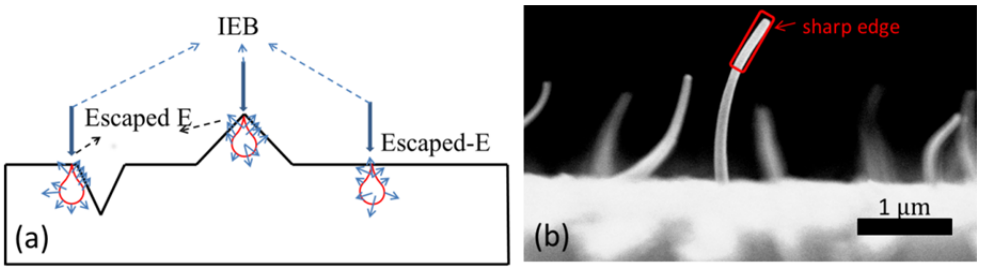

Fig.3.8 (a) Enhanced SEs emission due to edge effect. The IEB is the incident electron beam, the escaped E represents escaped electrons, the red unfilled balls under the surface are volumes of injected electrons and the blue arrows are electron escape directions. (b) A SEM micrograph example showing the edge effect.

The SEs yield mainly depends on the chemical composition of the sample and the tilt angle of the surface element with respect to incoming electrons, as well as incident electron energy. Owing to their low exit energy, less than 50 eV, electrons can escape from only a few nanometer depths below the specimen surface. At the specimen edges, more secondary electrons can leave the specimen surface compared with that of flat area as shown in Fig. 3.8. Therefore, the areas around edges appear brighter in images.

In this work, the HITACHI S-4100 SEM with cold field emission gun was used to investigate samples' topography and lateral structure. The accelerating voltage can be varied between 0.5 and 30 KV. The maximum resolution that can be reached is 1.5 nm. In order to obtain high resolution images, before investigation a 10 nm thick gold layer was usually sputtered onto specimens.

3.1.4 Scanning force microscopy

The scanning force microscope (SFM) invented by Binning et al in 1986 was developed from the scanning tunneling microscope,[Binnig, 1986] and allows for the study of the surface topography with sub-molecular resolution. The basic principle of the SFM is to measure the attractive or repulsive force between the sharp tip mounted on a flexible cantilever and the surface of solid film on an atomic scale of nanometers. A schematic representation of SFM operation process is shown in Fig. 3.9.

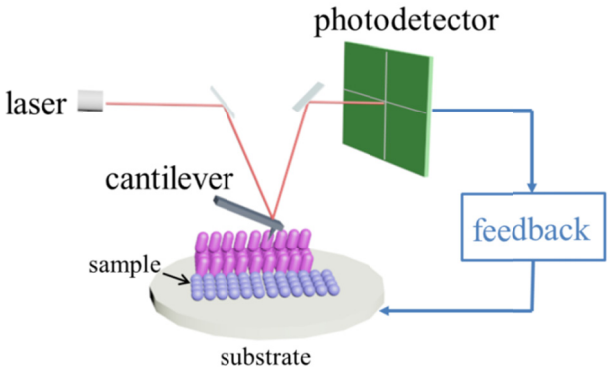

Fig.3.9 Schematic representation of SFM operation. Blue ball/purple rods represent molecules on the substrate, red lines are laser beams, feedback is data collection system controlled by computers and two plate squares between laser and photodetector are minors. The laser beam emitted from the laser diode shines on the tiptop of cantilever and is reflected to the photodector, while the collected optical signal is translated to an electrical signal by the controller.

During scanning, an accurately controlled tip moves line by line, and the laser beam line bounced off the back of the cantilever is captured by a four-segment photodetector. The cantilever deflections due to its bending are detected on an Angstrom spatial scale (optical lever principle) and converted into electrical signals for mapping.[E. Meyer, 2003] While scanning the interaction between the tip and sample surface is principally due to two forces: long-range and short-range forces. Recall that the Lennard-Jones potential $\varepsilon(r)$ is given by the expression

$$\varepsilon(r) = -4\varepsilon_0\left[\left(\frac{\sigma}{r}\right)^6 - \left(\frac{\sigma}{r}\right)^{12}\right] \tag{3.6}$$

where ε_0 is potential energy at the minimum, r is tip-sample distance and σ is effective molecular diameter. The interaction force F is given as the derivative of the Lennard-Jones potential by

$$\mathrm{F}(r) = -\nabla\varepsilon(r) = -4\varepsilon_0\left[12\left(\frac{\sigma}{r}\right)^{13} - 6\left(\frac{\sigma}{r}\right)^{7}\right] \tag{3.7}$$

The two terms in the equation 3.7 refer to long range force dominated by van der Waals' force $\sim r^{-7}$ and repulsive force $\sim r^{-13}$ in short displacement[Cappella, 1999].

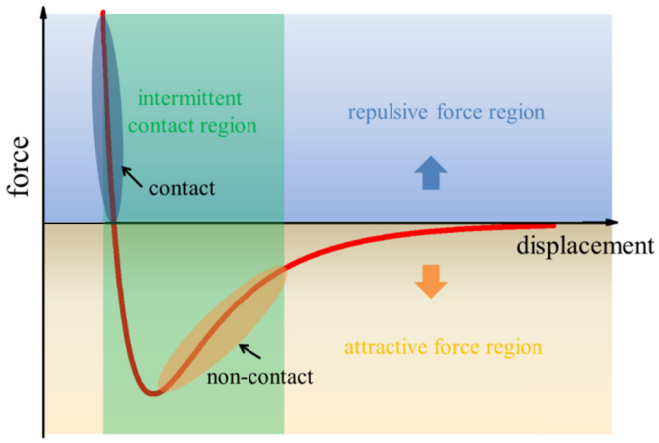

Fig.3.10 Interaction between tip and the sample surface for a SFM dependent on distance defined by derivative of Lennar-Jones potential. Contact and non-contact regimes are highlighted respectively. In between these two regimes lies the intermittent contact region.

There are several techniques based on the SFM operation principle, such as contact mode, non-contact mode and tapping mode. The tapping mode was used in this work for investigating surface morphology of molecular and polymer films. In tapping mode, the cantilever driven by piezo crystals is forced to vibrate in the intermittent-contact region indicated in Fig. 3.10 with reasonable setting amplitude typically in the range of tens of nanometers. During scanning on an undulating surface, the cantilever is bent due to the interaction force. To follow the surface topography with the cantilever tip the following approach is used. The deflection of reflected laser beam induced by the bending of cantilever is detected and then used in a feedback loop to control the tip movement up and down in z-direction in order to keep the amplitude constant. Subsequently, the mapping of morphology is based on the scanner's motion in z-direction. At the same time, surface roughness, which can be deduced from 3D AFM topography statistics, can be used as a quantitative description of height variations on the surface topography. The principle parameter for quantifying the surface morphology is the root mean square roughness (rms), expressed by the deviation of the data in the *z*-direction:

$$R_{rms} = \sqrt{\frac{1}{N}\sum_{j=1}^{N}\left(z_j - \bar{z}\right)^2} \tag{3.8}$$

where z_j is the height value of pixel j of the surface $z = z(x, y)$ in the AFM image comprising N pixels and $\bar{z}$ is the mean height value : $\bar{z} = \frac{1}{N}\sum_{j=1}^{N} z_j$. Another important parameter is the 3D surface area of the entire image that can also be calculated from the root

mean square roughness. The entire surface area is the sum of the area (s_i) of all of the triangles formed by three adjacent data points,

$$s_i = \frac{1}{2}\sqrt{a^2c^2 - \left(\frac{a^2+c^2-b^2}{2}\right)^2} \tag{3.9}$$

$$S_{tatal} = \sum_{i=0}^{N-2} s_i \tag{3.10}$$

where a,b,c are displacements of each three adjacent points (x_i, y_i, z_i), (x_{i+1}, y_i, z_i), (x_i, y_{i+1}, z_i) respectively.

In addition, the oscillation of tip only allows it to impinge the sample surface at the lowest point periodically; thus, scanning operates in the attractive force region for most of the time but only a short fraction of time in the repulsive region. Therefore, the lateral forces in tapping mode are much lower than in the contact mode. This feature makes the tapping mode appropriate for soft matter scan without damaging the sample surface such as organic molecules. In this work, Bruker Multimode-8 AFM is used to investigate the morphology of the most samples.

3.1.5 Ultraviolet/visible absorption spectroscopy

In general, ultra-violet/visible (UV-Vis) spectroscopy is a technique allowing one to access information concerning the absorption and scattering characteristics of a given sample. A simplified description involves a sample being placed between a monochromatic light source and a photodetector, with the intensity of light beam measured before and after passing through the sample. After extraction of the "background" (substrate or cuvette with solvent), the extinction spectrum is plotted as a function of wavelength.

As discussed in chapter 2, for a single molecule, the absorption corresponds to the excitation of outer electrons mainly the $\pi - \pi^*$ transition and $n - \pi^*$ transition. For an organic solid, the absorption is the sum of the absorptions of each molecule. Thus, the extent and intensity of absorption are both dependent on the molecular electronic structure and the number of molecules that absorb light of a given wavelength. This can be described by the Beer-Lambert law which states that the transmittance (T) of light through a substance is dependent on the extinction coefficiency (ε) of the substance and the distance (L) the light travels through the substance as given by

$$\mathrm{T} = \frac{I}{I_0} = 10^{-\varepsilon c L} \tag{3.11}$$

where I_0 is intensity of the incident light, I is intensity of light transmitted through the substance, c is concentration of the substance. For a given molecule, α is constant at a

specific wavelength and the product εcL defined as the absorbance (A), which can be read from the spectrum directly, is given as

$$\mathrm{A} = -LogT = Log\frac{I_0}{I} \tag{3.12}$$

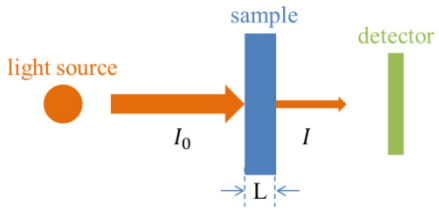

Fig.3.11 Schematic representation of the Beer-Lambert law. The orange ball is light source and the orange arrow bars represent the light rays.

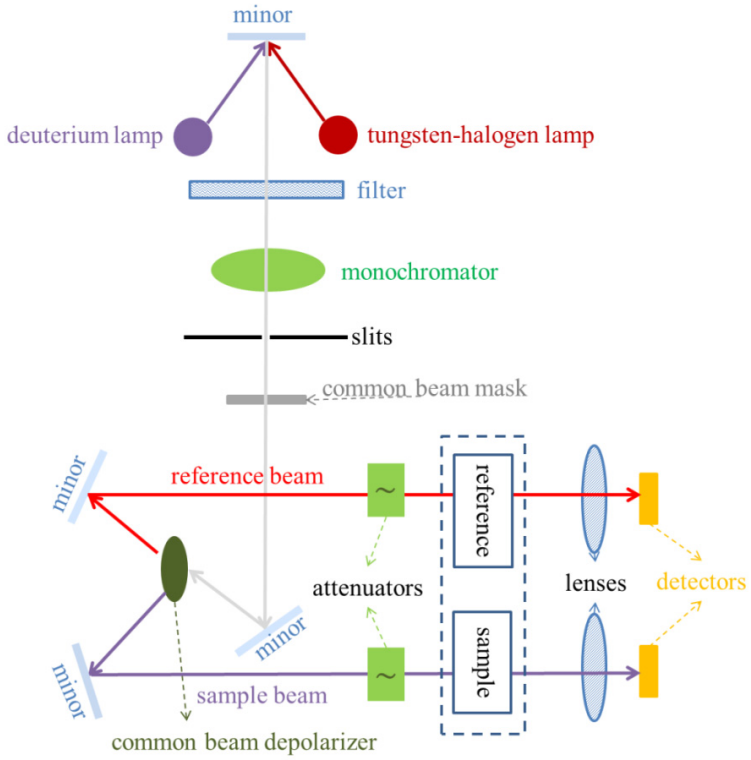

Fig.3.12 Schematic representation of PerkinElmer lambda 900 spectrometer. Grey lines with arrows in front are light beams. The upper purple and dark red balls are deuterium and tungsten-halogen lamp respectively. The light is converted to a monochrome source by a filter and monochromator. Subsequently the focused monochromatic light is split into two light beams by a common beam depolarizer. The two light beams are then recalculated by attenuators to ensure equal light intensity output.

In principle, the absorption peaks of given molecules in UV-Vis spectrum should be sharp as the energies of the electronic transitions are constant. However, common spectra show broad peaks rather than sharp peaks. This is due to discrete vibrational energy levels and rotational energy levels at each electronic energy level where transitions may also occur.

Prevalently throughout this work, measurements of absorption were carried out with a PerkinElmer lambda 900 spectrometer with the instrument structure is shown in Fig. 3.12. The setup is also capable of measuring the absorption of infrared region at a wavelength of 3000 nm, which allows for the investigation of the polaronic absorption induced by molecular doping in polymer. In order to minimize the error due to substrates difference, calibration is necessary prior to measure UV-Vis spectroscopy for reference substrate and the sample substrate before using.

3.2 Materials

In this section, the materials used to fabricate OPVs and the experimental conditions are introduced. Additionally, sample preparation and measurements will be illustrated in detail.

3.2.1 Organic materials

Pentacene (PEN) (99%), fullerene (C60) (99.9%) and bathocuproine (BCP) (96%) purchased from Sigma-Aldrich were used directly without sublimation. [6.6]-phenyl-C61-butyric acid methyl ester (PCBM) was purchased from American Dye Source, Inc. Tetrafluorotetracyanoquinodimethane (F4-TCNQ) (≥98%) was purchased from Tokyo Chemical Industry co. LTD. Znic phthalocyanine (ZnPc) and diindenoperylene (DIP) were twice sublimated. Ploy (3,4-ethylenedioxythiphene):poly(styrenesulfonate) (PEDOT:PSS) were purchased from H.C. Stark GmbH&Co. KG. Purified polyfuran was provided by Bendikov group (Weizmann institute of science).

a. Organic materials for column structure

As mentioned in section 3.1.2, the morphology of column structures grown with GLAD is also dependent on the properties of organic materials such as the diffusion length and crystalline characteristics. In this work, PEN and DIP were chosen and their chemical structures are depicted in Fig.3.13 (a) and (b) respectively.

PEN is one of the most intensively investigated conjugated organic molecules over the past several decades due to its importance in organic electronic devices applications. Considering high charge carrier mobility for holes and low mobility for electrons, PEN has been used as a good donor material for OPVCs.[Salzmann, 2008] Furthermore, singlet fission discovered recently in PEN film, which could increase the quantum efficiency significantly, makes PEN a much stronger candidate. With appropriate deposition rate, molecular beam incident angle and substrate rotation rate, the columnar structure on indium tin oxide (ITO) substrate is achievable. [Witten, 1981, Meyer zu Heringdorf, 2001a, Ruiz, 2003a, Ruiz, 2003b, Abelmann, 1997b, Zhang, 2007a]

DIP has drawn great attention since its application on OPVs owing to its advantage of having a long exciton diffusion length.[Wagner, 2010, Stübinger, 2001, Dürr, 2002, Heinemeyer, 2008a, Kurrle, 2008, Meiss, 2010] Appropriate crystalline structure and stability in ambient conditions make DIP a good candidate for fabricating column structures. Furthermore, lying phase DIP, which enhances the absorption, has been found in column structure layers by x-ray diffraction spectroscopy (XRD).

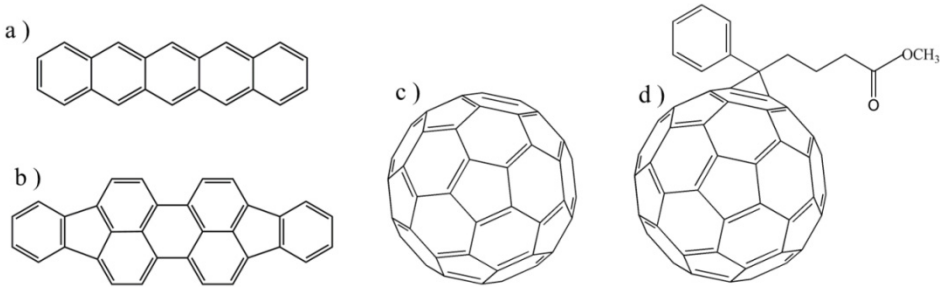

Fig.3.13 Chemical structure of organic materials as donors and acceptors for OPVs; (a) PEN; (b) DIP; (c) C60; (d) PCBM.

b. Other functional organic materials

C60 consisting of 12 pentagons and 20 hexagonsone is one of the most promising *n*-type semiconductors and has been applied widely in the field of organic electronics (Fig.3.13c). [Kroto, 1985, Itaka, 2006, Wang, 2006] The PCBM (Fig.3.13d) is one of the most commonly used polymers as an acceptor for solution processed OPVs. The solubility of PCBM is improved by adding the side group, and to a large extent the electronic properties of buckminsterfullerene are preserved. F4-TCNQ (Fig.3.14a) is a strong acceptor small molecule that is broadly used for the *p*-type doping of materials in organic electronics to manipulate the energy alignment and improving conductivity.[Gao, 2003, Aziz, 2007, Sun, 2009, Lu, 2013, Pingel, 2013]

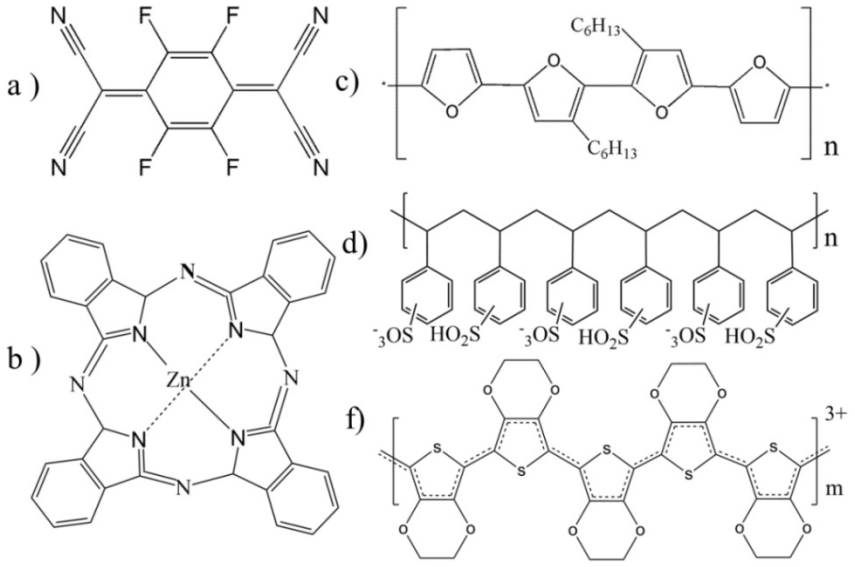

Fig.3.14 Chemical structures of organic materials; (a) F4-TCNQ; (b) ZnPc; (c) polyfuran (one monomer); (d) PSS; (f) PEDOT.

Polyfuran is a *p*-type highly conductive conjugated polymer with electrical and optical properties similar to P3HT, with the chemical structure shown in Fig.3.14c. However, due to the difficulties in their synthesis, it has been the subject of less attention than P3HT.[González-Tejera, 2008, Ferron, 2012] ZnPc has been extensively studied as a promising semiconductor material for OPVs, exhibiting good absorption in visible region and a high value of exciton diffusion length.[Amsalem, 2009, Hong, 2007, Pfuetzner, 2011, Senthilarasu, 2007, Zeng, 2010] BCP, in this work, is treated as exciton-blocking layer between acceptor and cathode, as well as a protection layer preventing damage due to metal evaporation.[Chan, 2006, Lo, 2010, Vogel, 2006a, Gommans]

3.2.2 Holes transport material

In the field of OPVCs, PEDOT:PSS is one of the most commonly used holes transport materials that is transparent and highly conductive, and it consists of PEDOT and PSS in various ratios. The chemical structures are shown in Fig.3.14 (d) and (f). [Drury, Halik, 2002, Groenendaal, 2000, Kirchmeyer, 2005] This highly conductive polymer is neutral since the positive charges on PEDOT are stabilized by negative charges on PSS and the conductivity can be tuned by employing various ratios of PEDOT in the mixture, ranging from 10^{-5} S/cm to over 100 S/cm. Although PEDOT is hydrophobic, the PEDOT:PSS can form agglomerates in aqueous dispersion, assisted by dressing hydrophilic PSS.[Jukes, 2004, Greczynski, 1999]

PEDOT:PSS thin film can be easily prepared by spin coating under ambient conditions, with the thickness controllable. The value of work function (ϕ) of PEDOT:PSS film is significantly impacted by water contamination, thus in order to obtain high ϕ for reducing injection barrier, an annealing process is necessary to remove the residual water before fabricating devices.[Koch, 2007c]

In this work, three types of PEDOT:PSS were used: CH8000 (weight ratio is 1:20), AI4803 (weight ratio is 1:6) and HIL1.3 (fluorinated derivative of the stand PEDOT:PSS) respectively. [Wilke, 2013]

3.2.3 Electrodes and substrates for OPVCs

In this work, glass substrates with patterned ITO (purchased from Thin film Devices Inc. and Präzisions Glas & Optik GmbH) were used for OPVs fabrication and ITO was treated as the bottom anode with a sheet resistance of 20 Ω/sq. The average thickness of ITO layer is about 120 nm and the roughness is approximately 2 nm. For absorption measurement, quartz glass (Präzisions Glas & Optik GmbH) substrates were sometimes used instead of ITO to reduce the influence of light scattering. The pre-cleaning procedure of all the substrates is as follows. First the substrates were scrubbed with diluted Hellmanex solution, then rinsed with

deionized water and blown dry with N_2 gas. Next they were sonicated for 10 min in acetone and isopropanol respectively and then blown dry again. In the application of OPVs, prior to use, Ultraviolet-ozone (UV-ozone) treatment for more than 30 minutes was applied to improve the wetting of the substrate by an aqueous suspension of the intrinsically conducting polymer PEDOT:PSS.[Destruel, 2006, Lo, 2013] Moreover, the ozone treatment can also affect ITO surface work function by increasing the oxygen concentration on top of the surface.[Sugiyama, 2000, Destruel, 2006] The prototypical morphology of an ITO surface is presented in Fig. 3.15 with the average rms for all ITO substrate being approximately 2 nm. Additionally the ITO substrates were pre-patterned with pure HCl etching to define the device active area.

The top electrode (cathode) used for some devices is samarium (Sm) exhibiting a relatively low work function of approximately 2.8 eV and was investigated in ultra-high vacuum condition ($< 10^{-9}$ mbar) with UPS.[Koch, 2002] The low work function is to some extent sufficient for charge collection in OPVCs and results from high energy offset between the cathode and anode leading to a high extraction electrical field. However, a crucial issue with using Sm as the top electrode is that Sm is sensitive to oxygen and can very easily be oxidized. Therefore, the J-V characteristics of the devices with Sm were measured in an inner environment (high vacuum or glovebox).

Alternatively, a widely used top electrode material is aluminum (Al) with a work function about 4.1 eV.[Koch, 2000] However if using Al as the cathode of OPVCs electron blocking layer or protection layer is needed due to the issues of exciton quenching occurring at the organic/Al interface with Al atoms diffusion taking place during deposition. [Vogel, 2006a, Gommans, 2008, Wagner, 2012]

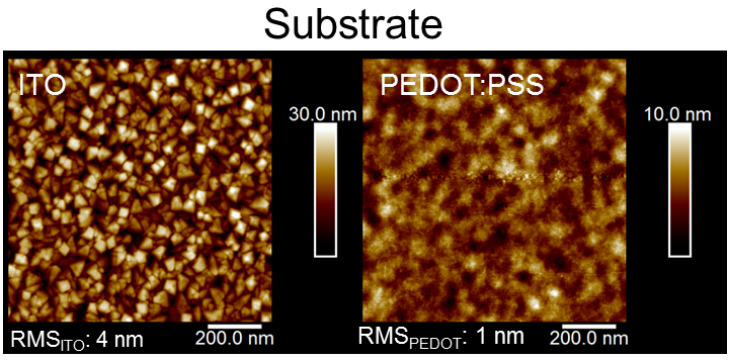

Fig.3.15 The typical morphology of ITO and PEDOT:PSS substrates investigated by AFM. The value of rms are 4 nm and 1 nm respectively.

Chapter 4

Results and discussion

This chapter is divided into three sections based on the materials and methods employed to fabricate OPVCs. The first section will focus on presenting vertically aligned pentacene nanocolumn architecture grown by GLAD and its application in OPVCs. The second section will illustrate the experimental and measurement results of DIP column structure on different substrates and their application in OPVCs. Compared to bilayer heterojunction devices, the performance of OPVCs utilizing nanocolumn structure improved owing to interface area enlargement and enhanced absorption by effectively using a thick organic film. The last section will demonstrate the process of molecular doping in polymer film with F4-TCNQ employed as the dopant. The results of molecular doping in OPVCs are then introduced.

4.1 Pentacene nanocolumn and application in OPVCs

4.1.1 Introduction

OPVCs have been extensively studied since the first study of bi-layer donor/acceptor heterojunction devices.[Tang, 1986] Significant improvement in power conversion efficiency was achieved through the production of bulk heterojunctions (BHJ) from solution processed conjugated polymer/fullerene mixtures. The BHJ morphology enables large interface areas between donor and acceptor material that facilitates efficient exciton dissociation.[Yu, 1995, Halls, 1995, Peumans, 2003a] At the same time, if the donor/acceptor phase separation length scale is on the order of the exciton diffusion length, losses due to excition recombination can be minimized.[Peumans, 2003a, Halls, 1995, Yu, 1995] However, in such random blends charge carrier mobility may be low, charge trapping at morphological bottlenecks can quench excitons, and dead-ends in the conduction pathway may build up unwanted space charge. Hence, a vertically interdigitated array of densely packed alternating donor and acceptor columns with a diameter in the range of the exciton diffusion length sandwiched between the electrodes could eliminate above problems and thus maximize OPVC efficiency.[Yang, 2005, Zheng, 2009a] A suitable lithography-free method to fabricate such organic vertically aligned nano-columnar structures is GLAD, which is a physical vapor deposition technique that exploits self-shadowing effects during island growth.[Hrudey, 2006b, Zhang, 2007b] In GLAD, a molecular beam is directed under a glancing angle (α) onto the substrate, which simultaneously rotates about its surface normal. This results in the growth of vertical columnar structures, whose morphology can be controlled by variation of α and substrate

rotation rate (ω), as well as the substrate surface energy, morphology, and temperature.[Abelmann, 1997a, Zhao, 2002, Robbie, 1997]

In this section the growth of vertically aligned crystalline nanocolumn arrays (NCAs) of PEN by GLAD is examined and their beneficial effects for OPVCs compared to devices with PEN donor layers grown by conventional (normal incidence) molecular beam deposition. The interdigitated donor/acceptor active layer was produced by filling the void volume around the PEN nanocolumns with the acceptor PCBM from solution, since evaporation of the acceptor would likely lead to holes due to shadowing of the molecular beam. Further device performance improvement was achieved by inserting a thin PEN electron-blocking layer prior to NCA growth to prevent electron current leakage to the anode. Lastly, the possibility of depositing C60 as acceptor on PEN nanocolumns for interdigitated bulk heterojunction is investigated.

4.1.2 PEN nanocolumn

The formation of nanocolumns is caused by the shadowing effect of molecular islands with respect to the incoming material flux, aggravated by the large oblique incident deposition angle. During deposition a large fraction of the flux is captured by taller grains that continue growing at the expense of their dying neighbors. As discussed in chapter 3, the morphology of column structure is determined by several parameters, such as incident angle (α), substrate rotation rate ω and the features of substrate, as well as features of the materials. In this work, the influence of each individual parameter on column structure with PEN is investigated. Figures 4.1.1b-d show representative topography and cross-section micrographs of PEN columnar structures grown by GLAD on ITO. Compared with the typical flat and homogeneous morphology of vertically deposited PEN thin films on ITO, displayed in Fig. 4.1.1a, almost square shaped crystalline PEN nanocolumns with large gaps between them persist after GLAD deposition. The polycrystalline structure of PEN nanocolumns, which is important towards obtaining high charge carrier mobility for a low solar cell series resistance, has been demonstrated earlier by Zhang et al.[Zhang, 2007b] As expected, due to the incident angle, there were two polymorph observed on ITO. The diameter of the columns in the samples used for fabricating OPVCs later is predominantly in the range of 120 nm to 180 nm and the column area-density is approximately 3×10^{7} mm^{-2}. The cross-section view (Figs. 4.1.1c-d) reveals that the height of the individual columns is rather uniform, about 210 nm, except for a few higher protrusions. There are always small gaps between the columns, even for locally high area-densities.

The results of PEN column presented above using α of 85°, ω of 6 revolutions per minute (rpm) and a deposition rate of ca. 1 Å/s on bare ITO likewise are depicted in Fig4.1.2b. When the incident angle was changed to 80° while keeping the other parameters constant, the density of the column increased as a result of rather weak shadow effect as illustrated in Fig.4.1.2a. The “column” density fabricated with 80° incident angle is much larger than that

using an 85° incident angle, corresponding to valleys of lower volume, and thus agreeing with the assumption of a relationship between column intensity and incident angle as discussed in section 3.1.2.

In figures 4.1.3(c) and (d), the influence of the substrates with different morphology on column formation is presented. The two substrates were amounted into the chamber at the same time for the PEN deposition to make sure using the same deposition parameters. In contrast to column structure on ITO substrate (Fig.4.1.3c), PEN film on PEDOT：PSS coated ITO substrate exhibits rather different morphology. No prototypical column features can be observed but the features are similar to PEN thin film prepared with vertically deposition on PEDOT:PSS (see Fig.4.1.3b). The absence of column structure on PEDOT:PSS is related to the large diffusion length of PEN molecules on smooth surfaces during vacuum deposition. As can been seen from figures 4.1.3 (a) and (b), in comparison to PEN film vertically deposited on ITO (a) and PEDOT:PSS (b), the average island size on PEDOT:PSS is much larger than that on ITO due to the extended diffusion length on smoother surfaces. There are many studies of PEN molecules growth on silicon oxide surface where the roughness is similar to PEDOT:PSS, approximately rms of 0.2 nm, which demonstrates a PEN molecular diffusion length in the range of micrometers.[Heringdorf, 2001, Abelmann, 1997b, Ruiz, 2003a, Ruiz, 2003b] In GLAD, the extended diffusion length on PEDOT:PSS enlarges the initial island growth size as for vertical deposition leading to a weakening of the shadow effect at the onset of growth core formation. Therefore, there is no PEN columnar structure growing on PEDOT:PSS coated ITO substrate.

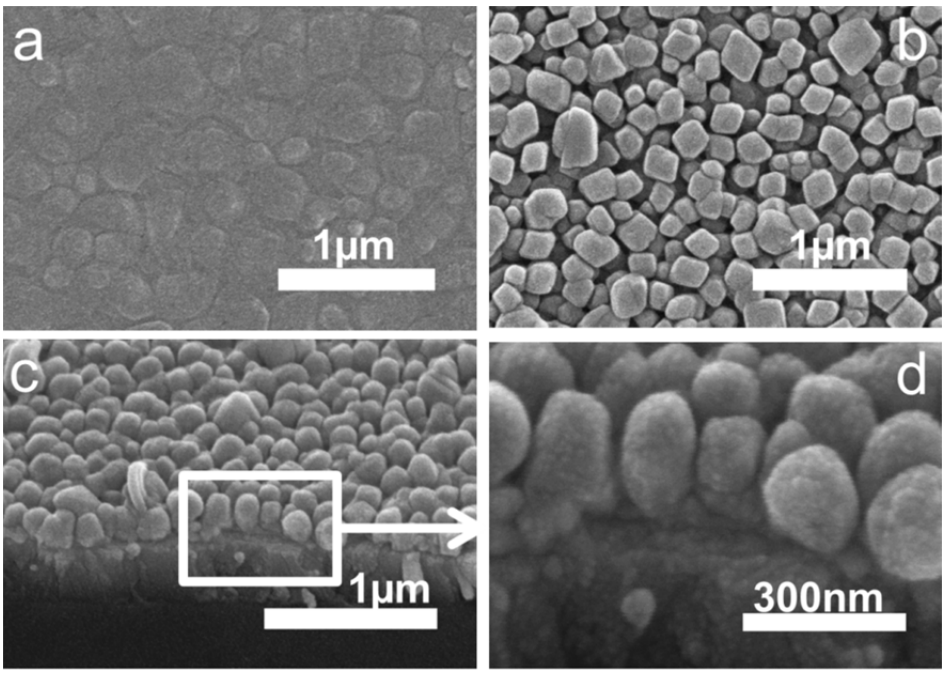

Fig. 4.1.1 SEM micrographs of PEN films on ITO. a) Top view of vertically deposited pentacene. b) Top view of a GLAD pentacene nanocolumn array (NCA). c) and d) Cross-section views of a GLAD pentacene NCA.

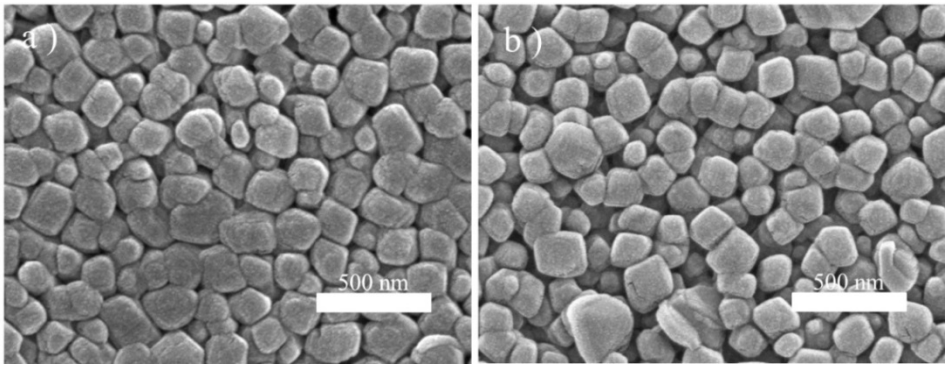

Fig.4.1.2 SEM micrographs of PEN film on ITO. a) Top view of the sample fabricated with incident angle of 80°. b) Top view of the sample fabricated with incident angle of 85°.

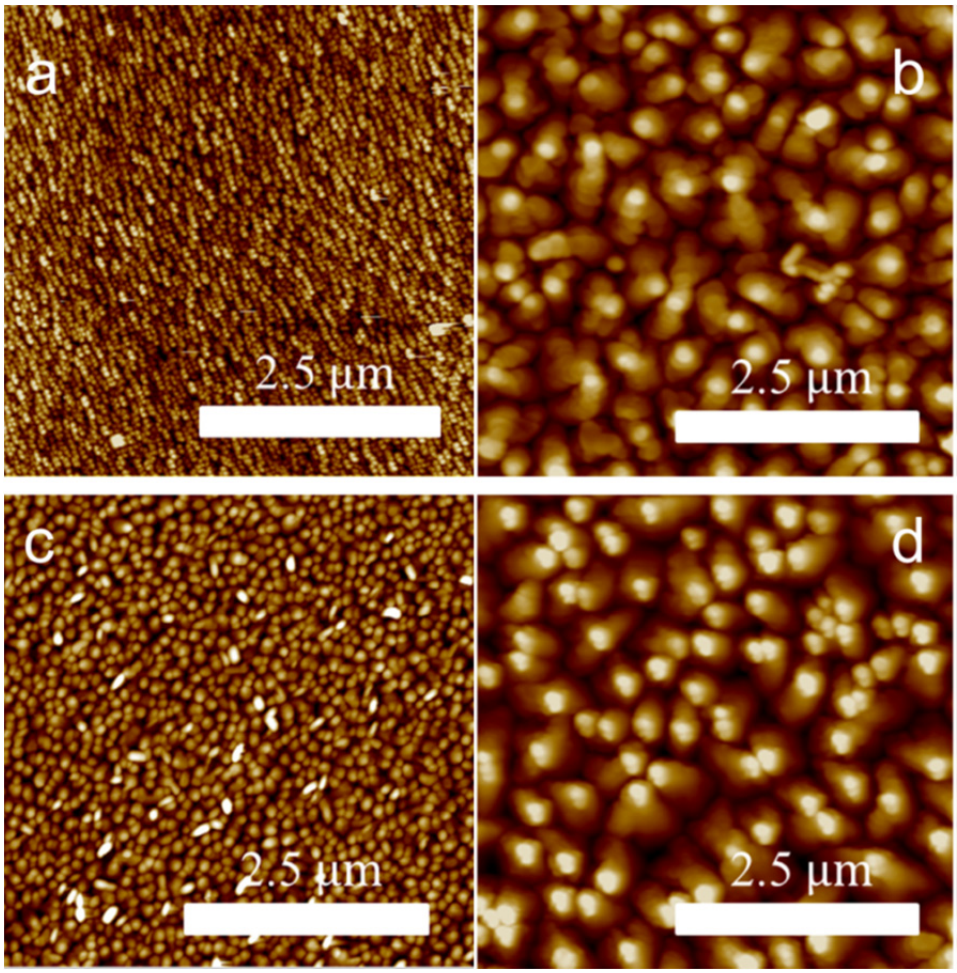

Fig.4.1.3 AFM micrographs of PEN film/columns on ITO and PEDOT:PSS coated ITO. a) Vertically deposited on ITO. b) Vertically deposited on PEDOT:PSS coated ITO. c) GLAD on ITO. d) GLAD on PEDOT:PSS coated ITO. Vertically deposition rate is 0.02 nm/s. GLAD parameters:
rpm and deposition rate: 0.1 nm/s. The height scale for all figures is 100 nm.

4.1.3 Analysis of OPVCs

a. Solution processing for electron acceptor

The interpenetrating donor-acceptor structure was obtained by PCBM solution spin coating onto the PEN nanocolumn arrays. As shown in Fig. 4.1.4a, spin coating with low concentration PCBM solution (18 mg/ml in chlorobenzene) left the underlying PEN nanocolumns still clearly visible. Although such a highly corrugated surface easily leads to electrical shorts,[Seungkeun, 2009, Reddy, 2009, Vogel, 2006b] the observation implies that PEN nanocolumns still stand vertically on the ITO substrate and are not impeded by PCBM spin coating. In addition, PCBM infiltration into gaps between nanocolumns occurred as shown in Fig. 4.1.4b. With a higher concentration PCBM solution (28 mg/ml), a rather smooth surface was obtained and the gaps were filled adequately by PCBM (see Figs. 4.1.4 c-d). Firstly, the OPVCs based on PEN/PCBM interdigitated heterojunction were prepared on bare ITO substrate, transferred to UHV chamber via ambient condition and completed with Sm deposition as the top electrode. However, all devices were "dead", displaying short circuits. This might be induced by the current short-pass formed by infiltrated PCBM contacting both electrodes. Unsurprisingly, the reference devices prepared under the same conditions employing bilayer structure with PEN/PCBM were also "dead" unless PEDOT:PSS was applied before PEN deposition.

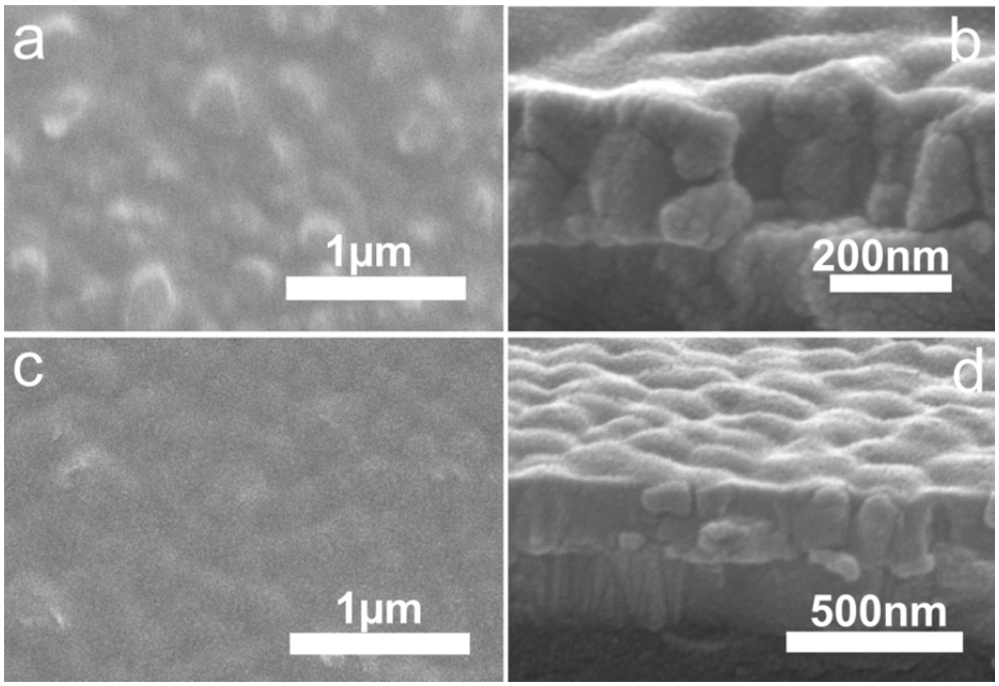

Fig.4.1.4 SEM micrographs of PCBM solution deposited onto pentacene NCAs. a) and b) Top and cross-section views of low concentration(18 mg/ml) PCBM solution. (c) and (d) Top and cross-section views of high concentration(28 mg/ml) PCBM solution.

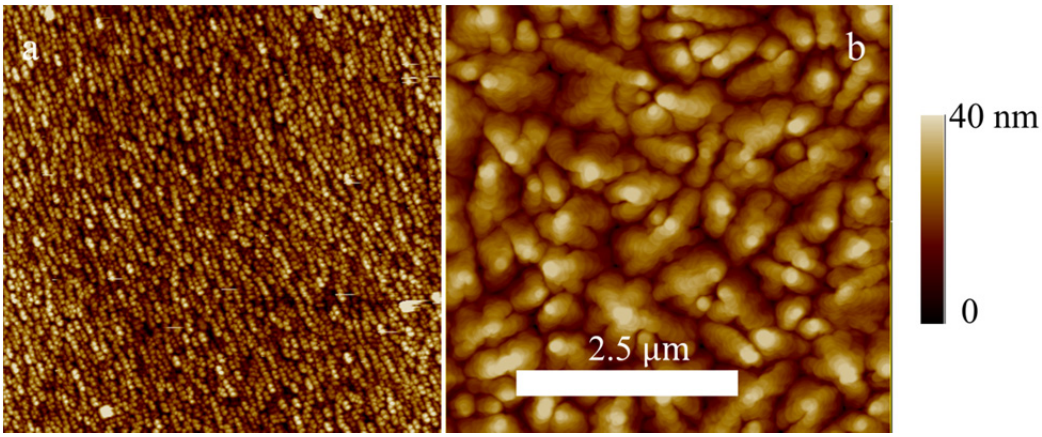

Fig.4.1.5 Morphology of PEN on ITO (a) and PEDOT:PSS (b) investigated by AFM.

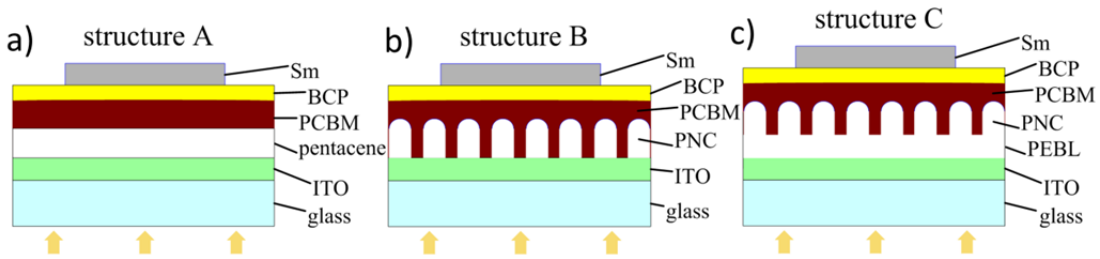

Fig. 4.1.6 Structures of the investigated OPVCs. a) Planar bi-layer structure. b) PNC (pentacene nanocolumn) structure. c) PEBL (pentacene electron-blocking layer) combined with PNC.

Figure 4.1.5 presents the morphology of PEN on ITO and PEDOT:PSS substrate respectively. Obviously, the PEN island size on PEDOT:PSS substrate is much larger than that on ITO, meaning that there are less PEN crystalline boundaries on sample b. This is beneficial for effectively reducing the possibility of having a current short. However, as presented previously, it is impossible to fabricate PEN nanocolumns on PEDOT:PSS substrate. Therefore another electrode interface was considered where BCP was deposited as a blocking layer before evaporating Sm in order to prevent the two electrodes contacting with PCBM directly. As predicted, the development of current short-pass was efficiently prevented by the inserted-BCP between PCBM and Sm. In addition BCP with wide optical energy gap (3.5 eV [Peumans, 2000]) was used as an exciton-blocking layer. Although BCP introduces the problem of crystallization, it remains a good candidate to act as protection-layer for the active the donor/acceptor layer during metal deposition. (In this work, all metal evaporation were finished in 30 minutes after BCP deposition, avoiding the crystalline issue reported [Masumoto, 2008])

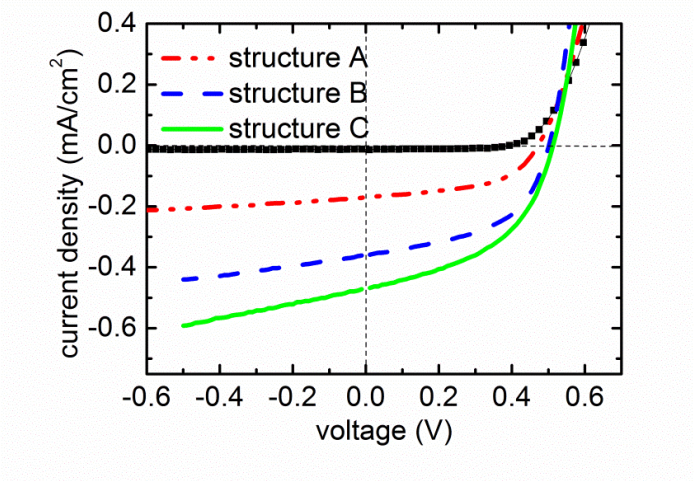

Fig. 4.1.7 Current density-voltage characteristics of NC heterojunction and improved devices compared with bi-layer heterojunction devices at the same illumination density. Squares with the black line show the characteristics of all three devices in dark.

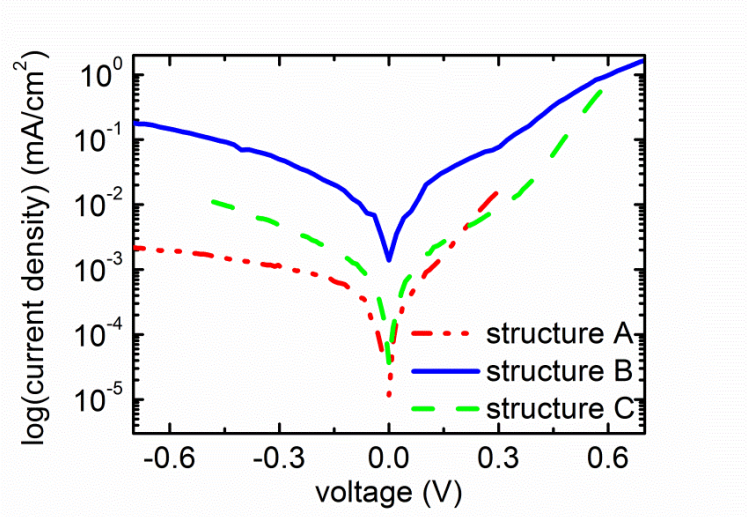

Fig. 4.1.8 Current density-voltage characteristics in dark for the three device structures.

Tab. 4.1 Characteristic performance parameters of OPVCs. Open circuit voltage (V_{oc}), short circuit current (J_{sc}), fill factor (FF).

	Structure A	Structure B	Structure C
V_{oc}(V)	0.50	0.50	0.51
J_{sc} (mA/cm^2)	0.17	0.36	0.47
FF	0.48	0.51	0.48
$V_{oc}J_{sc}$FF	0.04	0.09	0.12

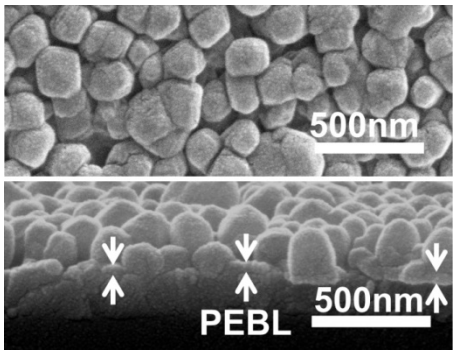

Fig. 4.1.9 Top and cross-section view of pentacene nanocolumn array grown on a 10 nm thick PEBL.

The structure of all investigated OPVC variants are shown in Fig. 4.1.6. For comparison with OPVCs that have PEN nanocolumns, an optimized bi-layer planar heterojunction OPVC employing ITO/PEDOT:PSS/50nm PEN/30nm PCBM/8nm BCP/100nm Sm (structure A) was fabricated at room temperature, as suggested in [Reddy, 2009]. Interdigitated OPVC fabrication was done by BCP and cathode (Sm) deposition in high vacuum (structure B). The current density-voltage characteristics of interdigitated OPVCs and reference bi-layer cells are shown in Fig. 4.1.7 with the characteristic parameters summarized in Tab. 4.1. The open-circuit voltage (V_{oc}) of all cells is virtually the same, i.e., 0.5 V. However, the short circuit current density (J_{sc}) of interdigitated cells with structure B has more than doubled compared to that of the reference bi-layer cell under the same illumination condition. The fill factor (FF) of the cell with structure has slightly increased from 0.48 to 0.51. The improved performance of interdigitated cells is attributed to the increased active interface area due to the PEN nanocolumns. From the SEM images a ca. threefold increased interface area with nanocolumns is estimated, which in principle could lead to threefold increase J_{sc} threefold if there are no other factors impacting device performance. Since J_{sc} in structure B OPVCs was only doubled compared to structure A, we expect additional effects to play a role. Considering the characteristics of devices in the dark, shown on a logarithmic scale in Fig. 4.1.8, a much lower specific shunt resistivity of structure B devices was obtained (approx. 0.02 MΩ cm^2) compared to that of structure A devices (approx. 2.86 MΩ cm^2).[Sze, 2007] The low shunt resistance could be due to current leakage paths produced by the infiltration of the PCBM acceptor phase to the bottom electrode, which does not occur in the planar bi-layer reference device.

To eliminate the problem of leakage paths, a 10nm thick PEN film was deposited on ITO before growing PEN nanocolumns as an electron-blocking layer, shown as structure C in Fig. 4.1.6 (c). As seen from Fig. 4.1.9, there is no marked difference of pentacene nanocolumns compared to those in Fig. 4.1.1 except for the thin PEN electron-blocking layer. A remarkable increase in J_{sc} resulted (see Fig. 4.1.7 and Tab. 1), owing to the increased shunt resistivity (approx. 1 MΩ cm^2), as shown in Fig. 4.1.8. Hence, the influence of current leakage paths is reduced but not entirely eliminated. Employing a heavily p-doped thin film was suggested as

electron-blocking layer that might be helpful to further improve device performance. Nevertheless, the characteristics of interdigitated OPVCs employing PEN nanocolumns were improved significantly by utilizing the thin electron-blocking layer. The J_{sc} improvement now reached more than 90% of the expected threefold increase due to increased active interface area. However power conversion efficiency values under standard illumination conditions (due to the experimental setup in vacuum) cannot be provided. Devices with structure C (interdigitated) are estimated to have an efficiency of ca. 4%, as opposed to only ca. 1.5% for those with structure A (planar), at 2.5 mW/cm2 illumination from a halogen lamp with an emission spectrum close to daylight in the visible region.

b. Vacuum deposition for electron acceptor

On the other hand, attempts were made to build the donor-acceptor heterojunction by depositing C60 (deposition rate: 0.2 nm/s) on top of PEN nanocolumns in vacuum (3.5×10^{-7} mbar). However, due to the narrow "tunnels" (gaps), it was easier for evaporated C60 molecules to be deposited on the wall of the tunnels than passing the tunnel and be deposited on the bottom of the tunnels. Thus, this led to unfilled holes underneath as indicated in Fig.4.1.10a. The unfilled holes are huge defects that significantly reduce the PCE of OPVCs. Afterwards, the vacuum level was reduced to 3.5×10^{-3} mbar by venting the chamber with argon gas in an attempt to shorten the evaporated molecules free pathway to allow the evaporated molecules to move randomly. To some extent, this method was helpful for C60 molecules passing through the "tunnels", but unfilled holes still existed. In any case, devices were fabricated based on the heterojunction of PEN nanocolumns/C60, and the performance was poor as predicted. In particular the J_{sc} was very low as shown in Fig.4.1.10b.[Salzmann, 2008] Thus, vacuum depositing electron acceptor molecules to fabricate interdigitated heterojunction is not suitable for such high intensity columnar structure. Large volume valley is necessary for evaporated molecules passing the "tunnel".

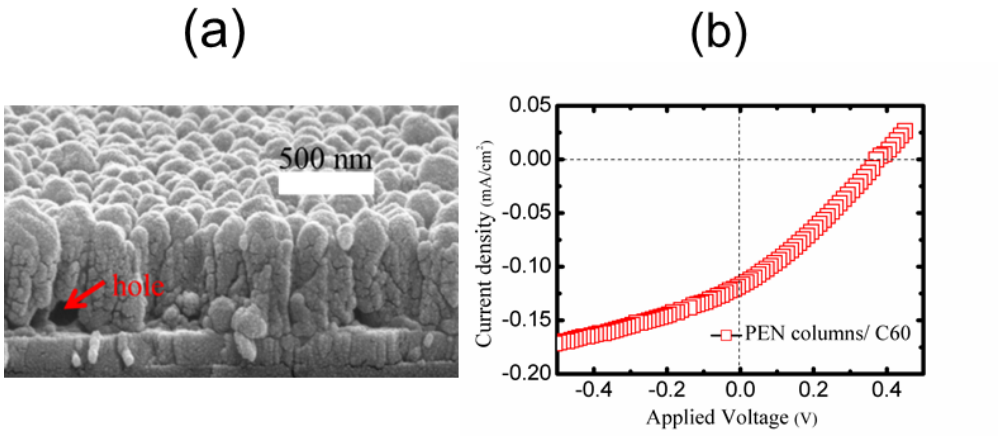

Fig.4.1.10 (a) Evaporation of C60 on top of PEN columns in vacuum. (b) Performance of OPCVs under illumination 2.5 mW/cm2 in vacuum, device structure ITO/PEN column/C60/BCP/Sm.

4.1.4 Summary

In conclusion, the morphology of pentacene nanocolumns grown by GLAD has been investigated with SEM and AFM, through variation of the experimental conditions. Final vertically aligned crystalline pentacene nanocolumns with a diameter of ~ 160 nm were achieved. Qualitative analysis of the influence of substrate morphology and incident angle on PEN nanocolumn architecture has been presented. Interdigitated OPVCs structures were achieved by spin-coating PCBM onto the optimized pentacene nanocolumns, which led to a threefold increase of active donor/acceptor interface area as compared to planar bi-layer structures. By employing an additional planar thin pentacene electron-blocking layer, J_{sc} was increased from 0.17 mA cm^{-2} to 0.47 mA cm^{-2}, thus attributing over 90% of the expected increase to the larger interface area. The remarkable conversion efficiency of OPVCs based on NC structures proves that it is an effective architecture towards eliminating charge transport and exciton diffusion bottlenecks while maximizing the interface area. Other materials as donors and/or acceptors employed in similar structures will most likely lead to significant further improvements in OPVCs performance in the future. In addition, attempts to fabricate the OPVCs with vacuum deposition of electron acceptor C60 were made. Unfortunately, the performance of OPVCs was not satisfactory due to the large amount of defects induced by appearance of unfilled hole after vacuum deposition.

4.1.5 Experimental details

ITO coated glass substrates (Präzisions Glas & Optik, sheet resistance < 20 Ω/sq, surface roughness (rms): 2 nm) were sonicated for 10 min in acetone and, subsequently, isopropanol. After cleanness, ITO coated substrates were patterned by etching processing (36.5% HCl solution), leaving two parallel strips ITO (1 mm width) on glass, and the pattern ITO substrates were cleaned once more as description before.

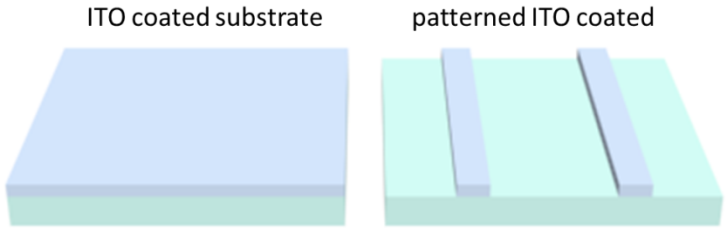

Fig.4.1.11 The bottom cyan box is denoted as glass substrate ;the light blue squares are denoted as ITO.

UV-ozone-treatment was applied to improve the wetting of the substrate by an aqueous suspension of the intrinsically conducting polymer poly(ethylene-dioxythiophene): poly--(styrenesulfonate) (PEDOT:PSS) (H.C. Starck GmbH, CH8000), employed as substrate for OPVCs. PEDOT:PSS was spin-coated and subsequently annealed at 200℃ for 5 min under

ambient conditions to desorb residual water. PEN was deposited by GLAD on glass substrates coated with 20Ω/square ITO (patterned) in a high vacuum chamber (base pressure ~3×10^{-7} mbar). A computer-controlled stepper motor was used to facilitate sample rotation about the substrate surface normal. The molecular flux incidence angle α and the substrate rotation rate ω were set between 60° to 85° and 3 or 6 rounds per minute, respectively during nanocolumn growth for device fabrication. The distance between the center of the substrate and the evaporation source was 15 cm, and the deposition rate at the substrate was ca. 1 Å/s, as monitored by a quartz-crystal microbalance which vertically faced the evaporation source. The nominal thickness recorded by microbalance was corrected according the profiles of AFM and SEM investigation.

OPVCs were fabricated by spin-coating PCBM dissolved in chlorobenzene (28 mg/ml) onto the NCAs at 25 rounds per second in a nitrogen glove box. The pentacene/PCBM interdigitated structures were subsequently annealed at 85℃ for 20 min to remove residual solvent and to facilitate improved PCBM infiltration into the voids between the PEN nanocolumns. An 8 nm thick exciton-blocking layer of BCP was deposited onto the structure before a 100 nm thick Sm cathode was evaporated in high vacuum (base pressure ~8×10^{-8} mbar). The Sm evaporation was carried with a mask as shown in Fig.4.1.12 and the exact size of devices was determined by the crossing area of the bottom ITO substrate and the top Sm, in most cases it was 1 mm^2. The current density-voltage characteristics in dark and under illumination (2.5 mW/cm^2, Solux C6 halogen lamp) were measured in vacuum (2×10^{-8} mbar) with a Keithley 2400 SourceMeter® as shown in Figure 4.1.13, and the sample morphology was investigated with a HITACHI S-4100 field-emission SEM, after sputter-coating the samples with a thin conductive Au layer.

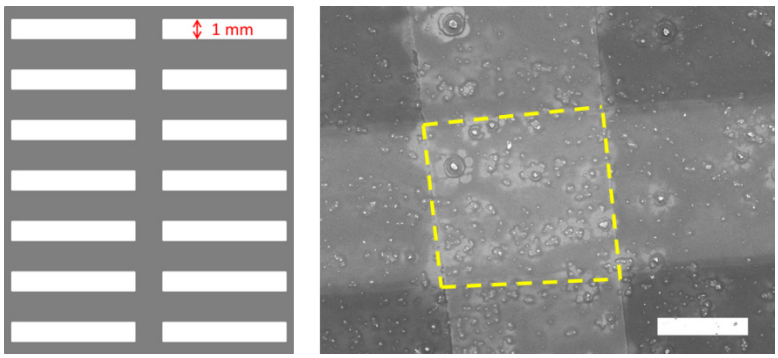

Fig.4.1.12 Left is the shape of mask used for top Sm evaporation; the white zones on the mask are empty where Sm atoms can penetrate through and reach to the top of samples. Right image is topography of one device investigated by SEM; the yellow-dash-line square denotes the crossing area of bottom ITO and perpendicular top Sm, the size of an active OPVC.

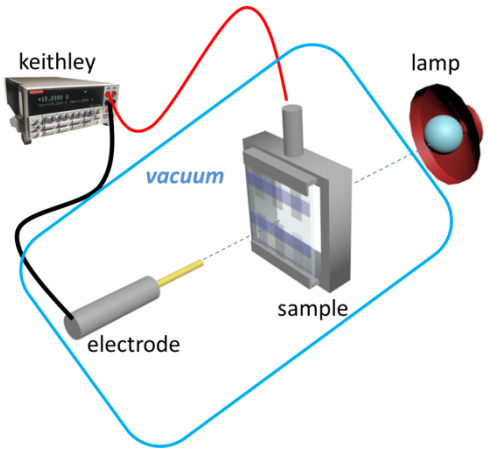

Fig.4.1.13 J-V measurement system. Inner of blue frame denotes in vacuum. The sample facing front is put on a frame holder which also contacts with sample's bottom electrode. The front electrode rod approaches to the sample as the top contact. Keithley is used to control applied bias to devices. Samples are illuminated by the lamp through chamber's window.

4.2 DIP nanocolumn and application in OPVCs

4.2.1 Introduction

Since the initial application of "sandwich" structure in organic photovoltaic cells (OPVCs) in the 1970s', [Tang, 1975, Ghosh, 1973] the power conversion efficiency of OPVCs significantly increased only after introducing the donor/acceptor heterojunction concept,[Tang, 1986] where layers of preferentially hole/electron conducting materials with an interface promoting exciton dissociation are employed. Today, high open circuit voltage (V_{oc}) and optimized light harvesting can be realized with a wide variety of organic semiconductors suitable for application in OPVCs.[Svensson, 2003, Kietzke, 2006, Zhang, 2006, Bailey-Salzman, 2007, Riede, 2008, Bijleveld, 2010, Wagner, 2012, Dou, 2013, Hörmann, 2011b, Wagner, 2010] However, the short diffusion length of photo-generated excitons in such materials (typically in the range of tens of nanometers[Stübinger, 2001, Kurrle, 2008]) significantly limits the fraction of excitons dissociated at the donor/acceptor interface, thus restricting the generation of mobile charges. To reconcile the exciton diffusion length with the average dimensions of organic heterojunctions, the concept of bulk heterojunction was introduced, which allows increasing the effective area of the donor/acceptor interface and, simultaneously, reducing the separation between individual donor and acceptor volumes.[Yu, 1995, Halls, 1995, Peumans, 2003a] While this approach turned out to be highly successful for polymer-based OPVCs processed from solution [Ma, 2005] and molecular blend structure OPVCs typically from vacuum co-deposition[Wagner, 2012, Gruber, 2013, Xiao, 2013], low charge-carrier mobility, exciton quenching, and morphological issues like dead-ends in the conduction pathway (*i.e.*, individual, isolated phase grains without connection to the respective electrode) still limit the desired efficiency improvement of this approach [Salzmann, 2008, Opitz, 2010a, Gruber, 2012]. Idealized structures to overcome these limitations are bulk heterojunction OPVCs comprising a crystalline, vertically interdigitated, and laterally structured configuration of separate donor/acceptor phases, with the aim to enable generated excitons to most likely reach an interface and the separated charges to be efficiently collected by the electrodes through individual donor/acceptor zones.[Yang, 2004, Koch, 2007a] As demonstrated in previous studies, a preparation technique highly promising for realizing such structures is glancing angle deposition (GLAD), [Robbie, 1996, Robbie, 1997, Van Dijken, Zhou] as schematically illustrated in Fig. 4.2.1, where high aspect-ratio nanocolumns (NCs) are established through shadowing effects.[Zheng, 2009b, Yang, 2004, Yu, 2011, Koch, 2007a]

Here, OPVCs based on a conventional bilayer heterojunction of a donor/acceptor pair are compared to devices with interdigitated heterojunctions comprising NC arrays. Diindenoperylene (DIP) was chosen as the donor material to establish NC arrays via GLAD as it is an emerging material for OPVCs [Wagner, 2010]. To accomplish the interdigitated donor/acceptor heterojunction, fullerene (C60) was employed as the acceptor material by

subsequent (vertical) physical vapor deposition in order to fill the voids between the NCs, as schematically illustrated in Fig. 4.2.10 (columnar). The performance of NC-based devices is shown to be significantly improved in comparison to the bilayer reference OPVCs, which can be related to the increase in active interface area and enhanced absorption of the NC arrays, as well as reducing the influence of the "trade-off" between getting high light absorption with thick C60 film and obtaining good exciton dissociation efficiency, which requires a film thickness close to excitons diffusion length.

4.2.2 DIP nanocolumn

a. Morphology

The formation of individual NCs upon GLAD is due to limited adsorbate diffusion, shadowing effects of the collimated molecular flux under oblique angle ($\alpha > 70°$), and continuous rotation of the substrate (*c.f.* Fig. 4.2.1), which leads to a large fraction of the incoming flux being captured by larger grains that, therefore, preferentially grow.[Robbie, 1997, Yu, 2011, Zhang, 2007a, Abelmann, 1997a, Zhao, 2002] Fig. 4.2.2 illustrates the representative topography and cross section of conventional vertically deposited DIP films and GLAD deposited DIP nanocolumn on bare ITO. The vertically deposited film on bare ITO (Fig. 2.2a-b) shows a morphology of (terraced) islands as expected for DIP.[Turak, 2011, Dürr, 2002] In contrast, with GLAD a highly corrugated morphology of polygon-shaped nanocolumns reaching down to the ITO substrate is apparent (Fig. 4.2.2c-d). As a result, the surface roughness (root-mean-square-rms: 9.2 nm) increases by more than a factor of two (rms: 22.4 nm) through GLAD, and the bottom radius of the NCs is in the range 60 and 80 nm (*c.f.* Fig. 4.2.2a-b). This is well within the range of the reported exciton diffusion length of crystalline DIP between 20 and 100 nm [Kurrle, 2008, Lunt]. To enhance the shadow effect, a 10 nm thick DIP film was vertically deposited on the substrates prior to GLAD to increase the substrate roughness as shown in Fig.4.2.3. Besides increasing the surface roughness, the underneath DIP thin film also acts as an electron blocking layer, in analogy to a procedure introduced in a previous study on pentacene NCs[Yu, 2011]. After obtaining such DIP nanocolumn structures, attempts were made to fabricate OPVCs, employing C60 and PCBM as electron acceptor. However, all devices showed short circuit without diode properties. Even for bilayer heterojunction with 50 nm DIP film and 50 nm C60 film, diode properties could only be observed when using PEDOT:PSS as the hole transport layer. Therefore, the possibility of growing DIP columns on PEDOT:PSS was explored.

Figures 4.2.4 (a-b) shows the morphology of DIP nanocolumns grown by GLAD on PEDOT:PSS coated ITO substrate. Unlike DIP-NCs on bare ITO, DIP-NCs on the PEDOT:PSS exhibited some connectivity and had a broader distribution of diameters, which is a direct result of the increased molecular diffusibility on the smoother surface. (PEN columnar structure could not be obtained on polymer coated ITO substrates. For further details see section 4.1) As previously, a 10 nm thick DIP film was vertically deposited on the

substrates prior to GLAD to increase the substrate roughness. With this approach, the homogeneity of the NCs on the bare ITO substrate was significantly improved (Fig. 4.2.4c) and essentially monodisperse columns were formed with mean lateral and vertical extensions of 65 nm (radius) and 120 nm respectively. For the PEDOT:PSS covered ITO substrates, the same trend was essentially observed with the void area between the NCs approximately doubling in size (Fig. 4.2.4d). In Fig.4.2.5, PEDOT:PSS layer can be observed since the sample was not covered by gold, which is commonly sputtered onto the organic film prior to SEM measurement to avoid charging and increase resolution.

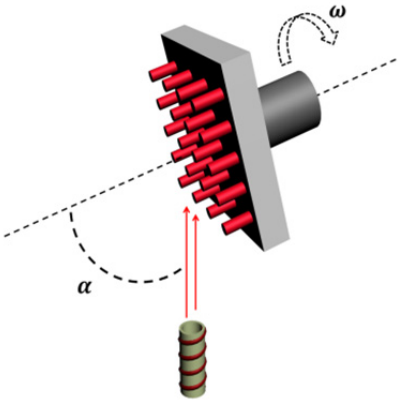

Fig.4.2.1 Experimental geometry of GLAD; α is the angle of the molecular flux with respect to the sample normal and ω the substrate rotation frequency measured in rpm.

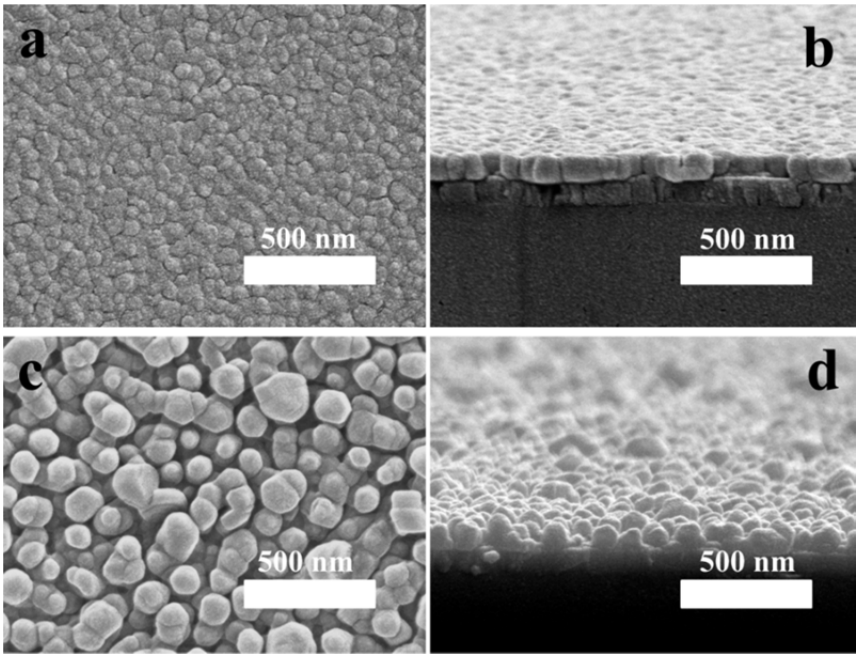

Fig. 4.2.2 SEM micrographs (top and cross-section view) of DIP thin film and nanocolumns on bare ITO substrates.

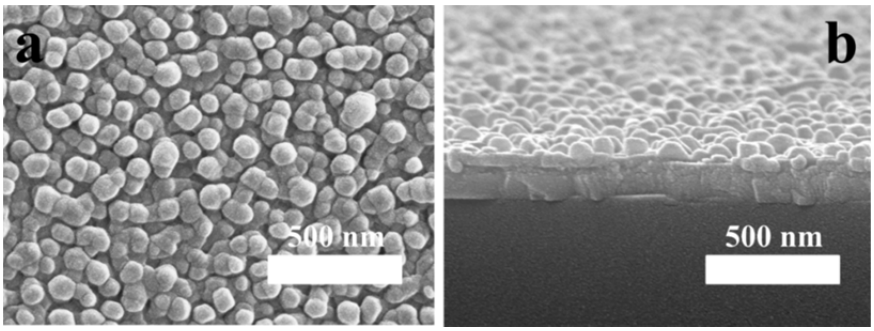

Fig.4.2.3. SEM micrographs (top and cross-section view) of 100 nm DIP nanocolumns on 10 nm thick DIP film coated ITO.

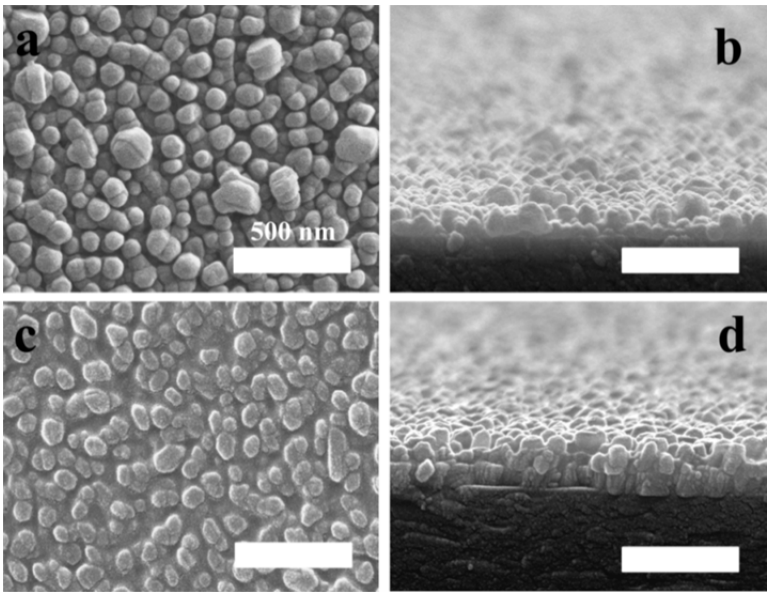

Fig. 4.2.4. SEM micrographs (top and cross-section view) of DIP thin film and nanocolumns. (a-b) 100nm DIP nanocolumns on PEDOT:PSS; (c-d)100nm DIP nanocolumns on 10 nm thick DIP film coated PEDOT:PSS.

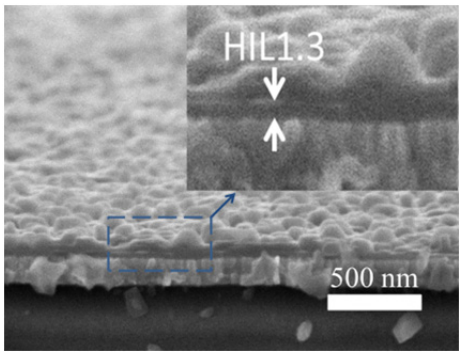

Fig.4.2.5 SEM micrographs (cross-section) of DIP nanocolumns on PEDOT:PSS (HIL1.3) without Au coating.

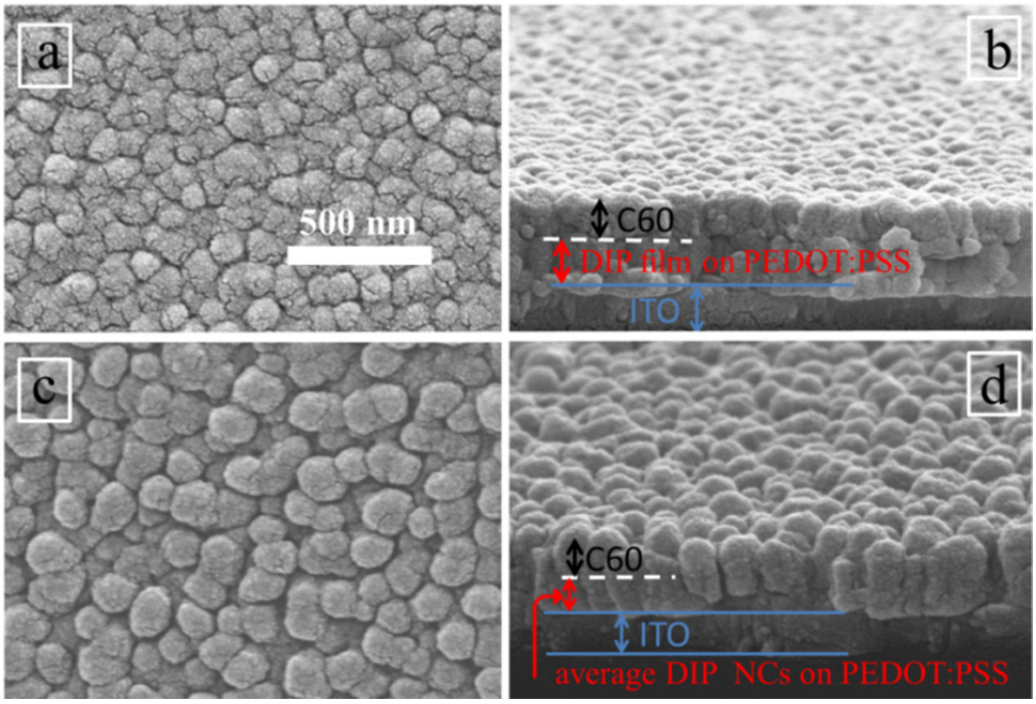

Fig.4.2.6 SEM micrographs of the planar C60/DIP heterojunction (a-b), and the C60/DIP-NC heterojunction (c-d), in top view (left) and cross section view (right); average DIP NC height was determined from a sample not coated with C60, but otherwise prepared identically.

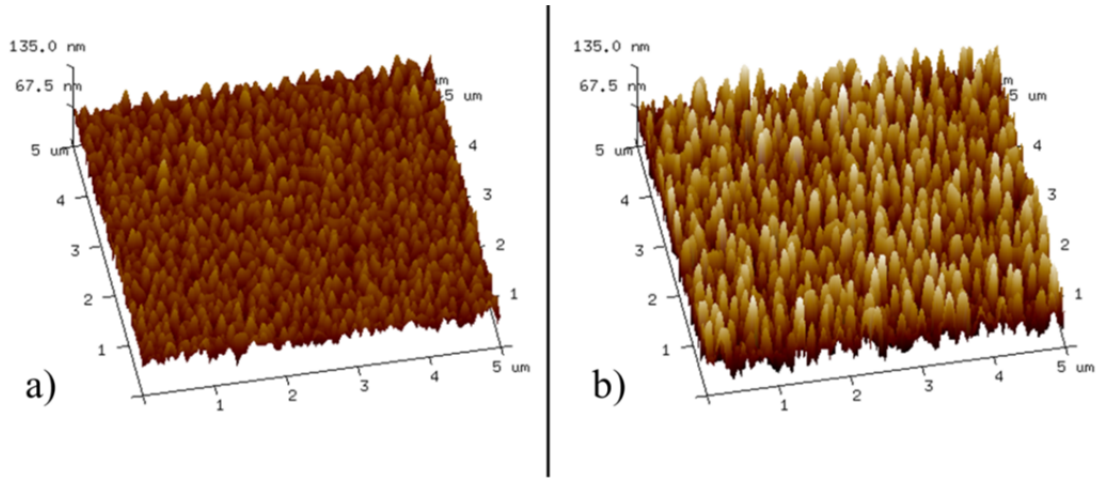

Fig.4.2.7 AFM micrographs of (a) a vertically deposited DIP/PEDOT:PSS film and (b) DIP-NCs/PEDOT:PSS (SEM *c.f.* Fig. 4.2.4d).

Finally, the donor/acceptor heterostructures were completed by vertical vacuum deposition of nominally 75 nm C60 on both the vertically deposited DIP film (denoted as *planar* in the following) and the DIP-NC/DIP (*columnar* in the following) (see Fig. 4.2.4c-d). The topography and the respective cross section micrographs (obtained by SEM) are shown in

Fig. 4.2.6a-d. The comparison with the DIP-only samples reveals that fullerene molecules completely cover the vertically deposited DIP layer (Fig. 4.2.6a-b) and also fully penetrate into the voids between the NCs (Fig. 4.2.6c-d). For the NCs, this is clearly seen in Fig. 4.2.6d from the absence of a clear-cut DIP/C60 interface, which is, in contrast, clearly observed in the cross section view of the bilayer structure (Fig. 4.2.6b). Finally, the AFM micrographs shown in Fig. 4.2.7 were used to determine the surface-area enlargement factor (ξ) of the films, which increases from $\xi = 1.068$ for planar film to $\xi = 1.288$ for NC structures made by GLAD. It should be noted that this value represents a lower limit for ξ due to the finite curvature of the AFM tip.

b. Structure

To assess the microstructure of the samples, grazing-incidence X-ray diffraction (GIXRD) and specular X-ray diffraction (XRD) are performed Fig.4.2.8a shows GIXRD in-plane data of C60 on vertically deposited DIP (black curve) compared to C60 on DIP-NCs (red curve) and two reference scans on DIP-NCs (blue curve) and pristine C60 (black curve), all deposited on ITO (*c.f.* Fig. 4.2.2 for respective SEM data). In all cases, DIP is found to grow crystalline in two different polymorphs with the dominant one denoted as *B* ("bulk phase") and the minor one as *B*' in the following. In the corresponding specular XRD scans (Fig.4.2.9) only one peak series is observed with a (001)-lattice spacing of 1.665 nm, which is indicative of an almost upright-standing molecular orientation. Via the corresponding reciprocal space maps (Fig.4.2.9), both observed polymorphs B and B' are shown to be significantly different from known crystal structures, that is single-crystal and thin-film phases [Heinrich, 2007, Lunt, 2009, Dürr, 2002, Kowarik, 2009, Dürr, 2003]. An unambiguous determination of the unit-cell parameters is impossible in the present case as the diffraction intensities are smeared out along rings in the reciprocal space maps. However, combining the GIXRD and specular XRD results, in analogy with known DIP crystal structures [Heinrich, 2007, Turak, 2011], a monoclinic space-group with a monoclinic angle of $\beta = 92.4°$ is assumed. While the in-plane reflections in the $q_{\|}$-range between 1-2 $Å^{-1}$ due to DIP molecules in upright orientation are present in all DIP samples, both samples comprising DIP-NCs show increased (001)- reflection also in GIXRD. This observation is indicative of additional crystalline grains in a "lying" molecular orientation. Therefore, the vertically deposited film can be regarded as fiber-textured ("2D-powder") in that DIP-NCs show a more "3D-powder like" crystalline property. This can be best observed in the full reciprocal space maps (Fig.4.2.9) where the DIP related peaks of the NC samples are smeared out significantly more than those of the vertically deposited film. In contrast to DIP on the smooth substrates like SiO_x,[Kowarik, 2006] such rings are also observed for vertically deposited DIP on ITO, which is attributed to the higher surface roughness of this substrate that increases the mosaicity of the adsorbate.

1. GIXRD, XRD measurements and data analysis were led by Dr. Ingo Salzmann.

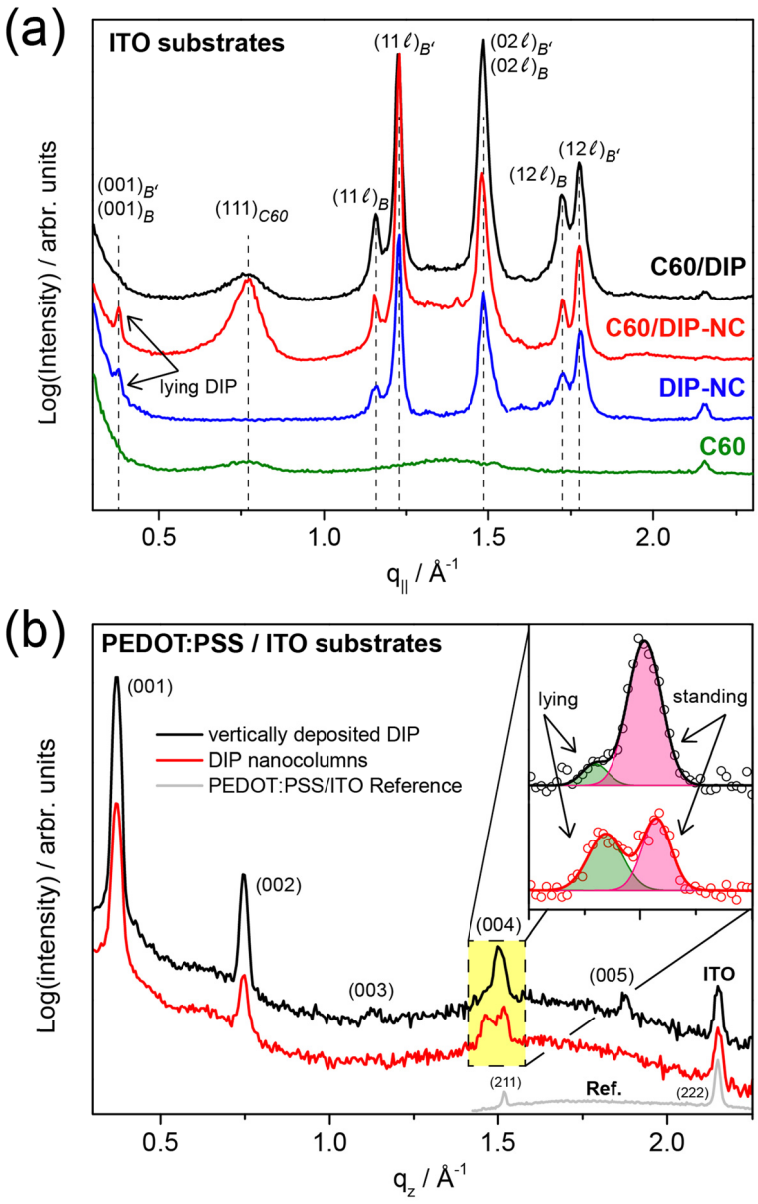

Fig 4.2.8 (a) In-plane GIXRD data of nominally 60 nm C60 on 90 nm vertically deposited DIP (black curve) and on 100 nm C60 on 160 nm DIP-NCs (red curve), as well as for reference samples of 160 nm DIP NCs (blue curve) and 20 nm C60 (green curve). The data was extracted from the respective reciprocal space maps (Fig. 4.2.9) by integrating along qz (range: 0.0 – 0.1 Å-1). All films were deposited on bare ITO substrates. Index labels *B* and *B*' indicate the two different observed crystalline phases of DIP (see text). (b) Specular XRD of nominally 50 nm vertically deposited DIP (black curve), and on 100 nm DIP-NCs on a 10 nm DIP underlayer (red curve), both on PEDOT:PSS coated ITO substrates with a PEDOT:PSS/ITO reference sample (grey curve) with the ITO (222) and (211) peaks observed. The inset is a zoom of the (004) reflection highlighting the contribution of lying DIP molecules ("λ-phase") [Kowarik, 2006], which is enhanced in the DIP-NC sample.

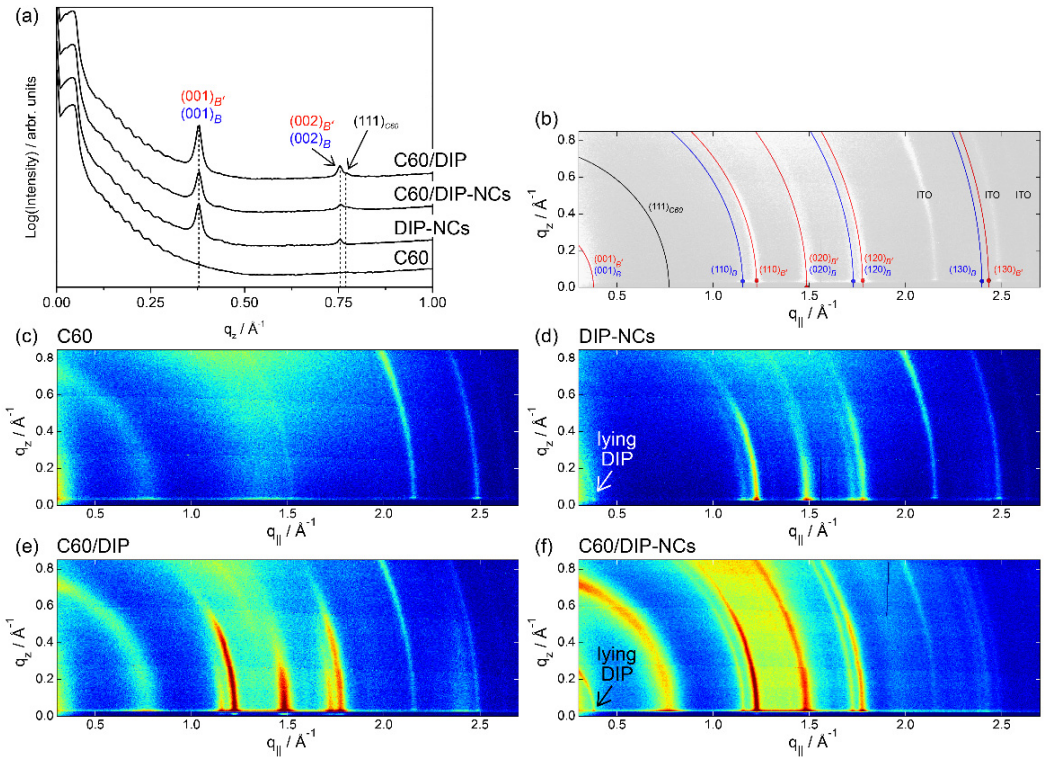

Fig.4.2.9 Specular X-ray diffraction (XRD) and grazing-incidence X-ray diffraction (GIXRD) data of the investigated DIP films on *bare* ITO substrates: (a) XRD data of 60 nm C60 on 90 nm *vertically* deposited DIP [GIXRD: (e)], 100 nm C60 on nominally 160 nm thick DIP *nanocolumns* (DIP-NCs) established by glancing-angle deposition (GLAD) [GIXRD: (f)], as well as pure reference films of 160 nm DIP-NCs [GIXRD: (d)] and 20 nm C60; peaks labelled with *B* and *B*' relate to the polymorphs discussed in the text. (b) Indexation of the reflections observed in GIXRD (c-f) from the $q_{||}$ positions, the unit-cell parameters of the DIP polymorphs can be estimated.

Finally, the C60 top-layer is found to grow crystalline on both types of DIP underlayers, in line with previous findings for C60/DIP/SiO_x or C60/PEN.[Hinderhofer, 2012a, Salzmann, 2008]

Both for vertically deposited DIP and the DIP-NCs, a similar growth behavior is found on PEDOT:PSS coated ITO substrates, as demonstrated by the XRD data depicted in Figure 4.2.8b. Once again, the DIP (00l)-series with an identical lattice spacing of 1.66 nm is recovered, but in contrast to bare ITO substrates, now up to higher order owing to the lower surface roughness of the polymer coating. At 1.47 Å-1 an additional reflection is observed related to lying DIP, which was denoted as λ-phase in previous studies [Kowarik, 2006]. Compared to the vertically deposited DIP film with a peak ratio of 9:1 (area) between the (004) and the λ-phase peak, this ratio changes to almost 1:1 for DIP NCs (see inset in Fig.

4.2.8b), thus, clearly indicating as seen in the above data on the pristine ITO substrates - an increase of the lying DIP fraction in the samples grown by GLAD.

4.2.3 Analysis of OPVCs

a. DIP column/C60

These structures are now used in OPVCs in order to assess the impact of NCs on device performance. Unlike PEN nanocolumn structure, the valley volume of DIP column on ITO substrate is larger and thus very difficult to build working OPVCs (all devices showed short circuit) based on bare DIP column on ITO, even with BCP blocking layer. Therefore, in the following all nanocolumn structures used to fabricate OPVCs were built on PEDOT:PSS coated ITO substrate. OPVCs of planar and NC form, both capped with a 6.5 nm BCP layer followed by a 100 nm Sm top-electrode are compared in Fig.4.2.10. The beneficial role of BCP in such device structures has been extensively investigated and attributed to the protection of the active layer during metal deposition.[Gommans, 2008, Vogel, 2006a] The J-V characteristics of both devices were recorded under 25 mW/cm^2 illumination from a halogen lamp in a vacuum. The results are shown in Fig. 4.2.11a with the corresponding key parameters summarized in Table 4.2. While the open circuit voltages (V_{oc}) of both OPVCs are almost identical (ca. 0.8 V), the short circuit current (J_{sc}) under illumination is almost 20% higher in the NC-based OPVCs. Furthermore, the decrease in the current density is less pronounced in the fourth quadrant for the NC devices. This is related to the series resistance (R_s) which is lower by more than one order of magnitude and further explains the higher fill factor (FF).[Sze, 1981] The much smaller R_s is associated for the NC-based OPVCs to closed pathways within the active donor/acceptor layer. Moreover, the higher FF is further related to the lower ideality factor (n) of the NC-OPVCs (n = 1.1) as compared to that of the bilayer OPVCs (n = 6.4). These values were deduced from the slope of the logarithmically represented J-V characteristics in the exponential regime (in Fig. 4.2.11b) based on the non-ideality diode equation:[Sze, 1981]

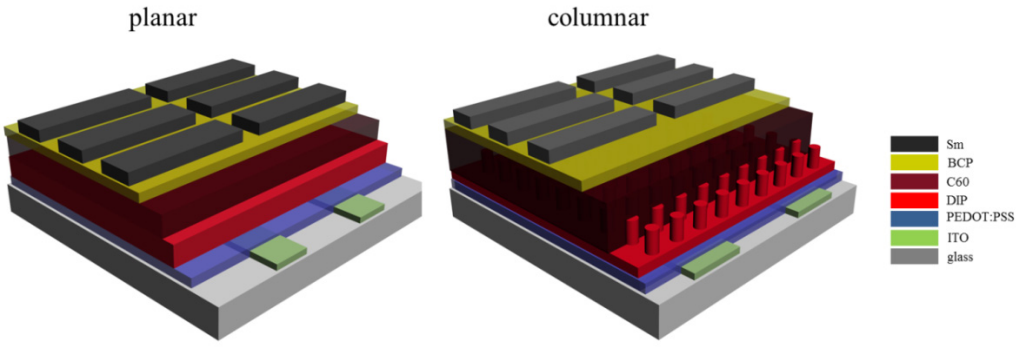

Fig.4.2.10 Scheme of the OPVC structures used; left: conventional bilayer OPVC, right: OPVC with DIP-NCs.

(4.1)

where is the saturation current density, n the diode ideality factor, k Boltzmann's constant and T the temperature.

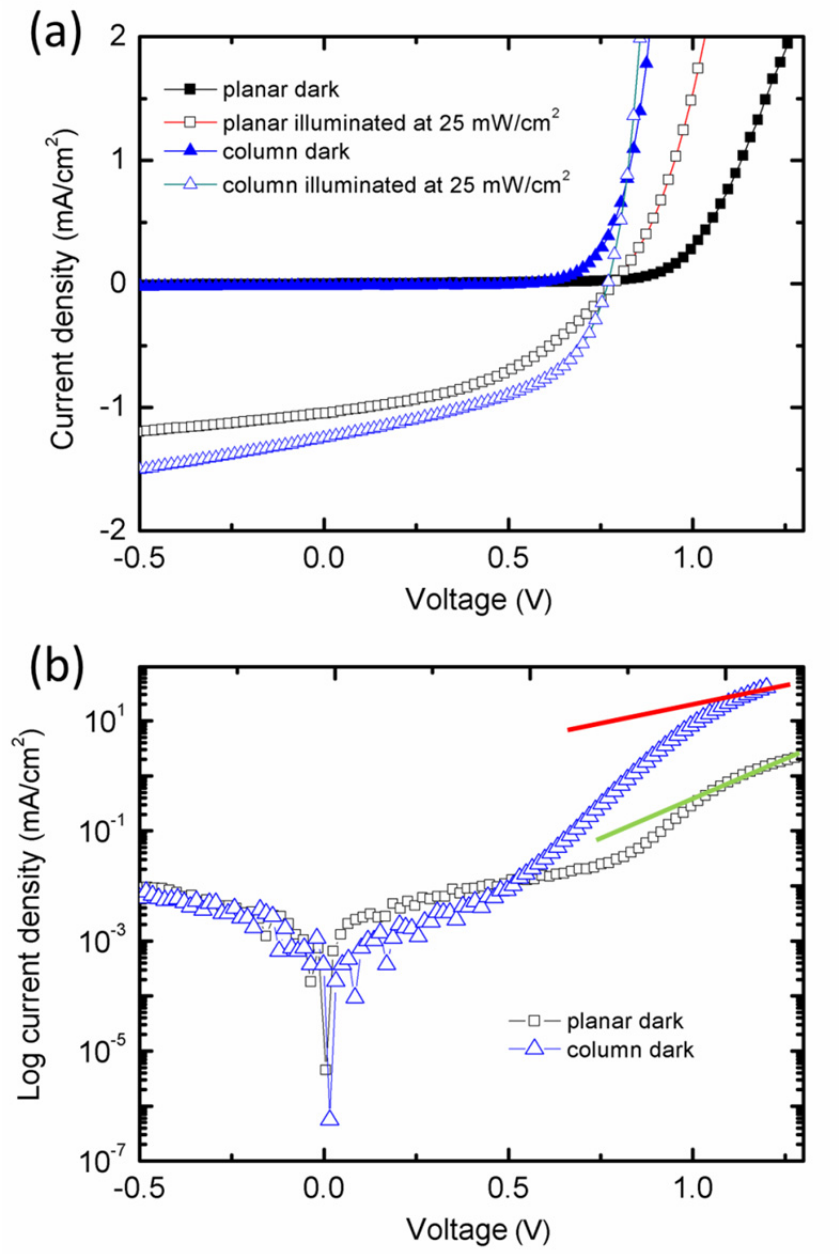

Fig.4.2.11 (a) J-V characteristics of bilayer and DIP-NC based OPVCs. Black closed/open square symbols: bilayer device in dark/illuminated (25 mW/cm^2) in vacuum and blue closed/open triangle symbols: DIP-NC based device in dark/illuminated (25 mW/cm^2) in vacuum. (b) J-V curves in dark in logarithmic representation. The red line and green line are the slopes of current in exponential region.

To assess the influence of air exposure, e.g., due to sample transfer through air or poor encapsulation, reference OPVCs were fabricated and characterized *in-situ* under conditions of simulated AM 1.5 illumination at 100 mW/cm^2 (Fig. 4.2.12).[2] Compared with the performance of the air-exposed OPVCs, almost identical J-V characteristics are observed, which well documents the stability of the DIP-NCs against (short) ambient exposure.

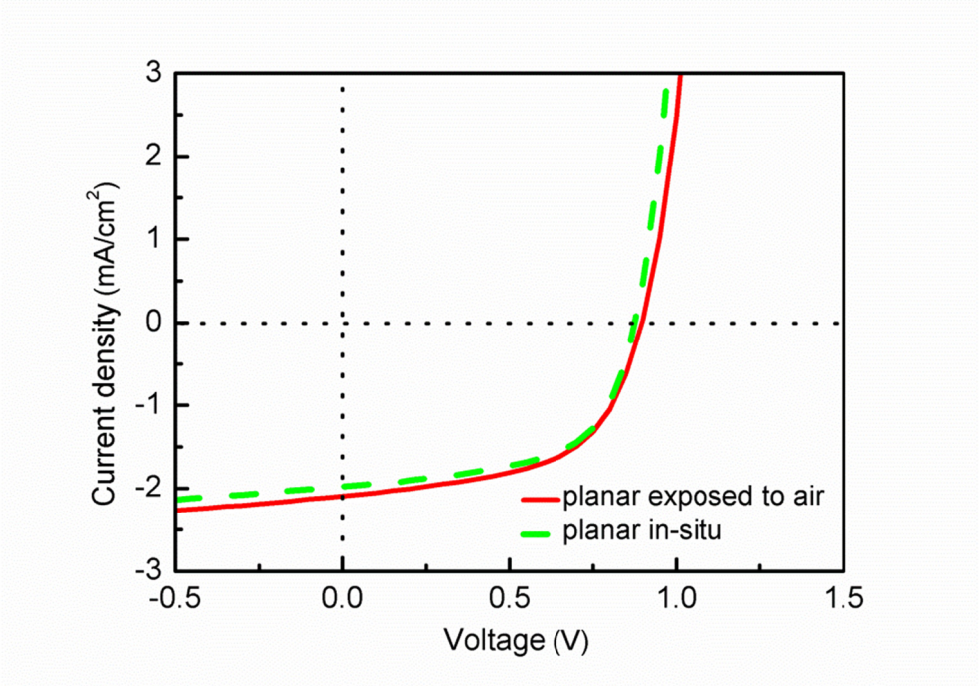

Fig.4.2.12 Comparison of OPVC characteristics of bilayer devices measured *in-situ* and after exposure to ambient air demonstrating negligible degradation under 100 mW/cm^2 illumination.

Table 4.2: Key parameters of OPVC performance, as deduced from the J-V curves (*c.f.* Fig 4.2.11); *planar* denotes the bilayer OPVC, *column* the DIP-NC based device; V_{OC} the open-circuit voltage, J_{SC} the short-circuit current, *FF* the fill factor, R_S the serial resistance, R_{sh} the shunt resistance, and η the external power-conversion efficiency under 25 mW/cm^2 illumination (halogen lamp) in vacuum.

	V_{oc} （V）	J_{sc} (mA/cm^2)	FF	R_s(Ω)	R_{sh}(MΩ)	η
planar	0.79	1.05	0.43	6100	0.34	1.4%±0.05%
column	0.77	1.25	0.48	260	0.17	1.8%±0.05%

2. The DIP nanocolumns structures were fabricated with GLAD at Humboldt Universität zu Berlin, and transferred to Universität Augsburg for C60, BCP and top electrode evaporation. The J-V performance of OPVCs was measured in glovebox (N_2 filled) conditions of simulated AM 1.5 illumination at 100 mW/cm^2.

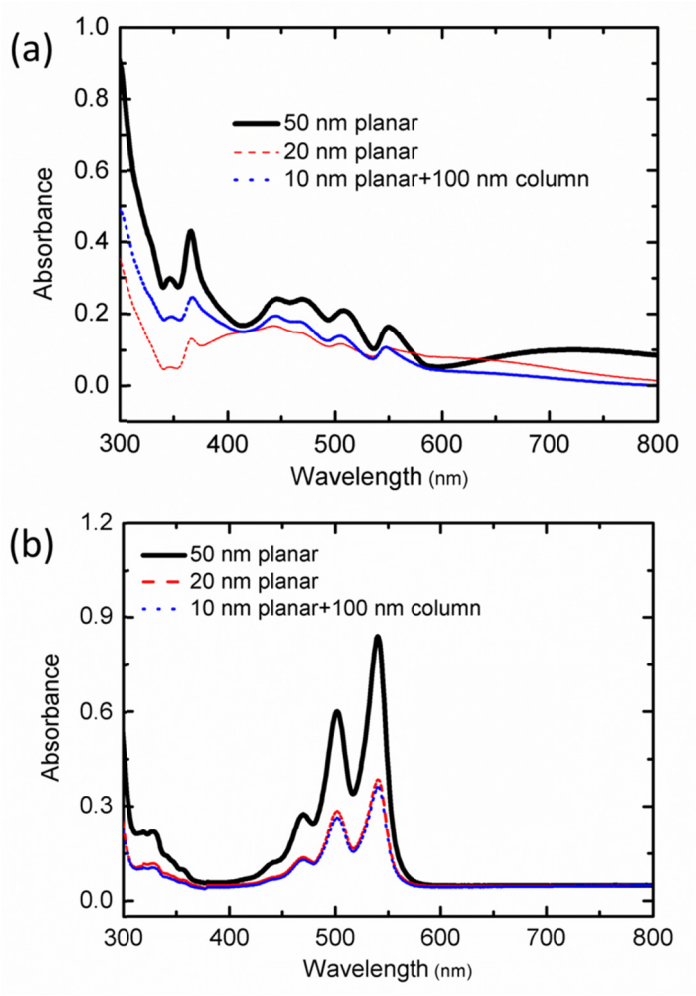

Fig.4.2.13 (a) UV-VIS absorption spectra of 50 nm (black curve) and 20 nm (red point curve) vertically deposited DIP/PEDOT:PSS, and that of 100 nm DIP-NCs on a vertically deposited 10 nm DIP underlayer on PEDOT:PSS (blue dash curve). (b) UV-VIS absorption spectra of the 50 nm sample (black curve), 20 nm sample (red dash curve) and the NC-based sample (blue point curve) dissolved from the substrate in equal amount of solvent and measured in solution.

Since the DIP structure and molecular orientation varied between planar and NC devices, the absorption characteristics of DIP of corresponding samples are compared in Fig. 4.2.13. On average, a 50 nm planar film absorbs 1.5 more photons than the NC structure (10 nm underlayer plus 100 nm columns), but clearly, due to the inherent structural differences, their absorption spectra cannot be directly compared. Therefore, individual samples of both types were fully dissolved in a defined volume of 1,2-dichlorobenezene to measure the total amount of DIP contained therein. It was found that the volume of DIP present in the NC-OPVCs equals that of a 20 nm thick DIP film fabricated by vertical deposition with Fig. 4.2.13b showing a comparison of the respective solution spectra. Thus it is apparent that the NC sample exhibits a significantly higher absorbance than the vertically deposited sample

(normalized to the number of molecules present in each sample). This finding can be understood by the different molecular orientation of DIP in the planar film and in NCs. Planar films comprise a fiber-textured with a preferential vertical molecular orientation ("2D-powder"), while the NCs exhibit significantly less-textured growth (more "3D-powder like") and a substantial fraction of "lying" molecules. As the absorption is dominated by the fundamental HOMO-LUMO transition (*c.f.* in Fig. 4.2.13b), which is polarized along the long molecular axis of DIP, this transition is less efficiently excited in the vertically deposited film than in the DIP-NCs.[Heinemeyer, 2008a]

Overall, with less DIP molecules (by a factor of 0.4, as deduced from UV-VIS) and, therefore, lower total absorption by DIP NCs (*c.f.* Fig. 4.2.13a), the power conversion efficiency (η) of NC-OPVC reaches 1.8 %, significantly larger than that of the stronger absorbing planar structure (bilayer OPVC, η = 1.4 %) as listed in Table 4.2 (Note: The same measurement conditions are utilized for both structures without using the solar simulator. Without spectral corrections the efficiency is in the range as reported in the literature for similar devices [Steindamm, 2012, Gruber, 2013, Schuenemann, 2013]). In comparison to the bilayer OPVCs, more photo-generated excitons in NC-OPVCs can reach the donor/acceptor interface for dissociation. This is due to the increase of the active interface area in the NC heterojunction by ca. 20% compared to the planar heterojunction. This is less than the overall efficiency increase of almost 30%, therefore, another mechanism may contribute beneficially. The intrinsic vertical distribution of the donor/acceptor interface introduced through the NCs covers a wider range of high optical intensity, which may be generated by interference effects through reflection at the back electrode [Gruber, 2013, Kurrle, 2008, Opitz, 2010b, Stübinger, 2001, Peumans, 2003b]. As a result the impact of comparably short exciton diffusion length reduces in C60 when employing a thicker film. Moreover, the lying phases may positively influence J_{sc} and FF, but due to the unknown spatial distribution of the two DIP orientations the contribution cannot be quantified.

b. DIP column/PCBM

In addition, PCBM was also tested as the electron acceptor material, spin coated on to DIP nanocolumn as electron donor using exact same method for PEN/PCBM OPVCs. The concentration of 25 mg/ml PCBM was spin coated at 20 rps onto DIP column structure in the glovebox (sometimes DIP column was annealed with 80 ℃ for 10 minutes before PCBM spin coating). However, this solution process did not proceed as expected since the solvent chlorobenzene that was used to dissolve PCBM also could dissolve DIP molecules. Thus in the process of PCBM solution spin coating, DIP columnar structure was ruined due to re-dissolving (*c.f.* Fig. 4.2.14).

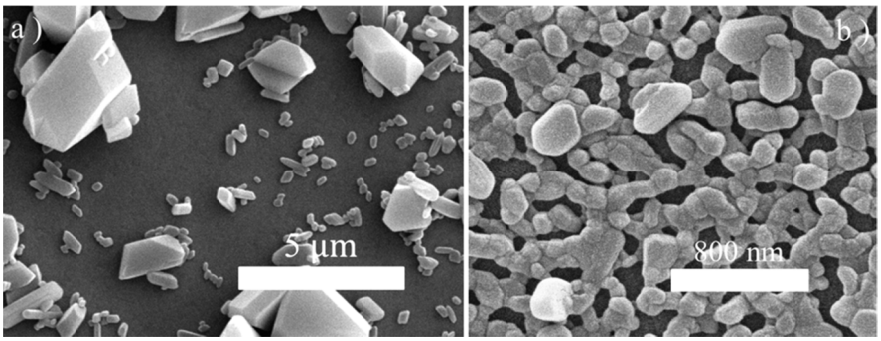

Fig. 4.2.14 SEM micrographs of re-dissolving DIP film by chlorobenzen solvent. Two drops of chlorobenzen solvent were spin-coated onto DIP column prepared with GLAD (a) for 1 min at 25 rounds per second (rps) and for (b) 30 s at 10 rps and afterwards annealed at 120℃.

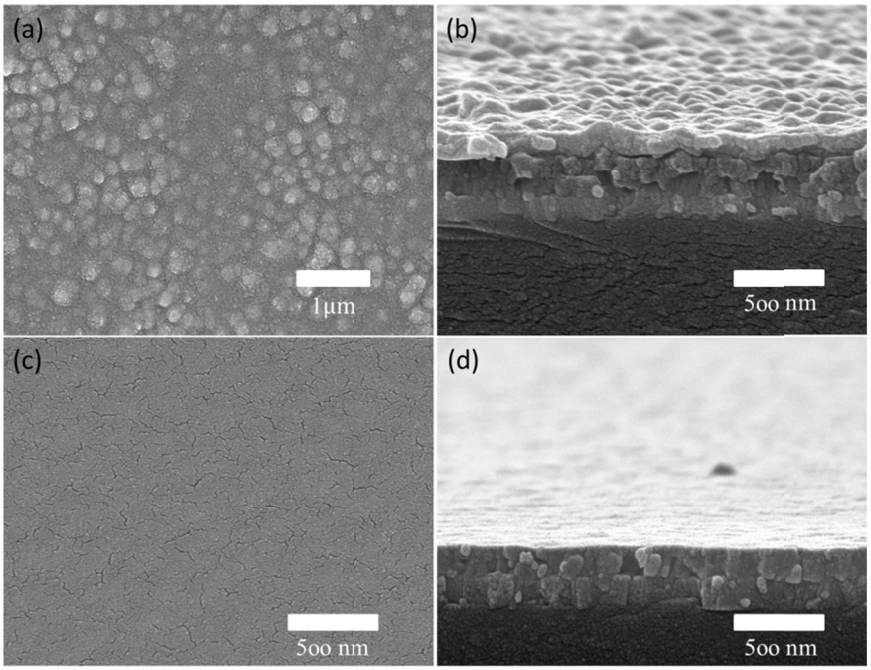

Fig. 4.2.15 SEM micrographs of PCBM on top of DIP NCs. (a-b) Top and cross-section view of thin PCBM layer on DIP NCs; (c-d) top and cross-section view of thick PCBM layer on DIP NCs.

To bypass the re-dissolving problem, the other solvent chloromethane was used to dissolve PCBM instead of chlorobenzene. The solubility of PCBM in chloromethane is much lower than that in chlorobenzene, ≤15 mg/ml. From the top-view and cross-section view of the SEM images (Fig. 4.2.15a-b), low concentration (6 mg/ml) PCBM spin-coated onto DIP NCs succeeded in the infiltration of NCs structure. In addition corrugated topography was led by the thin PCBM film thickness since it was unable to fulfill the valleys. When using 12

by the thin PCBM film thickness since it was unable to fulfill the valleys. When using 12 mg/ml PCBM solution for spin coating, the surface is rather flat as shown in Fig. 4.2.15 c-d. The OPVCs were fabricated by depositing BCP and Sm on top subsequently. The J-V characteristics were recorded under 25 mW/cm^2 illumination from a halogen lamp in vacuum with the results shown in Fig. 4.2.16. From the trends it can be seen that the J_{sc} is 0.61 mA/cm^2 and V_{oc} is 0.56 V and they are both smaller than those of DIP/C60 devices, as well as the fill factor, consequently the PCE of the devices is lower. Moreover, the device reproducibility is poor due in part to the uncontrollability of PCBM solution spin coating. Due to the limitation of PCBM solubility in new solvent chloromethane (12mg/ml), this results in an inhomogeneous PCBM layer thickness on top of NCs.

In total, using chloromethane as solvent to bypass the re-dissolve issue is incapable of optimizing the performance of OPVCs with this solution process until an appropriate solvent with solubility for PCBM larger than 20 mg/ml is identified. However the solubility for DIP extremely must be low so that the DIP columnar structure can survive the solution spin coat process similar to the devices consisting of PEN/PCBM.

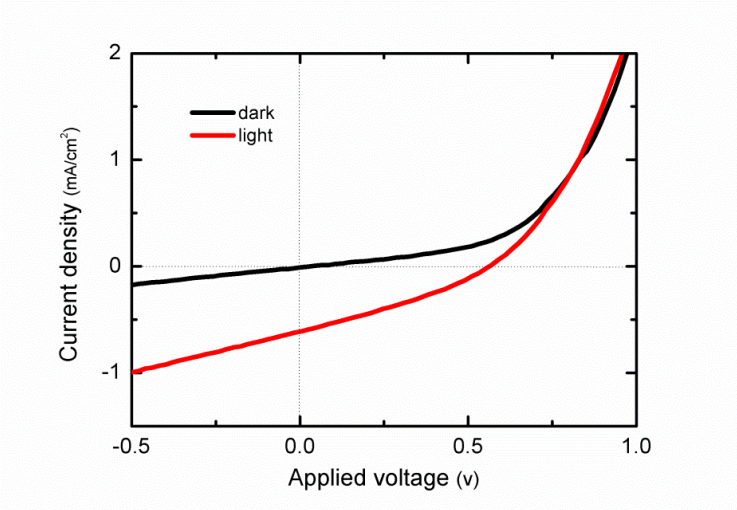

Fig.4.2.16 J-V characteristics of OPVCs based on DIP NCs/PCBM heterojunction.

c. DIP on graphene[3]

Lying phase DIP is a promising material towards improving the light absorption when was applied to OPVCs for electron donor. In this section the morphology and absorption behavior of lying DIP on graphene substrate will briefly be discussed.

---

3. Graphene coated substrates were provided by the group of Prof. Müllen (Max Planck Institute for Polymer Research). Graphene that was grown using the chemical vapor deposition method was transferred to patterned ITO substrates to act as the anode.

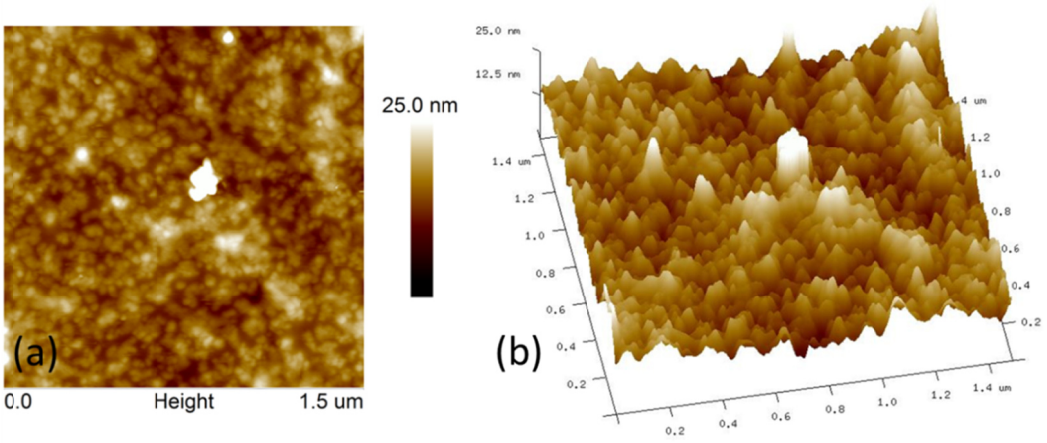

Fig.4.2.17 Morphology of graphene coated ITO substrate investigated by AFM. (a) 2D; (b) 3D.

As it was observed that lying phase DIP could effectively enhance light absorption, which is important for exciton generation rate, in this study thoroughly lying DIP have been explored and applied to OPVCs. ITO coated with graphene was used according to the study on highly order pyrolytic graphite (HOPG) in which it was shown that DIP adopted a lying-down configuration facilitated by DIP/graphite interfacial $\pi-\pi$ interaction [Huang, 2009]. Before depositing DIP on the graphene substrate, high temperature (≥ 500 ℃) annealing in high vacuum conditions ($\leq 10^{-7}$ mbar) was carried out to repair defects caused during transfer. However, due to the roughness of ITO substrate, in particular the patterning ITO step (approximately 120 nm), the flat graphene layer was turned to corrugation as shown in Fig.4.2.17.

The angle dependent absorption spectra of DIP film on graphene and PEDOT:PSS are presented in Fig.4.2.18. As can be seen from the figure, on graphene substrate, the absorption is weakened upon increasing the incident angle. In contrast on PEDOT:PSS, the absorption is enhanced when the incident angle is increased. This observation correlates with the estimation of lying DIP orientation on graphene due to its HOMO-LUMO transition polarized along molecular long axis. The morphology of 100 nm DIP film on graphene substrate as studied by AFM is shown in Fig.4.2.19(a). Surprisingly, the DIP film on graphene exhibits a rms of 18 nm, which is similar morphology to that of 100 nm DIP columns on PEDOT:PSS (*c.f.* Fig.4.2.19b). Therefore, there are huge morphological differences between vertically deposited DIP on graphene and those on ITO. This phenomenon is also verified by the SEM cross-section view (see Fig.4.2.2b), the morphology shows rod-like islands in the film. The structural difference might be induced by $\pi-\pi$ DIP/graphene interfacial interaction in the first monolayer deposition with this force capable of extending several tens nanometers in to the bulk.[Huang, 2009]

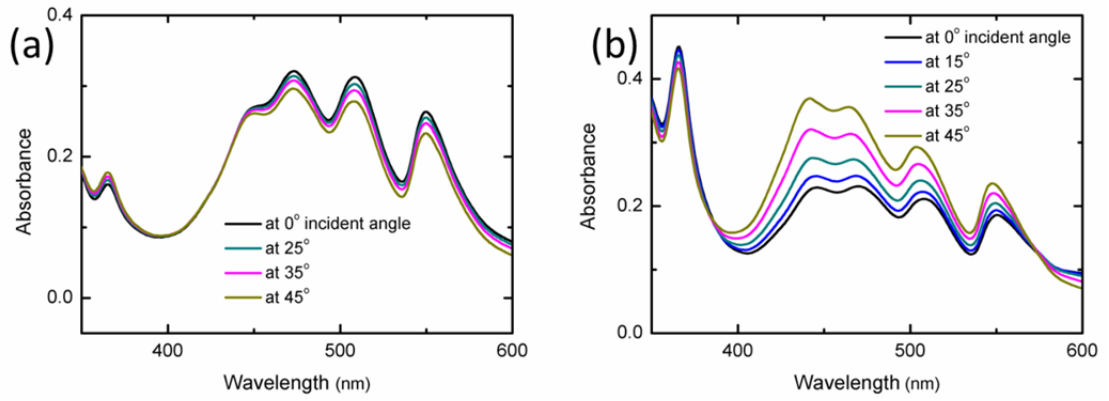

Fig.4.2.18 (a) Angle dependent absorption spectra of vertically deposited DIP film on a graphene substrate. (b) Angle dependent absorption spectra of vertically deposited DIP on PEDOT:PSS. The film thickness monitored with quartz microbalance for both samples is 50 nm. The incident angle is defined by the angle between incident light and the substrate surface normal.

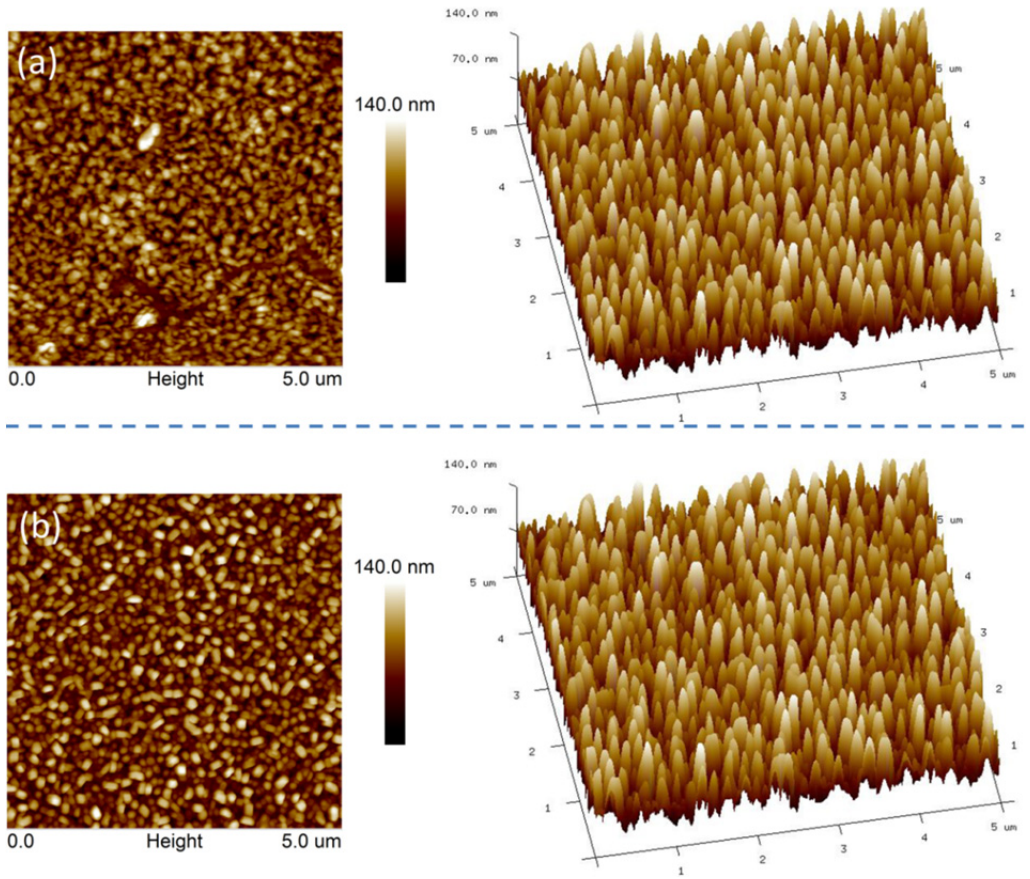

Fig.4.2.19 Morphology of DIP on graphene substrate with vertical deposition (a) and on PEDOT:PSS substrate with GLAD (b). Both were investigated by AFM measurements.

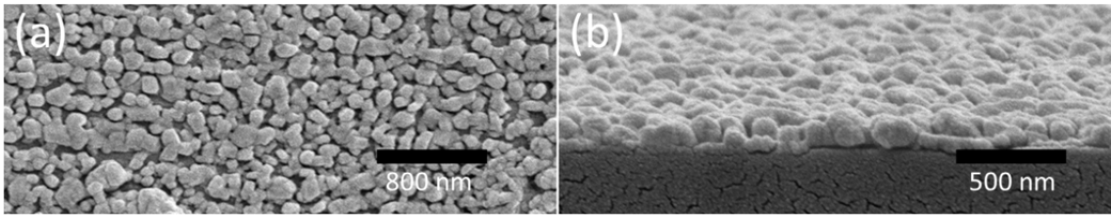

Fig.4.2.20 Morphology of DIP film on graphene substrate with vertical deposition, investigated by SEM. (a) Top-view. (b) Cross-section view.

OPVCs were fabricated based on the rod-like DIP film, employing C60 as electron acceptor, BCP as blocking layer and Sm as top electrode. However, no working OPVCs could be obtained, even without diode characteristics, due to current short-pass between the two electrodes as when using pentacene on ITO to fabricate OPVCs (see section 4.1). Although the application of graphene in OPVCs combined with lying DIP was unsuccessful, tuning molecular orientation may still be a very efficient method to optimize the performance of OPVCs via improving the active organic layers' absorption. Furthermore, graphene was assumed to be a very promising candidate for replacing the ITO as the electrode for organic optoelectronic devices in the future, if the conductivity of grapheme could be further increased.

4.2.4 Summary

The morphology and structure of crystalline DIP nanocolumns grown by GLAD on pristine and PEDOT:PSS coated ITO substrates has been demonstrated and such structures applied in OPVCs. Despite the fact that the DIP volume in NC-based OPVCs was less than one half of that in planar heterojunctions (with also an overall lower absorption by the NCs), the power-conversion efficiency of the solar cells increased from 1.4% (planar) to 1.8% through using DIP-NCs in the active layer. This noteworthy finding is explained as follows. (i) An increase of active interface area between DIP-NCs and the surrounding C60 acceptors which improves charge-carrier generation through exciton dissociation at that interface. (ii) A more random orientation of crystalline DIP grains in the NCs enhances light absorption in comparison to the fiber-textured, upright standing DIP in vertically deposited films. (iii) The vertically oriented donor/acceptor interface enabled by the NCs is further beneficial for light absorption, since it covers a wider vertical range, and light intensity variations due to interference effects can be accommodated. Further investigation of the contribution of molecular orientation on light absorption for OPVCs was carried out by growing lying DIP on a graphene substrate. Unfortunately, due to the short current induced by the morphology issues of lying DIP on graphene, no working OPVCs were produced. The development of a process for the preparation of a smoother lying DIP on graphene is certainly a worthwhile direction for future investigations. Nevertheless, the present work underlines the key role of

structure and morphology in OPVCs and demonstrates that their targeted optimization by glancing angle deposition offers good perspectives for pushing further the limits of organic photovoltaics in future applications.

4.2.5 Experimental details

ITO coated glass substrates (Präzisions Glas & Optik, sheet resistance < 20 Ω/sq, surface roughness (rms): 2 nm) were sonicated for 10 min in acetone and, subsequently then, in isopropanol. After cleanness, ITO coated substrates were also patterned for devices fabrication as described in section 4.1.11. UV-ozone-treatment was applied to improve the wetting of the substrate by an aqueous suspension of the intrinsically conducting polymer poly(ethylene-dioxythiophene): poly(styrenesulfonate) (PEDOT:PSS) (H.C. Starck GmbH, HIL 1.3) employed as substrate for OPVCs. PEDOT:PSS was spin-coated and subsequently annealed at 200℃ for 5 min under ambient conditions to desorb residual water. DIP was purified twice by gradient sublimation. NCs were grown by GLAD, the material sublimed from a resistively heated ceramic crucible with a deposition rate of ca. 0.1 nm/s (quartz crystal microbalance, base pressure < 5×10^{-7} mbar) at room temperature. The incident angle of the molecular flux (α) with respect to the substrate surface normal was set to 84^{o} (*c.f.* Fig. 4.2.1) and the substrate rotation frequency (ω) was 6 revolutions per minute (computer-controlled step-motor). OPVCs were completed with a 75 nm thick C60 (99.9%, Sigma-Aldrich) layer deposited at a rate of 0.02 nm/s on the DIP films/NCs in another vacuum chamber (base pressure < 2×10^{-8} mbar). Sample transfer between the chambers was done through ambient conditions. A 6.5 nm thick bathocuproine (BCP, 96%, Sigma-Aldrich) layer was deposited onto the donor/acceptor structure followed by a 100 nm thick samarium (Sm) layer that was used as the cathode. The current density *versus* voltage (J-V) characteristics were measured *in-situ* in dark and under illumination (25 mW/cm^2, Solux C6 halogen lamp, close to daylight spectrum in the visible region) with a Keithley 2400 SourceMeter®. (Device performance measurement system is same as description in section 4.1) The sample morphology was investigated with a Bruker Multimode-8 atomic force microscope (AFM) and a HITACHI S-4100 field-emission scanning electron microscope (SEM), using the latter after sputter-coating the samples with a thin gold layer to avoid sample charging. Optical absorption spectra (UV-VIS) were recorded with a PerkinElmer Lambda 900 spectrometer. X-ray diffraction experiments were carried out in inert (He) atmosphere at beamline W1 at the synchrotron radiation source HASYLAB (DESY, Germany) using a primary beam energy of 10.5 keV and a one-dimensional position sensitive detector (Mythen 1K, Dectris) mounted in the z-direction covering a range of out-of-plane scattering angles of ca. 3.8°. For grazing-incidence diffraction, five scans at fixed out-of-plane position were performed for every reciprocal space map [Salzmann, 2012b]. Specular X-ray diffraction (XRD) on the PEDOT:PSS-substrate samples was performed with a Philips X'Pert system in Bragg-Berntano geometry (sealed Cr-tube, secondary HOPG monochromator). Graphene annealing processing was carried out under high vacuum conditions (base pressure

< 10^{-7} mbar) and heated up to 500 ℃ on the ceramic covered hot plane at least for one hour and cooled down automatically until it reached the ambient temperature.

4.3 F4-TCNQ doping in polyfuran

In this section of the thesis, the characteristics of molecular doped polymeric semiconductor will be investigated. F4-TCNQ as a *p*-type dopant is mixed with polyfuran and applied in the fabrication of organic photovoltaic cells combining with C60 as electron acceptor. In this section attention will be drawn to the definition of the doping ratios used in this work. For example, 1% doping refers to the addition of one F4-TCNQ molecule per 100 monomer units (see section 3.2) of polyfuran.

4.3.1 Introduction

For several decades, organic photovoltaic cells (OPVCs) have been extensively investigated owing to the advantage of low-cost and simplicity of large-scale processing. [Tang, 1986, Tang, 1975, Ramsdale, 2002, Koster, 2005, Snaith, 2006, Geiser, 2008, Jørgensen, 2008, Søndergaard, 2013, You, 2013a, You, 2013b] Basic strategies used to improve the power conversion efficiency are available. For example, the short-circuit current density (J_{sc}) may be enhanced by increasing light absorption by using low band gap polymers[Bundgaard, 2007] or by optimization of blend film morphology [Thompson, 2008]. Another approach towards improving power conversion efficiency is to the increase the open-circuit voltage (V_{oc}) via maximizing the photovoltaic gap (E_{pvg}), which is the energetic difference between the valence band onset (VB-onset) of the donor polymer and the onset of the LUMO of the acceptor molecule at the heterojunction.[Wilke, 2012] One material parameter that influences both J_{sc} and V_{oc} in OPVCs is the hole and electron mobility of the donor and acceptor material respectively. A mobility that is too large can be detrimental for the device performance as seen in a decrease in V_{oc}.[Tress, 2011b] On the other hand J_{sc} is limited by the mobility of the slowest carriers when the photo current is space charge limited. As most polymer/fullerene based OPVCs suffer from low hole mobility in polymers in comparison to the high electron mobility in the fullerene[Tunc, 2012, Melzer, 2004, Koster, 2005], balanced mobilities are required for high efficiency. To increase the hole mobility in the polymer, electrical doping can be applied by introducing dopants such as F4TCNQ into polymer films.

Doping organic semiconductors, which is one of the most effective methods of improving the characteristics of organic electronic devices, is selected in order to obtain analogous benefits as for doping in inorganic semiconductors, which has been well proved and explained theoretically and experimentally. Doping inorganic semiconductors enables the precise adjustment of band positions and improvement of conductivity, thus tuning the optical and electrical properties. In principle, the doping mechanism of organic semiconductors (OSCs) is similar to those in inorganic semiconductors where holes are generated by removing electrons in the highest occupied orbital states or donating electrons in the lowest unoccupied orbital states through ionization of the dopant. Recently, stable doping of OSCs

has been demonstrated by adding strong molecular dopants to conjugated polymers or small molecules. Consequently the conductivity of doped film increases by several orders of magnitude and can be used as charge transport layers in organic light emitting diodes and organic photovoltaic cells (OPVCs). [Lüssem, 2013, Brutting, 2012, Blochwitz, 1998, Zhou, 2002, Meerheim, 2006, Reineke, 2009] [Sun, 2009, Salzmann, 2012a, Lüssem, 2013, Pingel, 2013, Mendez, 2013, Duong, 2013, Mityashin, 2012] In the case of poly(3-hexyl -thiophene) (P3HT) for high doping ratios [>1% (F4TCNQ:thiophene units)], the mobility, and therefore the conductivity, increases linear [Pingel, 2012, Pingel, 2013]. In addition, for concentrations <2% (F4TCNQ: thiophene units), p-type dopant molecules reduce the interfacial recombination via charge transfer excitons and results in the favorable formation of separated carriers[Deschler, 2011].

In this section, the effect of p-type electrical doping of polyfuran on the performance of a bilayer heterojunction OPVCs with C60 as acceptor material is presented. To analyze the doping effect, the absorption characteristics, conductivity and morphology of polyfuran thin film with different F4-TCNQ doping ratio were investigated. As expected for high dopant concentrations (still lower than 2%) J_{sc} significantly increased. For even higher concentrations such as an over doped system (up to 40%), unexpectedly V_{oc} significantly increased and J_{sc} was just slightly higher in comparison to the undoped system. Ultra violet photoelectron spectroscopy (UPS) data showed an increase in the photovoltaic gap, a finding that supports the predicted increase of V_{oc} at very high dopant concentrations. In addition, the effect of high doping concentration (1%) polyfuran treated as the hole transport layer was investigated in combination with ZnPc as the electron donor and C60 as the electron acceptor.

4.3.2 Absorption, morphology and conductivity

a. Absorption

The normalized UV-Vis absorption spectra of F4-TCNQ doped polyfuran thin films with varied doping ratios starting with pristine polyfuran until 100% F4-TCNQ doped polyfuran, i.e. on quartz substrates is depicted in Fig.4.3.1. As indicated by the absorption onset of pristine PF, the optical gap is determined to be 2.30 eV which is remarkably close to the theoretically predicted value of 2.38 eV.[Zade, 2006] Upon doping, pronounced sub-band gap absorption features develop in addition to the absorption of pristine polyfuran. A qualitative comparison of the NIR region to the known spectra of ionized F4-TCNQ anions [Torrance, 1980, Dixon, 1989] allows a clear identification of the prominent 1.43 and 1.62 eV peaks for the absorption of singly negatively charged F4-TCNQ (Fig.4.3.2a). Due to the scattering effect induced by inhomogeneous morphology (Fig.4.3.3), the second ionic peak at 1.62 eV could not be observed on the sample of pristine F4-TCNQ film, but was observed in solvent as shown in Fig.4.3.2b. The broad absorption bands between 1.3 and 1.8 eV and the absorption below 1.1 eV can be attributed to polyfuran polarons similar to P3HT. [Pingel, 2013] For very high doping concentrations the absorption above 3 eV is also enhanced due to

an increasing amount of neutral F4-TNCQ molecules. Consequently, efficient charge transfer between polyfuran and F4-TNCQ was only guaranteed for lower doping concentrations.

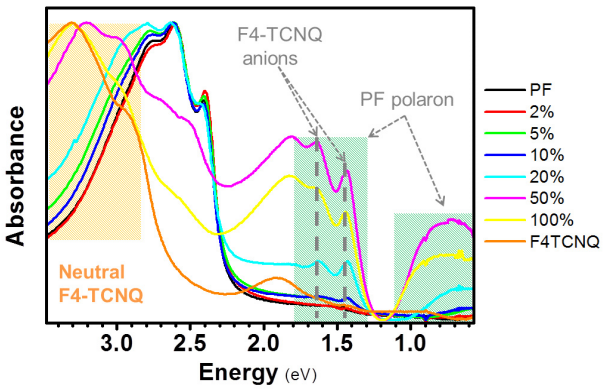

Fig.4.3.1 UV-VIS absorption spectra of polyfuran (red curve), F4-TCNQ (cyan curve) and mixtures of polyfuran and F4-TCNQ at different ratio: 50:1 (olive green curve), 20:1 (blue curve), 10:1 (wine red curve), 5:1 (grey curve), 2:1 (orange curve) and 1:1 (dark yellow curve). Vertical yellow zones smaller than 1.1eV and in between 1.3 eV and 1.8 eV indicate the absorption of broaden band induced by delocalized polar excitation. Dashed lines are the ionic peak of F4-TCNQ.

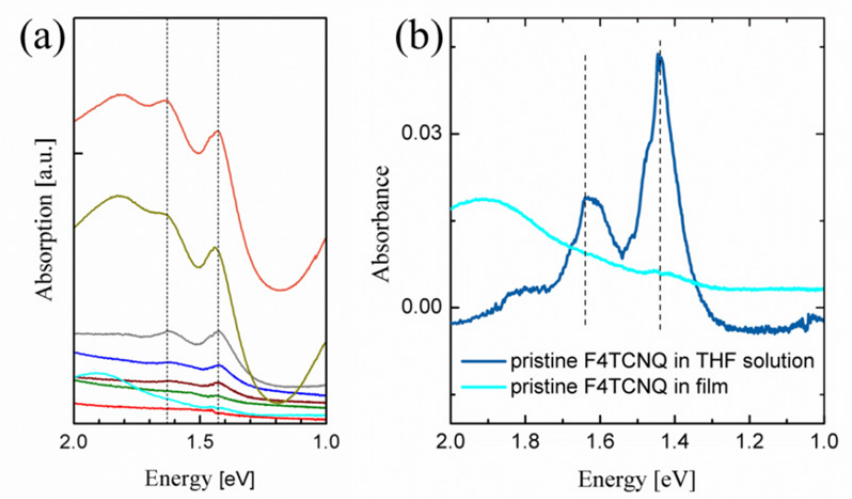

Fig.4.3.2 (a) Zoom-in on the UV-Vis absorption spectra from Fig.4.3.1 in the near infrared region. (b) UV-Vis absorption spectra of pristine F4-TCNQ in film and THF solution respectively. The cyan curve represents absorption in film while the dark navy curve presents absorption in solvent.

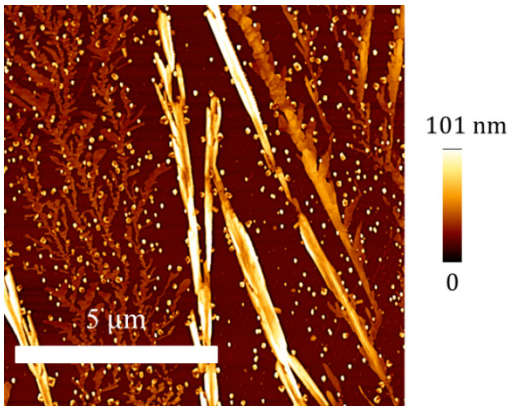

Fig.4.3.3 Morphology of F4-TCNQ on quartz glass substrate investigated by AFM.

b. Morphology

To gain insight into the morphology of pristine and doped polyfuran films, AFM images are shown in Fig.4.3.2. The topography of pristine and 1% F4TCNQ doped polyfuran (see Fig.2.3.4 a-b) is rather smooth and homogenous, with average structural size of ca. 150 nm. In contrast, 10% and 40% F4TCNQ doped PF films (see Fig.4.3.4 c-d) exhibit a rough surface morphology. The uniform polyfuran morphological structure is severely disrupted by small high islands that grow further to form distinct needle-like features on the surface for very higher doping concentration (40%). This growth mode is typical for pristine solution processed F4-TCNQ films (see also Fig.4.3.3). Consequently, the system has reached the solubility limit of F4TCNQ in the polyfuran in the solid phase for very high dopant concentrations and thus pristine-F4-TCNQ solidified at the polymer surface. The high concentration of phase segregated F4-TCNQ at the surface of the polymer film can also be caused by the spin coating process. A two component system with a composition that is unstable to small fluctuations in concentration, e.g. due to limit solubility in the used solvent, will spontaneously phase separate.[Nilsson, 2007, Balsara, 1996, Cahn, 1958, Geoghegan, 2003, Smith, 2010] This effect is enhanced toward high dopant concentrations.

As a result of low solubility (2.8 mg/ml) of polyfuran in THF solvent (polyfuran in THF is relative stable), the thickness of film obtained from spin coating was only a few nanometers, even when employing low spin coating rate (15 rps). This thickness of polyfuran was too thin to be used as the only electron donor layer in OPVCs. To obtain a thicker film, a two-step spin coating was applied. First a lower spin coating rate (10 rps) was applied for spin coating, which produced a rough surface after drying (see Fig.4.3.5b). Secondly, spin coating with 15 rps with saturated solution was used to reduce the surface roughness. (The low spin-coating surface is too rough to obtain a quality image with AFM, thus the SEM micrograph is only considered as shown in Fig.4.3.5b.) In this way, polyfuran thickness can be increased to 30 nm. As further demonstrated by absorption measurements (see Fig.4.3.5a) on the same substrate and using the same solution, the absorbance peak value of the film employing the

two spin-coating procedure is much larger than that of the film obtained with a single spin-coating.

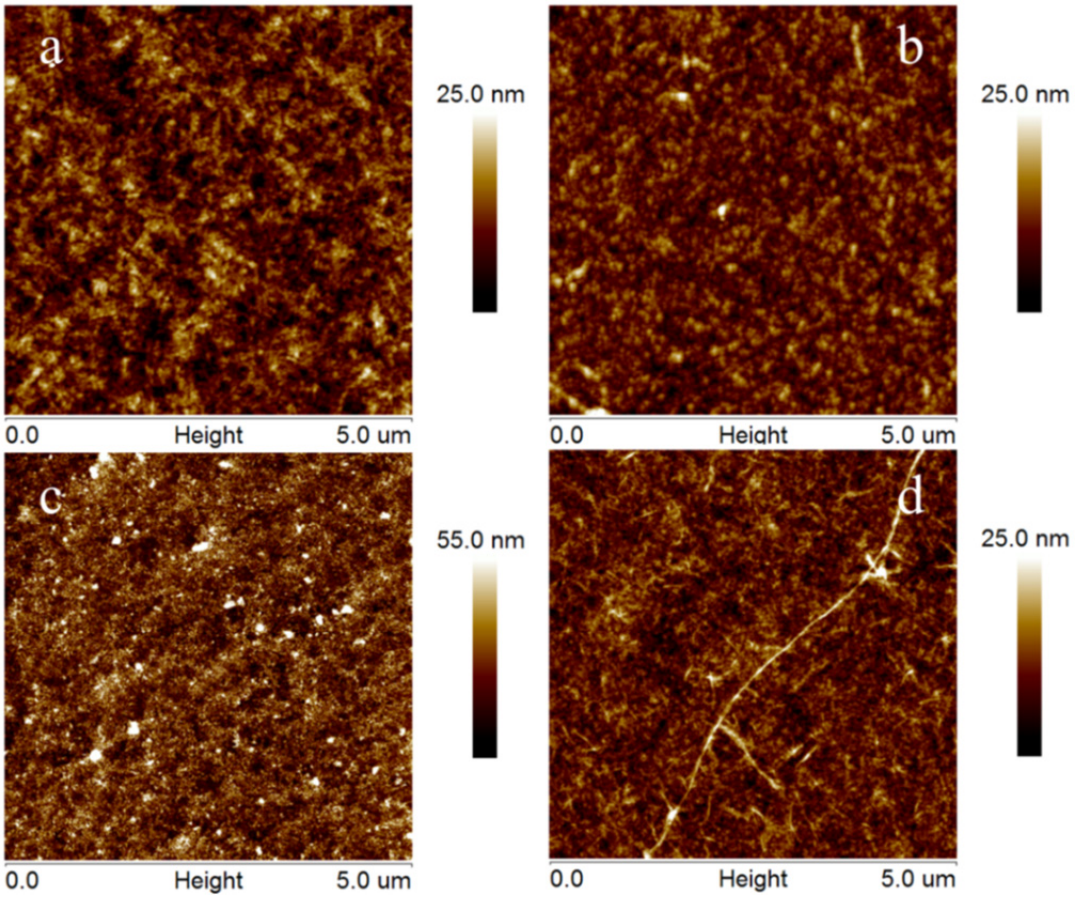

Fig.4.3.4 AFM micrographs of (a) spin coated pristine polyfuran/PEDOT:PSS film, (b) F4-TCNQ:polyfuran (1:100) mixture/PEDOT:PSS, (c) F4-TCNQ:polyfuran (1:10) mixture/PEDOT:PSS and (d) F4-TCNQ:polyfuran (2:5) mixture/PEDOT:PSS.

Conductivity

Fig.4.3.6 shows the conductivity of doped polyfuran films with a film thickness of 30 nm. Similar to the prototypical case of F4-TCNQ doped P3HT the conductivity increased rapidly for low doping ratios (lower than 2%). In this region it has been shown for P3HT that both the mobility and the density of states (DOS) drastically increases with doping concentration.[Pingel, 2013, Arkhipov, 2005b] The improvement in transport has also been attributed to the filling of traps by the dopant-induced carriers [Mendez, 2013, Olthof, 2012, Salzmann, 2012a, Gao, 2003, Gao, 2001, Pingel, 2013]. Beyond a doping ratio of 2%, the conductivity decreased and is likely due to the morphological changes determined by the AFM results. Due to the formation of intercalated areas of pristine F4-TCNQ, charge transfer might be significantly impeded. Note that polyfuran films are amorphous.[Gok, 2005, Sen,

2008] Consequently, a decrease in crystallinity did not decrease the conductivity. However, at the moment it is impossible to exclude improved ordering in the films with low dopant concentration as observed for poly(p-phenylenevinylene) blended with fullerene derivatives.[He, 2007, Melzer, 2004]

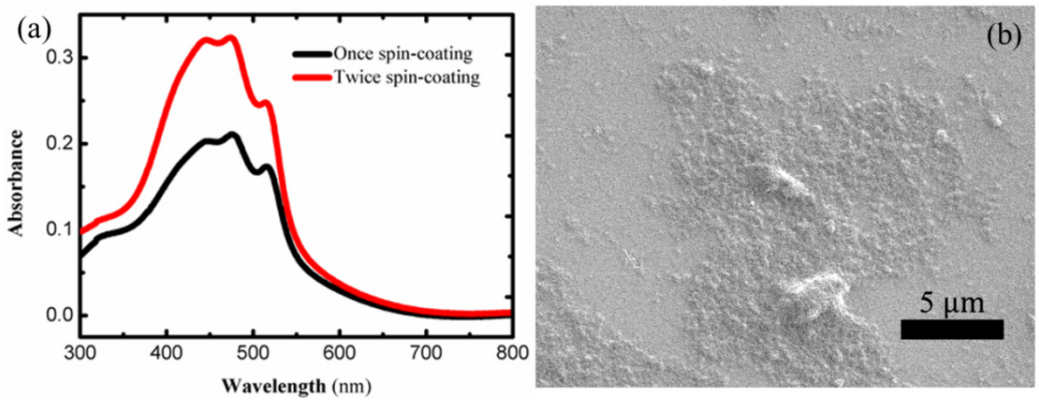

Fig.4.3.5 (a) Absorption spectra of polyfuran film on ITO substrate; black line is a single spin coating film (15 rps) and the red line is twice spin coating film (first: 10 rps; second: 15 rps). (b) SEM micrograph of rough polyfuran surface obtained with low spin-coating rate of 10 rps.

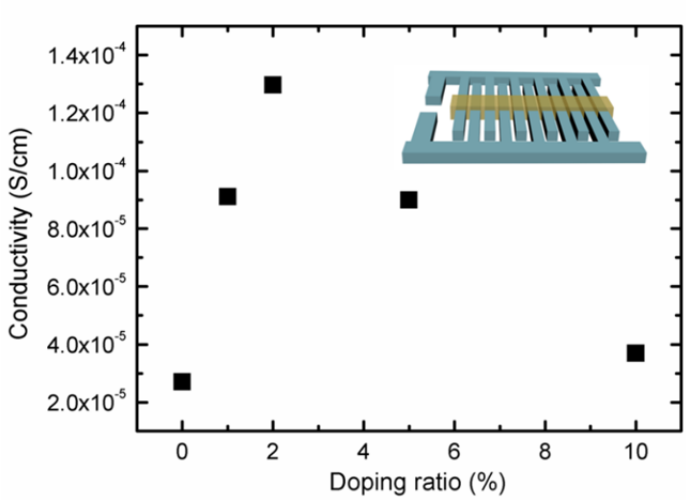

Fig.4.3.6 Conductivity of polyfuran films with an increasing amount of dopant F4-TCNQ. Inset: schematic representation of conductivity measurement using interdigitated electrodes of ITO on glass substrates with an organic film shown in semitransparent yellow.

4.3.3 Analysis of OPVCs

a. polyfuran/C60

Bilayer heterojunction organic photovoltaic devices were fabricated using 50 nm C_{60} as the acceptor deposited on doped and undoped spin coated polyfuran films (base pressure$<10^{-8}$ mbar). 6 nm BCP acting as a blocking layer and aluminum as the top electrode was deposited after C60. The device structure is presented in Fig.4.3.7. Fig.4.3.9(a) shows the logarithmic dark performance of pristine (device A), 1% doping (device B), 10% doping (device C) and 40% doping (device D) respectively. Again, based on the non-ideality diode equation (equation 4.1), the series resistance can be deduced from the slope of the logarithmically represented J-V characteristics in the exponential regime. For device A, B and C the series resistance are 270 Ω, 40 Ω and 340 Ω respectively. Unfortunately, it is impossible to measure the R_s for device D due to the presence of current leak. Benefiting from an increase in the conductivity, device B exhibits the lowest R_s, following Pouillet's Law

$$R = \frac{l}{\sigma S} \tag{4.2}$$

where σ is conductivity of the film, l is the active organic layer thickness and S is the active device area.

The short circuit current density (J_{sc}) (obtained under the illumination of 56 mW/cm^2) using pure polyfuran was quite low compared to state of the art polymer/PCBM devices.[Green, 2014] Nevertheless, 1% doping increased J_{sc} by a factor of two compared to the undoped polyfuran film as a result of the improved conductivity in the polymer while keeping the open circuit voltage (V_{oc}) at 0.2 V. However, higher dopant concentrations increased J_{sc} only by 30 % in comparison to the device with undoped polyfuran film, which correlates with the trend of the conductivity upon very high doping ratios. For dopant concentrations above 1% the V_{oc} increased by up to 0.39 V (at 40% dopant concentration). In order to understand this V_{oc} increase, the energy level alignment at the heterojunction was investigated using UPS measurements. As mentioned before, E_{pvg} is clearly related to V_{oc} (E_{pvg} is an upper bound to V_{oc})[Vandewal, 2009, Wilke, 2012]. As shown in Fig. 4.3.10a within the experimental error (50 meV) vacuum level (VL) alignment is established for the undoped system. The polyfuran VB-onset is located 0.40 eV below the substrate Fermi level (E_F) as shown in Fig.4.3.8. The ionization energy of HIL1.3 substrate is 5.60 eV. After depositing polyfuran on the substrate, in order to reach electronic equilibrium, the electrons were injected to the substrate from polyfuran film. This was done until the Fermi-level pinning was reached and the valence band onset was observed at 0.40 eV lower than the substrate Fermi-level, thus yielding an ionization energy of 4.8 eV.

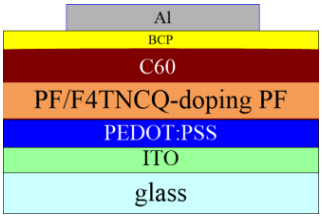

Fig. 4.3.7 Schematic representation of OPVCs structure.

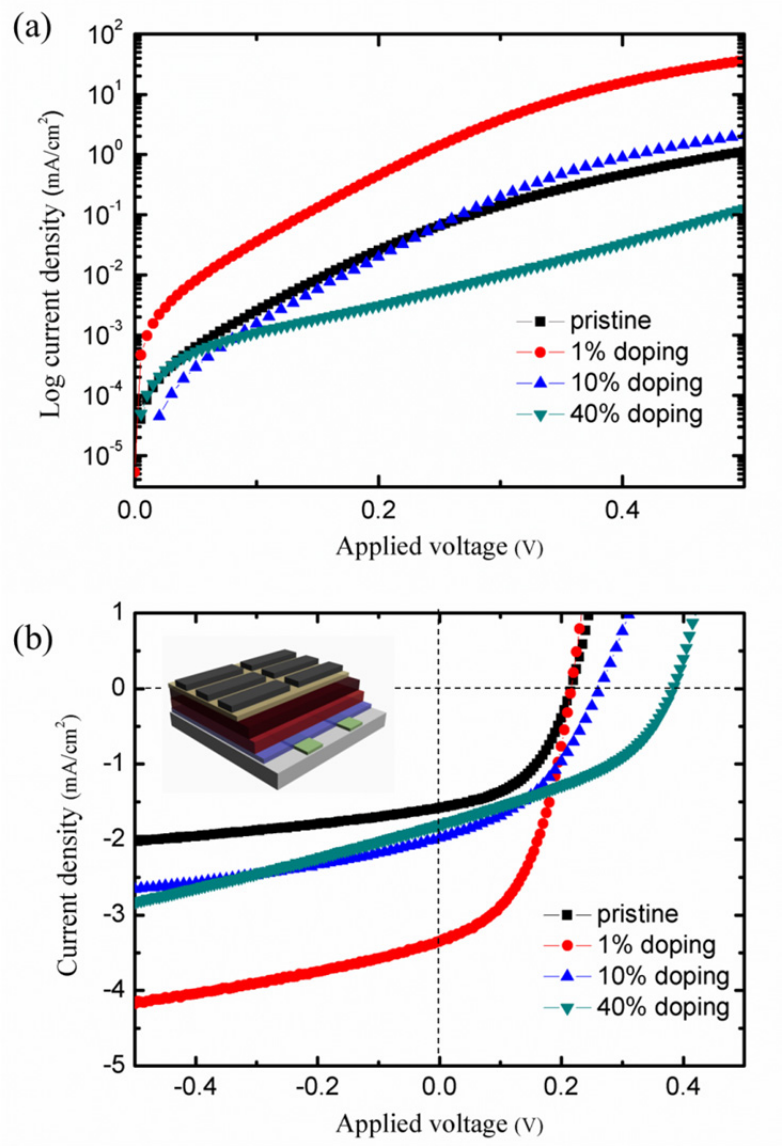

Fig.4.3.9 (a) J-V characteristics of OPVCs based on different dopant F4-TCNQ in dark in logarithmic representation. Black closed square symbols: pristine polyfuran, red dot symbols: 1% doping, blue up-triangle symbols: 10% doping and green down-triangle symbols: 40% doping. (b) J-V curve under illumination (56 mW/cm^2) in air. The device structure is shown in the inset and in the device from bottom to top the layers are glass/ITO/PEDOT:PSS/polyfuran (doped)/C60/BCP/Al.

However, the actual pinning level in the tail of the VB-onset could not ascertained from the UPS spectra due to extremely low density of states (DOS) in this energy range [Frisch, 2011, Hwang, 2009]. However, the VB-onset of F4-TCNQ doped polyfuran shifted to higher binding energy (BE) by 0.20 eV, mainly caused by an increased DOS and energetic disorder due to the doping effect. Consequently, the tail of the polymer VB-onset is broader and the pinning level is shifted further in the band gap[Arkhipov, 2005a, Pingel, 2013].

As can be seen in Fig.4.3.10b, the VL is also shifted in parallel resulting in a smaller work function (Φ) for the 1% doped PF film compared to the electron affinity of C_{60} (4.45 eV[Akaike, 2008]). This induces pinning of the C60 LUMO at E_F for the system and a VL shift to higher values [Niederhausen, 2012]. Most importantly, E_{pvg} is less affected by the different energy level alignment due to the 1% doping that is also shown by a constant V_{oc} in the device (see table 4.3). Nevertheless, E_{pvg} is explicitly enhanced for the very high doping ratios of 10% and 40%. This is due to an increase in Φ for the F4-TCNQ doped films that results in the LUMO being pushed further away from E_F. It is imperative to note that the Φ increase is not generated by the doping process itself but by the incipient interlayer formation of pristine F4-TCNQ between the doped polymer film and C60 at very high dopant concentrations. Due to the very large electron affinity of F4-TCNQ molecules [Kahn, 2003b] compared to the Φ of the doped polyfuran, film electrons will be transferred to the unoccupied state of F4-TCNQ to establish electrical equilibrium. These negative charges induce a local VL shift at the heterojunction with the C_{60} layer [Niederhausen, 2012]. Consequently, higher doping ratios also facilitate the formation of pristine F4-TCNQ domains on top of the doped polymer film, increasing the amount of negative charges and the doped polymer Φ. The calculated values of E_{pvg} and V_{oc} are shown in Table 4.3. Note that E_{pvg} and V_{oc} do not increase equally. This indicates an increase of charge recombination in highly doped OPCVs.

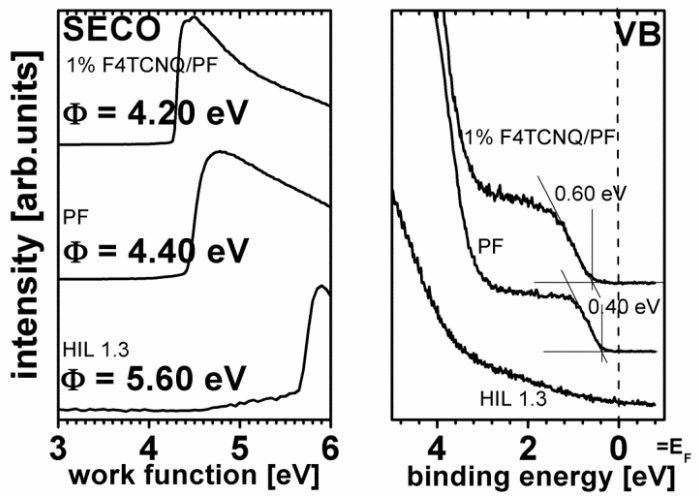

Fig.4.3.8 Secondary electron cut-off (SECO) and valance region photoemission spectra of the HIL1.3 substrate, pristine polyfuran film and 1% doped polyfuran film with F4TNCQ. PF denotes polyfuran and HIL1.3 is the PEDOT:PSS substrate.

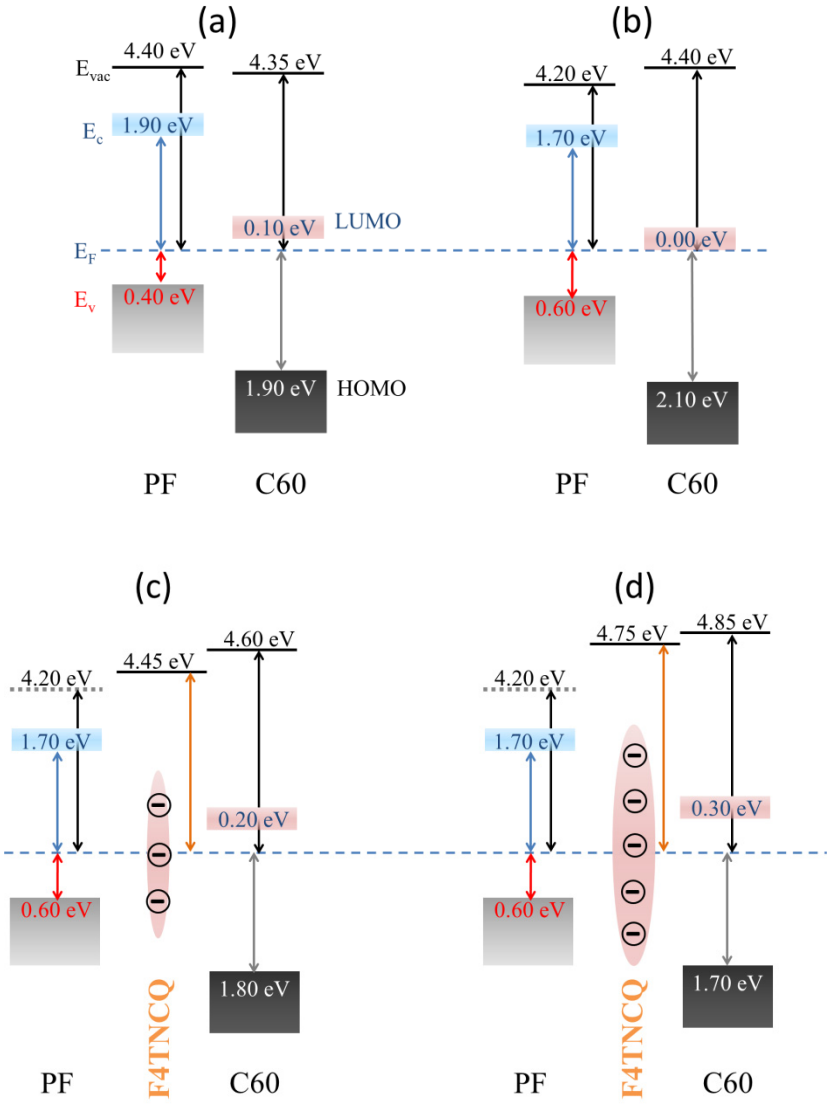

Fig. 4.3.10 Energy level alignment of the undoped PF/C_{60} (a) and F4TCNQ doped PF/C_{60} heterojunction with 1%(b), 10%(c), and 40%(d) dopant concentration. The pink areas between the PF and C_{60} layers indicate the increasing amount of pristine F4TCNQ domains at the doped polymer surface for very high doping ration. A few F4TCNQ molecules became negatively charged that increases the surface potential energy of the doped PF film. PF denotes polyfuran, E_F denotes the Fermi-level, E_v denotes the valence band, E_c denotes the conduction band and E_{vac} denotes the vacuum level.

Overall, through using F4-TCNQ interlayer facilitated by a large ratio of F4-TCNQ doping in polyfuran, the photovoltaic gap was effectively enlarged by pushing the valence band edge of doped polyfuran away from E_F and lifting the C60 HOMO onset towards E_F. Consequently, the V_{oc} of OPVCs employing doped polyfuran increased. However, owing to the morphology interruption in high doping ratio, the conductivity of doped polyfuran was reduced, which is the result of lower J_{sc} compared to OPVCs based on 1% doping polyfuran.

Table 4.3 The parameters of photovoltaic gap and experimentally measured V_{OC} of devices employing the dopant F4TCNQ at different ratios in polyfuran films.

Doping ratio	pristine	1% doping	10% doping	40% doping
photovoltaic gap (eV)	0.50	0.60	0.80	0.90
V_{oc} (V)	0.20	0.20	0.27	0.39

Therefore, the final power conversion efficiencies of devices with large V_{oc} were not improved as expected, an issue that might be resolved in the future. However, strong evidence is provided that molecular doping is an effective method for manipulating energy level alignment, which is important for the performance of organic electronic devices.

b. Polyfuran/ZnPc/C60

In order to compensate for the decrease of donor layer thickness, 10 nm thick ZnPc was deposited (0.2 nm/S) on top of polyfuran (doped), followed with C60 as the acceptor, BCP as a blocking layer and Al as the top electrode. The J-V characterization for this device layering is depicted in Fig.4.3.12. Another reference device consisting of only 50 nm ZnPc acting as the electron acceptor was also fabricated. Compared to the performance of device E (see Fig.4.3.12), the V_{oc} of device F was much larger, reaching 0.45 V (the HOMO of ZnPc is about 5.1 eV).[Tress, 2011b] However, the typical S-shape J-V curve for device F, which may be induced by imbalanced charge mobility in ZnPc (hole mobility: $\sim 10^{-6}\ cm^2/V \cdot S$) and C60 (electron mobility:$\sim 10^{-4}\ m^2/V \cdot S$) [Tress, 2011a, Terao, 2007, Itaka, 2006, Melzer, 2004]. Due to the low hole mobility in ZnPc, accumulated holes accumulated to a greater degree in ZnPc than in C60, leading to an increase in the electrical field close to the device anode until steady-state was reached where the external hole current equals the electron current. The schematic energy levels diagram in ZnPc/C60 heterojunction is shown in Fig.4.3.11. In region 1 close to anode, to remain neutral, space-charges are created. Originally, the current density at the external voltage of "principle V_{oc}" equals zero. However, within the build-up space charges, current density tended to zero before the application of the "principle V_{oc}", resulting in a lost on device V_{oc}.

The J_{sc} for both devices are almost equivalent although the absorbance of 50 nm ZnPc was higher than that of 20 nm doped polyfuran (see Fig.4.3.13), the absorption region differed, and the S-shape also caused a loss of J_{sc}. However in device G, the V_{oc} was maintained to that measured for device F while the S-shape was eliminated. The loss of hole mobility in thin ZnPc can therefore be compensated by underlying p-type doped polyfuran. Furthermore, larger J_{sc} in device G suggests that the excitons produced by polyfuran can be transported through ZnPc to the ZnPc/C60 interface and dissociated due to the large exciton diffusion

length in ZnPc (approximately 30 nm).[Kerp, 1998] Thus, the overall performance of device G was much better than that of reference device E and F (shown in Tab.4.4).

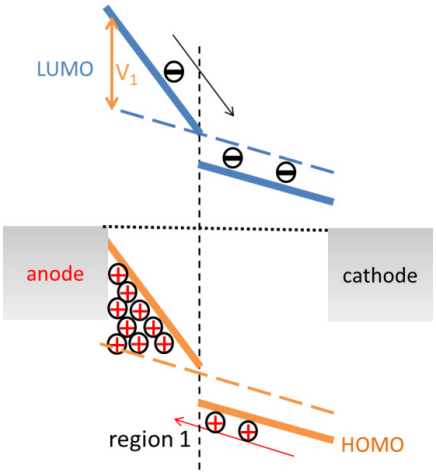

Fig.4.3.11 Schematic diagram of energy levels in ZnPc/C60 based OPVCs. V_1 is build-up potential in different regions respectively. [Melzer, 2004]

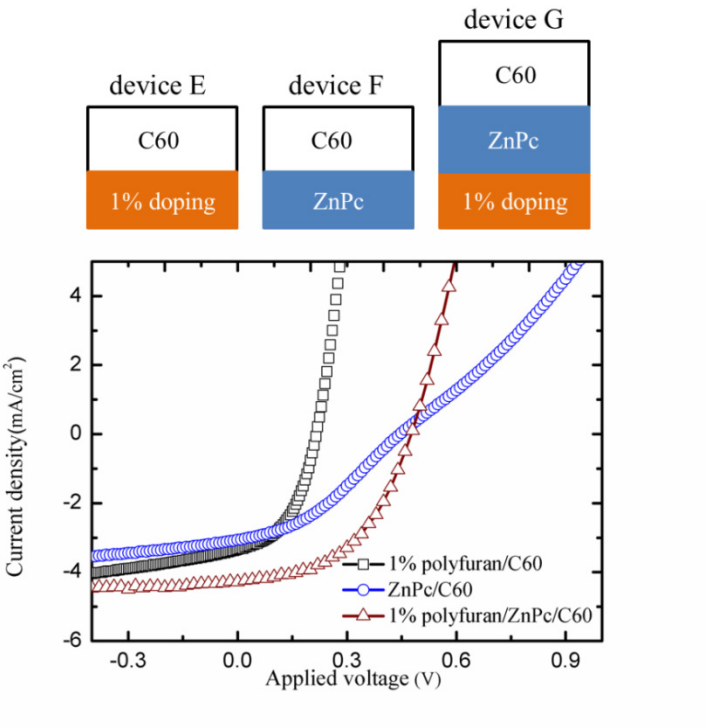

Fig.4.3.12. J-V characterization illuminated at 56 mW/cm^2 in air based on different device architectures. (device E) Open black square: ITO/PEDOT:PSS/ 20 nm 1% doping polyfuran/65 nm C60/6.5 nm BCP/Al, (device F) Open blue dot: Open black square: ITO/PEDOT:PSS/50 nm ZnPc/65 nm C60/BCP/Al and (device G) Open red wine triangle: ITO/PEDOT:PSS/20 nm 1% doping polyfuran/10 nm ZnPc/65 nm C60/BCP/Al.

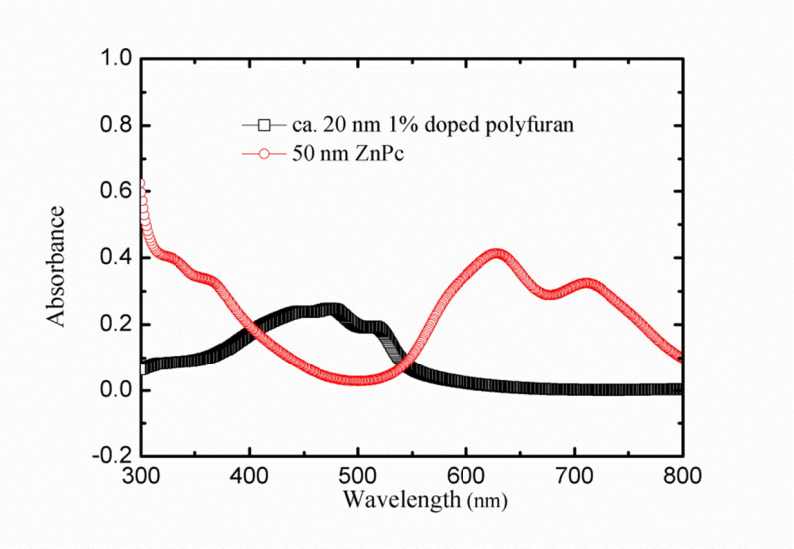

Fig.4.3.13 UV-Vis absorption spectra of 1% doped polyfuran and ZnPc.

Table 4.4 Key parameters of OPVC performance, as deduced from the J-V curves (*c.f.* Fig 4.34). V_{OC} is the open-circuit voltage, J_{SC} is the short-circuit current, FF is the fill factor, and η is the external power-conversion efficiency under 100 mW/cm^2 illumination (solar simulator) subject to ambient conditions.

	V_{oc} （V）	J_{sc} (mA/cm^2)	**FF**	**η**
Device E	0.22	3.35	0.45	0.4%
Device F	0.45	3.06	0.36	0.5%
Device G	0.48	4.28	0.48	1.0%

In total, in these doped polyfuran/ZnPc/C60 architectures, the performance of OPVCs improved significantly. Doped polyfuran played a very important role as a hole transport layer, while eliminating the S-shape that compensated for the current loss induced by low mobility in ZnPc, and also as an absorber, absorbing light at blue wavelengths.

4.3.4 Summary

F4-TCNQ was mixed with polyfuran with various ratios and spin-coated on substrates to

form films. The electronic characteristics of *p*-type doping polyfuran films have been investigated. For low doping ratios between 1% and 2%, the conductivity of doping polyfuran film could be significantly improved by one order of magnitude, which was very helpful for photogenerated charges transport, and thus improved the short circuit current density of the OPVCs. In addition, the doped polyfuran with high conductivity was also a good candidate for the hole transport layer, as shown in polyfuran/ZnPc/C60 architecture. For high doping ratio (above 10%), the photovoltaic gap was enlarged effectively due to accidently introducing a neutral F4-TCNQ layer, leading to larger V_{oc} for OPVCs compared to that of devices with low doping ratios. Unfortunately the morphology of high ratio doping polyfuran was severely affected and the conductivity lowered, which in turn affected the J_{sc} of OPVCs. Nevertheless, the results of UPS measurements confirmed the initial assumption that molecular doping enabled the tuning of the energy level alignment in OPVCs. Thus it demonstrates that the doping of organic semiconductors is a promising approach towards achieving the desired functionality for organic electronic devices.

4.3.5 Experimental details

Glass substrates coated with patterned indium tin oxide (Thin film Devices Inc., sheet resistance ≈ 20 Ω/sq) and quartz glass substrates were cleaned in an ultrasonic bath with acetone and isopropanol separately and afterwards with de-ionized water. UV-ozone-treatment was applied to improve the wetting of the substrate by an aqueous suspension of the intrinsically conducting polymer PEDOT:PSS employed as the substrate coating for OPVC application. PEDOT:PSS was spin-coated and subsequently annealed at 200℃ for 5 min under ambient conditions to remove residual water. Polyfuran purified with soxhlet extractions with methanol, hexane and chloroform separately was dissolved in tetrahydrofuran (THF) (2.5 mg/ml).[4] F4-TNCQ (≥ 98%, Tokyo chemical industry co. LTD) was dissolved in THF (0.7 mg/ml) in a N_2 filed glovebox. The doping was accomplished by mixing two solutions with designed monomer ratios under N_2 atmosphere (Glovebox, Braun GmbH), where 1% referred to the addition of 1 F4TCNQ molecule per 100 polyfuran monomer units (one monomer unit is shown in Fig. 3.14c). Pristine and F4TCNQ doped polyfuran films were spin coated on i) solvent cleaned fused silica substrates for UV-Vis absorption analysis measured with a PerkinElmer Lambda 900 spectrometer; ii) solvent cleaned interdigitated ITO contacts (electrode distance of 200 μm) on fused silica to measure the conductivity with a Keithley 2600 SourceMeter® and iii) PEDOT:PSS covered ITO substrates for OPVCs application. The conductivity of both pristine and F4-TCNQ doping polyfuran were measured with the Keithley 2610 SourceMeter@ on pre-etched interdigitated ITO substrate, with the thickness of ITO electrode measured as 120 nm (much thicker than film thickness).

4. Polyfuran is supplied by the group of Prof. Bendikov (Weizmann institute of science). The mass average molecular mass is 14.2 KDa.

Each photovoltaic device was completed by depositing C_{60} (0.2 nm/s) as the acceptor material under vacuum conditions (base pressure$\gg 10^{-7}$mbar), BCP (0.5 nm/min) as the blocking layer and aluminum as the top electrode. The deposition of ZnPc (twice sublimed) was also carried out in the vacuum before C60 evaporation. Device characterization was carried out under AM1.5G at 56 mW/cm^2 illumination in ambient condition with a Keithley 2600 SourceMeter$^{@}$ without encapsulation. Morphological investigations were performed using a Bruker multimode-8 atomic force microscope (AFM). Photoemission experiments were carried out *in house* using the HeI excitation (21.22 eV) of a He discharge lamp and a PECS Phoibos 100 hemispherical energy analyzer (base pressure 5x10 $^{-10}$ mbar). Sample transfer between the preparation and analysis chamber was done without breaking the vacuum investigating the undoped and doped polymer /C_{60} heterojunction.

Chapter 5

Summary and outlook

The key role of interface properties including morphology and energetics in OPVCs has been recognized for some time. However, the mechanism of OPVCs is still not fully understood and their abundant organic material species make them even more complicated and difficult to comprehend.

This thesis has focused on investigating the influence of the donor/acceptor interface on the performance of OPVCs. The interface area, which plays a crucial role for exciton dissociation, is increased effectively by incorporating nanocolumn structure in OPVCs, with the enlarged interface area subsequently producing an increase in J_{sc}. Owing to the introduction of the vertical donor/acceptor interface with the nanocolumn structure, the influence of the low exciton dissociation efficiency caused by short diffusion lengths in organic materials is reduced while using a thick absorber film. When a thick film is used, the light absorption can be reasonably enhanced. In addition, the light absorption enhancement in OPVCs can also result from the improved absorption features, which is caused by a change in the molecular orientation such as nanocolumn structured DIP grown by GLAD. Tuning the interface energy level alignment is achieved through molecular doping. This doping leads to a change of Gaussian density of states and further energetic disorder causing a variation in the conductivity and leading to energy level shifts. Moreover, stable and controllable doping can lead to the formation of net dipoles at the donor/acceptor interface, which also contribute to the photovoltaic gap enlargement and subsequently increasing the V_{oc} of OPVCs.

Within this thesis, the interface properties as a function of structure, morphology and electronics in OPVCs have been studied. Firstly pentacene and DIP, acting as an electron donor in OPVCs, were used to produce nanostructure with GLAD (sections 4.1 and 4.2). Pentacene grows preferentially layer-by-layer leading to a weak shadow effect. Therefore the nanocolumn structure can be only formed on a rough surface such as ITO. In comparison to pentacene, DIP grows preferentially in island-mode, accelerating the shadow effect in GLAD, which allows for the fabrication of DIP nanostructure on a smooth surface as shown in section 4.2. The interdigitated donor/acceptor heterojunction was formed by depositing molecular acceptor in vacuum or spin-coating polymer acceptor from solution on top of columnar structure. For pentacene nanocolumn arrays based OPVCs, the short circuit issue can be easily solved by introducing BCP as a buffer layer which leads to high density of nanocolumn arrays on the ITO substrate. However, for the OPVCs with DIP columnar structure on ITO, unavoidable current short passes induced by the low-density nanocolumn distribution rendered all devices beyond functional use. Fortunately, this problem can be excluded by employing PEDOT:PSS prior to depositing DIP. In the meantime, the low-density columnar

structure allows for the successful deposition of the acceptor in vacuum to form a perfectly infiltrated heterojunction. Furthermore, using GLAD, DIP grows in a “3D” powder-like crystalline structure, which enhanced its light absorption in OPVCs.

The short circuit current of OPVCs was increased due to the enlarged donor/acceptor interface area and the enhanced light absorption which can explained as follows. The vertically aligned donor/acceptor interfaces compensate for the issue of low exciton dissociation efficiency induced by short exciton diffusion lengths while employing a thick active absorption organic layer. The improvement is also based on a reduction of detrimental impacts of the optical interference effect and can be a subject of optics simulation in interdigitated nanostructure OPVCs. This may provide quantitative support for understanding the nanostructure functionality. In any case, the application of an interdigitated heterojunction is helpful towards solving the conflict between using thick organic absorber films and obtaining effective dissociation efficiency which requires absorber thickness closed to the excitons diffusion length in absorbers. The successful application of nanostructure in OPVCs demonstrates targeted optimization by GLAD, and thus offers promising perspectives for pushing further the limits of OPVCs in future applications.

In the third section of the main results chapter (section 4.3), doping effects on the performance of OPVCs have been addressed. *P*-type doping polyfuran film with F4-TCNQ was used as an electron donor, as well as a hole transport layer, in OPVCs. The observation of an improved J_{sc} for OPVCs based on polyfuran with low doping ratio can be explained by the conductivity increase due to the ionic F4-TCNQ as shown in the absorption spectra. The open circuit voltage of OPVCs employing a high doping ratio was increased significantly by the enlarged photovoltaic gap. This observation satisfied expectations with regards to the tuning of the energy level in organic electronic devices. However, based on the results of UPS measurements, the E_{pvg} enlargement was due to the introduced net dipoles, but not directly associated with the doping. The increase in E_{pvg} was inferred that the donor/acceptor interface dipoles arising from a random distributed pristine F4-TCNQ network was due to over doping. The functionality of doping was realized by increasing the conductivity to reach the charge carrier mobility balance for donor/acceptor heterojunction, such as eliminating the S-shape of J-V curve. Nevertheless, this study outlined the necessity for a detailed knowledge of the energetics of OPVCs since the E_{pvg} can be directly determined by the energy level offset between donor HOMO and acceptor LUMO. Although the OPVCs performance did not match expectations, the study still demonstrated that doping organic semiconductor could be a promising method towards augmenting the functionality of organic electronic devices provided in the future a detailed understanding of the molecular doping mechanism is formulated.

There are a number of unsolved issues that have arisen during this work that motivate future exploration. For instance, it would be interesting to investigate the impact of nanostructure on OPVCs quantum efficiency and design an accurate optical system to quantitatively analyze the advantages of organic nanostructure for light absorption and charge separation. Graphene is a promising candidate to replace ITO as the electrode, forming the

basis of an interesting research endeavor. As a material, graphene is not only light-weight but also transparent, renewable and its use leads to a decrease in pollutant output. In addition, graphene also has the potential to change molecular orientation as observed for lying DIP, which allows for the enhancement of the materials light absorption for OPVCs. If the conductivity of graphene is reduced to less than 100 Ω/square, it may be perfect substitutive electrode for organic optoelectronics. Moreover, the doping behavior and its application in organic electronic devices are also very promising directions for future work. In general, the organic doping process is very complicated. In this work, the short current density of OPVCs was severely affected by high doping concentrations due to the morphology interruption. This leads to PCE that was not significantly improved with a doubled open circuit voltage. Therefore, a better control of the doping process is necessary to eliminate the morphological issues and improve the doping efficiency.

Acknowledgements

I spent more than five years of my life in Berlin and this is the longest time I live in one city except my hometown. I experience many things, and those will be my cherishing remembrance.

Here, I would like to thank all people who make this work possible and appreciate their help both in my work and life. Foremost, I want to express sincere gratitude to my supervisor Prof. Dr. Norbert Koch for providing me the great opportunity to pursue my study in the Department of Physics at Humboldt Universtät zu Berlin. He is always pleased and patient to guide me through my research, sharing his overwhelming knowledge with me. Considering my research interests in photovoltaic cells, he provided me the opportunity to study OPVCs, focusing on the influence of interface characteristics on OPVCs performance.

I want to specially thank Johannes Frisch who offers me a lot of help in work with many valuable suggestions in experimental, in particular, he helped me start my life in Berlin, getting everything in life easy for me. The same appreciation goes to Junming Li and Dr. Haibo Wang, who share countless time in labs and office with me. I wouldn't survive without their care after my surgery. I also want to thank Dr. Ingo Saltzmann, Dr. Andreas Opitz, Raphael Schlesinger for fruitful discussion of experiment results, all manuscripts reading and valuable suggestions. Furthermore, all XRD results in this work were measured and analyzed by Dr. Ingo Saltzmann who also introduced me experiment setups in the beginning of my study. I want to thank Dr. Georg Heimel for theoretical discussion in fundamentals and the translation of abstract to German, thank Dr. Jian Zhang for introducing the GLAD and thank Hua Liang for introduction of AFM. I also would like to thank Prof. Dr. Jürgen P. Rabe for allowing me to access to the experimental facilities in his laboratories.

UPS experiments were carried out by Johannes Frisch and Dr. Patrick Amsalem. I want to thank Johannes Frisch for valuable discussion about the energy level alignment of molecular doping in OPVCs, thank Dr. Patrick Amsalem and Dr. Martin Oehzelt for valuable discussion about the energy level alignment of OPVCs and SEM measurements shown in this work are mainly done with Dr. Peter Schäfer at Institut für Physik and Carola Klimm at Helmhotz-Zentrum Berlin für Materialien und Energies GmbH. I also want to thank Dr. Melanie Timpel for valuable suggestions of SEM measurement.

I thank Henriette Strahl for all things she helped me especially about my visa extension and taking me to hospital when I got really sick. Thank Paul Zybarth and Timo Florian for experimental setups maintenance. Thank Poblenz Evi for safety introduction of chemical lab. Thank Dr. Mauro Castellani who shared the office for helping fix GLAD system.

I also would like to thank all people I spent time together in labs, offices and coffee room, Benjamin Bröker, Jens Niederhausen, Giovanni Ligorio, Stefanie Winkler, Andreas Wilke, Henry Mendez, Christo Christodoulou, Navid Abedi Khaledi, Hendrik Glowatyki, Philipp Herrmann, Sven Käbisch and Marco Nardi. In addition, I want to thank all my friends who share happy life in Berlin, Pei Zhao, Anyi Wang, Zhilin Yu, Gang Feng, Jianwen Liu, Yide He, Yan Qiao and Yuan Zhang.

Last but not least, I want to thank my beloved wife Li Liu for her love, care and support. I also thank my parents for trust, respect and endless support. A big thank you goes to my parents in law for their care and understanding. At the end, I want to dedicate this thesis to my grandfather who passed away one year ago.

Bibliography

[Abelmann, 1997a] ABELMANN, L. & LODDER, C. 1997a, Oblique evaporation and surface diffusion. *Thin Solid Films,* 305**,** 1-21.

[Abelmann, 1997b] ABELMANN, L. & LODDER, C. 1997b, Oblique evaporation and surface diffusion. *Thin Solid Films,* 305**,** 1-21.

[Adam, 1994] ADAM, D., SCHUHMACHER, P., SIMMERER, J., HAUSSLING, L., SIEMENSMEYER, K., ETZBACHI, K. H., RINGSDORF, H. & HAARER, D. 1994, Fast photoconduction in the highly ordered columnar phase of a discotic liquid crystal. *Nature Mater.,* 371.

[Ahn, 2007] AHN, T.-S., WRIGHT, N. & BARDEEN, C. J. 2007, The effects of orientational and energetic disorder on Forster energy migration along a one-dimensional lattice. *Chemical Physics Letters,* 446**,** 43-48.

[Akaike, 2008] AKAIKE, K., KANAI, K., YOSHIDA, H., TSUTSUMI, J., NISHI, T., SATO, N., OUCHI, Y. & SEKI, K. 2008, Ultraviolet photoelectron spectroscopy and inverse photoemission spectroscopy of 6,6 -phenyl-C-61-butyric acid methyl ester in gas and solid phases. *Journal of Applied Physics,* 104**,** 5.

[Akamatu, 1954] AKAMATU, H., INOKUCHI, H. & MATSUNAGA, Y. 1954, Electrical conductivity of the perylene-bromine complex. *Nature,* 173**,** 168-169.

[Amsalem, 2009] AMSALEM, P., GIOVANELLI, L., THEMLIN, J. M. & ANGOT, T. 2009, Electronic and vibrational properties at the ZnPc/Ag(110) interface. *Physical Review B,* 79**,** 10.

[Anthony, 2010] ANTHONY, J. E., FACCHETTI, A., HEENEY, M., MARDER, S. R. & ZHAN, X. 2010, n-Type Organic Semiconductors in Organic Electronics. *Advanced Materials,* 22**,** 3876-3892.

[Arkhipov, 2004] ARKHIPOV, V. I. & BÄSSLER, H. 2004, Exciton dissociation and charge photogeneration in pristine and doped conjugated polymers. *physica status solidi (a),* 201**,** 1152-1187.

[Arkhipov, 2005a] ARKHIPOV, V. I., EMELIANOVA, E. V., HEREMANS, P. & BÄSSLER, H. 2005a, Analytic model of carrier mobility in doped disordered organic semiconductors. *Physical Review B,* 72**,** 235202.

[Arkhipov, 2005b] ARKHIPOV, V. I., HEREMANS, P., EMELIANOVA, E. V. & BÄSSLER, H. 2005b, Effect of doping on the density-of-states distribution and carrier hopping in disordered organic semiconductors. *Physical Review B,* 71**,** 045214.

[Atkins, 2006] ATKINS, P. & PAULA, J. D. 2006. *Physical Chemistry,* New York, Oxford University Press.

[Aziz, 2007] AZIZ, E. E., VOLLMER, A., EISEBITT, S., EBERHARDT, W., PINGEL, P., NEHER, D. & KOCH, N. 2007, Localized charge transfer in a molecularly doped conducting polymer. *Advanced Materials,* 19**,** 3257-+.

[Bailey-Salzman, 2007] BAILEY-SALZMAN, R. F., RAND, B. P. & FORREST, S. R. 2007, Near-infrared sensitive small molecule organic photovoltaic cells based on chloroaluminum phthalocyanine. *Appl. Phys. Lett.,* 91**,** 013508.

[Balsara, 1996] BALSARA, N. P., LIN, C. & HAMMOUDA, B. 1996, Early stages of nucleation and growth in a polymer blend. *Phys. Rev. Lett.,* 77**,** 3847-3850.

[Barabási, 1995] BARABÁSI, A. L. & STANLEY, H. E. 1995. *Fractal concepts in surface growth*, Cambridge

University Press.

[Barry P. Rand and Diana P. Burk, 2007] BARRY P. RAND AND DIANA P. BURK, S. R. F. 2007, Offset energies at organic semicondutor heterojunction and their influence on the open-circuit voltage of thin-film solar cells. *Physical Review B,* 75.

[Barth, 1997] BARTH, S., HERTEL, D., TAK, Y. H., BÄSSLER, H. & HÖRHOLD, H. H. 1997, Geminate pair dissociation in random organic systems. *Chem. Phys. Lett.,* 274**,** 165-170.

[Bässler, 1993] BÄSSLER, H. 1993, Charge transport in disordered organic photoconductors a monte carlo simulation study. *physica status solidi (b),* 175**,** 15-56.

[Bassler, 2012] BASSLER, H. & KOHLER, A. 2012, Charge transport in organic semiconductors. *Top Curr. Chem.,* 312**,** 1-65.

[Bauer, 1998] BAUER, K. H. 1998. *Coated pharmaceutical dosage forms: fundamentals, manufacturing techniques, biopharmaceutical aspects, test methods, and raw materials*, CRC Press.

[Bijleveld, 2010] BIJLEVELD, J. C., VERSTRIJDEN, R. A. M., WIENK, M. M. & JANSSEN, R. A. J. 2010, Maximizing the open-circuit voltage of polymer: Fullerene solar cells. *Applied Physics Letters,* 97**,** 073304.

[Binnig, 1986] BINNIG, G., QUATE, C. F. & GERBER, C. 1986, Atomic force microscope. *Phys. Rev. Lett.,* 56**,** 930-933.

[Blochwitz, 1998] BLOCHWITZ, J., PFEIFFER, M., FRITZ, T. & LEO, K. 1998, Low voltage organic light emitting diodes featuring doped phthalocyanine as hole transport material. *Appl. Phys. Lett.,* 73**,** 729-731.

[Bornside, 1987] BORNSIDE, D. E., MACOSKO, C. W. & SCRIVEN, L. E. 1987, On the modeling of spin coating. *Journal of Imaging Technology,* 13**,** 122-130.

[Brabec, 2003] BRABEC, C. J., DYAKONOV, V., J., P. & SARICIFTCI, N. S. 2003. *Organic photovoltaics*, Springer.

[Braun, 1984] BRAUN, C. L. 1984, Electric field assisted dissociation of charge transfer states as a mechanism of photocarrier production. *The Journal of Chemical Physics,* 80**,** 4157-4161.

[Braun, 2009] BRAUN, S., SALANECK, W. R. & FAHLMAN, M. 2009, Energy-level alignment at organic/metal and organic/organic interfaces. *Advanced Materials,* 21**,** 1450-1472.

[Breton, 1999] BRETON, P. J. 1999, From microns to nanometers: Early landmarks in the science of scanning electron microscope imaging. *Scanning Microscopy International,* 13**,** 6.

[Bröker, 2010] BRÖKER, B., HOFMANN, O. T., RANGGER, G. M., FRANK, P., BLUM, R. P., RIEGER, R., VENEMA, L., VOLLMER, A., MÜLLEN, K., RABE, J. P., WINKLER, A., RUDOLF, P., ZOJER, E. & KOCH, N. 2010, Density-dependent reorientation and rehybridization of chemisorbed conjugated molecules for controlling interface electronic structure. *Physical Review Letters,* 104**,** 246805.

[Brutting, 2012] BRUTTING, W., ADACHI, C. & HOLMES, R. J. 2012. *Physics of organic semiconductors,* Weinheim, Germany, Wiley-VCH Verlag&Co. KGaA.

[Bube, 1981] BUBE, R. H. & FAHRENBRUCH, A. L. 1981, Photovoltaic effect. *Advances in Electronics and Physics,* 56**,** 163-217.

[Bundgaard, 2007] BUNDGAARD, E. & KREBS, F. C. 2007, Low band gap polymers for organic photovoltaics. *Solar Energy Materials and Solar Cells,* 91**,** 954-985.

[Cahn, 1958] CAHN, J. W. & HILLIARD, J. E. 1958, Free energy of a nonuniform system. 1. Interfacial

free energy. *J. Chem. phys.,* 28**,** 258-267.

[Cappella, 1999] CAPPELLA, B. & DIETLER, G. 1999, Force-distance curves by atomic force microscopy. *Surface Science Reports,* 34**,** 1-104.

[Cetinkaya, 2008] CETINKAYA, M., MALVADKAR, N. & DEMIREL, M. C. 2008, Power-law scaling of structured poly(p-xylylene) deposited by oblique angle. *Journal of Polymer Science Part B-Polymer Physics,* 46**,** 640-648.

[Chan, 2006] CHAN, M. Y., LEE, C. S., LAI, S. L., FUNG, M. K., WONG, F. L., SUN, H. Y., LAU, K. M. & LEE, S. T. 2006, Efficient organic photovoltaic devices using a combination of exciton blocking layer and anodic buffer layer. *Journal of Applied Physics,* 100**,** 4.

[Chang, 2004] CHANG, P. C., LEE, J., HUANG, D., SUBRAMANIAN, V., MURPHY, A. R. & FRÉCHET, J. M. J. 2004, Film morphology and thin film transistor performance of solution-processed oligothiophenes. *Chemistry of Materials,* 16**,** 4783-4789.

[Coropceanu, 2007a] COROPCEANU, V., CORNIL, J., DA SILVA, D. A., OLIVIER, Y., SILBEY, R. & BREDAS, J. L. 2007a, Charge transport in organic semiconductors (vol 107, pg 926, 2007). *Chemical Reviews,* 107**,** 2165-2165.

[Coropceanu, 2007b] COROPCEANU, V., CORNIL, J., DA SILVA FILHO, D. A., OLIVIER, Y., SILBEY, R. & BRÉDAS, J.-L. 2007b, Charge transport in organic semiconductors. *Chemical Reviews,* 107**,** 926-952.

[de Boer, 2004] DE BOER, R. W. I., GERSHENSON, M. E., MORPURGO, A. F. & PODZOROV, V. 2004, Organic single-crystal field-effect transistors. *physica status solidi (a),* 201**,** 1302-1331.

[De Renzi, 2005] DE RENZI, V., ROUSSEAU, R., MARCHETTO, D., BIAGI, R., SCANDOLO, S. & DEL PENNINO, U. 2005, Metal work-function changes induced by organic adsorbates: A combined experimental and theoretical study. *Physical Review Letters,* 95**,** 046804.

[Deibel, 2009] DEIBEL, C., STROBEL, T. & DYAKONOV, V. 2009, Origin of the efficient polaron-pair dissociation in polymer-fullerene blends. *Physical Review Letters,* 103**,** 036402.

[Deibel, 2010] DEIBEL, C., STROBEL, T. & DYAKONOV, V. 2010, Role of the charge transfer state in organic donor–acceptor solar cells. *Advanced Materials,* 22**,** 4097-4111.

[Deschler, 2011] DESCHLER, F., DA COMO, E., LIMMER, T., TAUTZ, R., GODDE, T., BAYER, M., VON HAUFF, E., YILMAZ, S., ALLARD, S., SCHERF, U. & FELDMANN, J. 2011, Reduced Charge Transfer Exciton Recombination in Organic Semiconductor Heterojunctions by Molecular Doping. *Physical Review Letters,* 107**,** 4.

[Destruel, 2006] DESTRUEL, P., BOCK, H., SÉGUY, I., JOLINAT, P., OUKACHMIH, M. & BEDEL-PEREIRA, E. 2006, Influence of indium tin oxide treatment using UV–ozone and argon plasma on the photovoltaic parameters of devices based on organic discotic materials. *Polymer International,* 55**,** 601-607.

[Dexter, 1953] DEXTER, D. L. 1953, A theory of sensitized luminescence in solids. *J. Chem. phys.,* 21**,** 836-850.

[Dieckmann, 1993] DIECKMANN, A., BÄSSLER, H. & BORSENBERGER, P. M. 1993, An assessment of the role of dipoles on the density-of-states function of disordered molecular solids. *J. Chem. phys.,* 99**,** 8136.

[Dirks, 1977] DIRKS, A. G. & LEAMY, H. J. 1977, Columnar microstructure in vapor-deposited thin films. *Thin Solid Films,* 47**,** 219-233.

[Dixon, 1989] DIXON, D. A., CALABRESE, J. C. & MILLER, J. S. 1989, Crystall and molecular-structure of the 2-1 charge-transfer salt of decamethylferrocene and perfluoro-7,7,8,8-tetracyano-p-quinodimethane: { $[Fe(C_5Me_5)_2^+]\}_2$ $[TCNQF_4]^{2-}$ electric structure of $[TCNQF_4]^N$ (N = 0, 1-, 2-). *J. Chem. phys.,* 93**,** 2284-2291.

[Dou, 2013] DOU, L., YOU, J., HONG, Z., XU, Z., LI, G., STREET, R. A. & YANG, Y. 2013, 25th anniversary article: a decade of organic/polymeric photovoltaic research. *Adv. Mater.,* 25**,** 6642-71.

[Drury, 1998] DRURY, C. J., MUTSAERS, C. M. J., HART, C. M., MATTERS, M. & DE LEEUW, D. M. 1998, Low-cost all-polymer integrated circuits. *Appl. Phys. Lett.,* 73**,** 108-110.

[Dunlap, 1996] DUNLAP, D. H., PARRIS, P. E. & KENKRE, V. M. 1996, Charge-dipole model for the universal field dependence of mobilities in molecularly doped polymers. *Phys. Rev. Lett.,* 77**,** 542-545.

[Duong, 2013] DUONG, D. T., WANG, C., ANTONO, E., TONEY, M. F. & SALLEO, A. 2013, The chemical and structural origin of efficient p-type doping in P3HT. *Organic Electronics,* 14**,** 1330-1336.

[Dürr, 2003] DÜRR, A. C., KOCH, N., KELSCH, M., RÜHM, A., GHIJSEN, J., JOHNSON, R. L., PIREAUX, J. J., SCHWARTZ, J., SCHREIBER, F., DOSCH, H. & KAHN, A. 2003, Interplay between morphology, structure, and electronic properties at diindenoperylene-gold interfaces. *Phys. Rev. B,* 68**,** 115428.

[Dürr, 2002] DÜRR, A. C., SCHREIBER, F., MÜNCH, M., KARL, N., KRAUSE, B., KRUPPA, V. & DOSCH, H. 2002, High structural order in thin films of the organic semiconductor diindenoperylene. *Applied Physics Letters,* 81**,** 2276.

[E. Meyer, 2003] E. MEYER, H. J. HUG & BENNEWITZ, R. 2003. *Scanning probe microscopy. The lab on a tip.,* Heidelberg, Springer, Berlin.

[Emin, 1975] EMIN, D. 1975, Phonon-assited transition rates. 1. Optical-phonon-assisted hopping in solids. *Adv. Phys.,* 24**,** 305-348.

[Emslie, 1958] EMSLIE, A. G., BONNER, F. T. & PECK, L. G. 1958, Flow of a viscous liquid on a rotating disk. *J. Appl. Phys.,* 29**,** 858-862.

[Fahlman, 2007] FAHLMAN, M., CRISPIN, A., CRISPIN, X., HENZE, S. K. M., JONG, M. P. D., OSIKOWICZ, W., TENGSTEDT, C. & SALANECK, W. R. 2007, Electronic structure of hybrid interfaces for polymer-based electronics. *Journal of Physics: Condensed Matter,* 19**,** 183202.

[Felton, 2013] FELTON, L. A. 2013, Mechanisms of polymeric film formation. *International Journal of Pharmaceutics,* 457**,** 423-427.

[Feron, 2012] FERON, K., BELCHER, W., FELL, C. & DASTOOR, P. 2012, Organic solar cells: Understanding the role of Förster resonance energy transfer. *International Journal of Molecular Sciences,* 13**,** 17019-17047.

[Ferron, 2012] FERRON, C. C., DELGADO, M. C. R., GIDRON, O., SHARMA, S., SHEBERLA, D., SHEYNIN, Y., BENDIKOV, M., NAVARRETE, J. T. L. & HERNANDEZ, V. 2012, α-Oligofurans show a sizeable extent of π-conjugation as probed by Raman spectroscopy. *Chem. Commun.,* 48**,** 6732-6734.

[Fischer, 2006] FISCHER, M., DRESSEL, M., GOMPF, B., TRIPATHI, A. K. & PFLAUM, J. 2006, Infrared spectroscopy on the charge accumulation layer in rubrene single crystals. *Applied Physics Letters,* 89**,** -.

[Flack, 1984] FLACK, W. W., SOONG, D. S., BELL, A. T. & HESS, D. W. 1984, A mathematical model for spin coating of polymer resists. *J. Appl. Phys.,* 56**,** 1199-1206.

[Foertig, 2009] FOERTIG, A., BAUMANN, A., RAUH, D., DYAKONOV, V. & DEIBEL, C. 2009, Charge carrier concentration and temperature dependent recombination in polymer-fullerene solar cells. *Applied Physics Letters,* 95**,** -.

[Forrest, 1997] FORREST, S. R. 1997, Ultrathin organic films grown by organic molecular beam deposition and related techniques. *Chem. Rev.,* 97**,** 1793-1896.

[Förster, 1959] FÖRSTER, T. 1959, Transfer mechanisms of electronic excitation. *Discuss. Faraday Soc.,* 27**,** 7-17.

[Francombe, 1964] FRANCOMBE, M. H. & SATO, H. 1964. *Single crystal films,* Pergamon, Oxford.

[Frankevich, 1992] FRANKEVICH, E. L., LYMAREV, A. A., SOKOLIK, I., KARASZ, F. E., BLUMSTENGEL, S., BAUGHMAN, R. H. & HÖRHOLD, H. H. 1992, Polaron-pair generation in poly(phenylene vinylenes). *Phys. Rev. B,* 46**,** 9320-9324.

[Fratini, 2009] FRATINI, S. & CIUCHI, S. 2009, Bandlike motion and mobility saturation in organic molecular semiconductors. *Physical Review Letters,* 103**,** 266601.

[Fredrik A. Lindholm, 1979] FREDRIK A. LINDHOLM, J. G. F., EDWARD L. BURGESS 1979, Application of the Supperposition Principle to Solar-Cell Analysis. *IEEE Transaction on Electron Devices,* ED-26.

[Frisch, 2011] FRISCH, J., VOLLMER, A., RABE, J. P. & KOCH, N. 2011, Ultrathin polythiophene films on an intrinsically conducting polymer electrode: Charge transfer induced valence states and interface dipoles. *Organic Electronics,* 12**,** 916-922.

[Gao, 2001] GAO, W. & KAHN, A. 2001, Controlled p-doping of zinc phthalocyanine by coevaporation with tetrafluorotetracyanoquinodimethane: A direct and inverse photoemission study. *Applied Physics Letters,* 79**,** 4040.

[Gao, 2002] GAO, W. & KAHN, A. 2002, Electronic structure and current injection in zinc phthalocyanine doped with tetrafluorotetracyanoquinodimethane: Interface versus bulk effects. *Organic Electronics,* 3**,** 53-63.

[Gao, 2003] GAO, W. & KAHN, A. 2003, Controlled p doping of the hole-transport molecular material N,N′-diphenyl-N,N′-bis(1-naphthyl)-1,1′-biphenyl-4,4′-diamine with tetrafluorotetracyanoquinodimethane. *Journal of Applied Physics,* 94**,** 359.

[Geiser, 2008] GEISER, A., FAN, B., BENMANSOUR, H., CASTRO, F., HEIER, J., KELLER, B., MAYERHOFER, K. E., NUESCH, F. & HANY, R. 2008, Poly(3-hexylthiophene)/C-60 heterojunction solar cells: Implication of morphology on performance and ambipolar charge collection. *Solar Energy Materials and Solar Cells,* 92**,** 464-473.

[Geoghegan, 2003] GEOGHEGAN, M. & KRAUSCH, G. 2003, Wetting at polymer surfaces and interfaces. *Progress in Polymer Science,* 28**,** 261-302.

[Ghosh, 1973] GHOSH, A. K. & FENG, T. 1973, Rectification, space-charge-limited current, photovoltaic and photoconductive properties of Al ／ tetracene ／ Au sandwich cell. *J. Appl. Phys.,* 44**,** 2781.

[Glaeser, 1966a] GLAESER, R. M. & BERRY, R. S. 1966a, MOBILITIES OF ELECTRONS AND HOLES IN ORGANIC MOLECULAR SOLIDS . COMPARISON OF BAND AND HOPPING MODELS. *J. Chem. phys.,* 44**,** 3797-&.

[Glaeser, 1966b] GLAESER, R. M. & BERRY, R. S. 1966b, Mobilities of electrons and holes in organic molecular solids. comparison of band and hopping models. *J. Chem. phys.,* 44**,** 3797-3810.

[Glowatzki, 2007] GLOWATZKI, H., DUHM, S., BRAUN, K. F., RABE, J. P. & KOCH, N. 2007, Molecular

chains and carpets of sexithiophenes on Au(111). *Physical Review B,* 76**,** 125425.

[Gok, 2005] GOK, A., CAN, H. K., SARI, B. & TALU, M. 2005, X-ray diffraction studies and DC electrical conductivity of poly(2-halogenanilines) and their composites with polyfuran. *Materials Letters,* 59**,** 80-84.

[Goldstein, 2003] GOLDSTEIN, J., NEWBURY, D. E., JOY, D. C., LYMAN, C. E., ECHLIN, P., LIFSHIN, E., SAWYER, L. & MICHAEL, J. R. 2003. *Scanning electron microscopy and X-ray microanalysis,* New York, Plenum Press.

[Gommans, 2008] GOMMANS, H., VERREET, B., RAND, B. P., MULLER, R., POORTMANS, J., HEREMANS, P. & GENOE, J. 2008, On the role of bathocuproine in organic photovoltaic cells. *Adv. Funct. Mater.,* 18**,** 3686-3691.

[González-Tejera, 2008] GONZÁLEZ-TEJERA, M. J., DE LA BLANCA, E. S. & CARRILLO, I. 2008, Polyfuran conducting polymers: Synthesis, properties, and applications. *Synthetic Metals,* 158**,** 165-189.

[Greczynski, 1999] GRECZYNSKI, G., KUGLER, T. & SALANECK, W. R. 1999, Characterization of the PEDOT-PSS system by means of X-ray and ultraviolet photoelectron spectroscopy. *Thin Solid Films,* 354**,** 129-135.

[Green, 2013] GREEN, M. A., EMERY, K., HISHIKAWA, Y., WARTA, W. & DUNLOP, E. D. 2013, Solar cell efficiency tables (version 41). *Progress in Photovoltaics: Research and Applications,* 21**,** 1-11.

[Green, 2014] GREEN, M. A., EMERY, K., HISHIKAWA, Y., WARTA, W. & DUNLOP, E. D. 2014, Solar cell efficiency tables (version 44). *Progress in Photovoltaics,* 22**,** 701-710.

[Groenendaal, 2000] GROENENDAAL, L., JONAS, F., FREITAG, D., PIELARTZIK, H. & REYNOLDS, J. R. 2000, Poly(3,4-ethylenedioxythiophene) and its derivatives: past, present, and future. *Adv. Mater.,* 12**,** 481-494.

[Gruber, 2013] GRUBER, M., RAWOLLE, M., WAGNER, J., MAGERL, D., HÖRMANN, U., PERLICH, J., ROTH, S. V., OPITZ, A., SCHREIBER, F., MÜLLER-BUSCHBAUM, P. & BRÜTTING, W. 2013, Correlating structure and morphology to device performance of molecular organic donor-acceptor photovoltaic cells based on diindenoperylene (DIP) and C60. *Adv. Energy Mater.,* 3**,** 1075-1083.

[Gruber, 2012] GRUBER, M., WAGNER, J., KLEIN, K., HÖRMANN, U., OPITZ, A., STUTZMANN, M. & BRÜTTING, W. 2012, Thermodynamic efficiency limit of molecular donor-acceptor solar cells and its application to diindenoperylene/C60-based planar heterojunction devices. *Adv. Energy Mater.,* 2**,** 1100-1108.

[Hagemeyer, 1993] HAGEMEYER, A., RICHTER, H. J., HIBST, H., MAIER, V. & MAROSI, L. 1993, Crystallographic texture and morphology of obliquely deposited co-cr magnetic thin-films on flexible polymeric sunbstrates. *Thin Solid Films,* 230**,** 199-202.

[Halik, 2002] HALIK, M., KLAUK, H., ZSCHIESCHANG, U., KRIEM, T., SCHMID, G., RADLIK, W. & WUSSOW, K. 2002, Fully patterned all-organic thin film transistors. *Applied Physics Letters,* 81**,** 289-291.

[Halls, 1995] HALLS, J. J. M., WALSH, C. A., GREENHAM, N. C., MARSEGLIA, E. A., FRIEND, R. H., MORATTI, S. C. & HOLMES, A. B. 1995, Efficient photodiodes from interpenetrating polymer networks. *Nature,* 376.

[Hannewald, 2004] HANNEWALD, K., STOJANOVIĆ, V. M., SCHELLEKENS, J. M. T., BOBBERT, P. A., KRESSE, G. & HAFNER, J. 2004, Theory of polaron bandwidth narrowing in organic molecular crystals. *Physical Review B,* 69**,** 075211.

[Hashimoto, 1982] HASHIMOTO, T., OKAMOTO, K., HARA, K., KAMIYA, M. & FUJIWARA, H. 1982, Columnar structure and texture of iorn films evaporated at oblique-incidence. *Thin Solid Films,* 91**,** 145-154.

[He, 2007] HE, F., TIAN, L. L., TIAN, X. Y., XU, H., WANG, Y. H., XIE, W. J., HANIF, M., XIA, J. L., SHEN, F. Z., YANG, B., LI, F., MA, Y. G., YANG, Y. Q. & SHEN, J. C. 2007, Diphenylamine-Substituted Cruciform Oligo(phenylene vinylene): Enhanced One- and Two-Photon Excited Fluorescence in the Solid State. *Advanced Functional Materials,* 17**,** 1551-1557.

[Heimel, 2012] HEIMEL, G., SALZMANN, I. & KOCH, N. 2012, On the fundamental processes in molecular electrical doping of organic semiconductors. *Theory and Applications in Computational Chemistry: The First Decade of the Second Millennium,* 1456**,** 148-156.

[Heinemeyer, 2008a] HEINEMEYER, U., SCHOLZ, R., GISSLÉN, L., ALONSO, M., OSSÓ, J., GARRIGA, M., HINDERHOFER, A., KYTKA, M., KOWARIK, S., GERLACH, A. & SCHREIBER, F. 2008a, Exciton-phonon coupling in diindenoperylene thin films. *Phys. Rev. B,* 78.

[Heinemeyer, 2008b] HEINEMEYER, U., SCHOLZ, R., GISSLÉN, L., ALONSO, M. I., OSSÓ, J. O., GARRIGA, M., HINDERHOFER, A., KYTKA, M., KOWARIK, S., GERLACH, A. & SCHREIBER, F. 2008b, Exciton-phonon coupling in diindenoperylene thin films. *Phys. Rev. B,* 78**,** 085210.

[Heinrich, 2007] HEINRICH, M. A., PFLAUM, J., TRIPATHI, A. K., FREY, W., STEIGERWALD, M. L. & SIEGRIST, T. 2007, Enantiotropic polymorphism in diindenoperylene. *J. Phys. Chem. C,* 111**,** 18878-18881.

[Heringdorf, 2001] HERINGDORF, F., REUTER, M. C. & TROMP, R. M. 2001, Growth dynamics of pentacene thin films. *Nature,* 412**,** 517-520.

[Hinderhofer, 2012a] HINDERHOFER, A., GERLACH, A., BROCH, K., HOSOKAI, T., YONEZAWA, K., KATO, K., KERA, S., UENO, N. & SCHREIBER, F. 2012a, Geometric and electronic structure of templated C60 on diindenoperylene thin films. *J. Phys. Chem. C,* 117**,** 1053-1058.

[Hinderhofer, 2012b] HINDERHOFER, A., HOSOKAI, T., YONEZAWA, K., GERLACH, A., KATO, K., BROCH, K., FRANK, C., NOVAK, J., KERA, S., UENO, N. & SCHREIBER, F. 2012b, Post-growth surface smoothing of thin films of diindenoperylene. *Applied Physics Letters,* 101.

[Holstein, 1959a] HOLSTEIN, T. 1959a, Studies of polaron motion: Part I. The molecular-crystal model. *Annals of Physics,* 8**,** 325-342.

[Holstein, 1959b] HOLSTEIN, T. 1959b, Studies of polaron motion: Part II. The “small” polaron. *Annals of Physics,* 8**,** 343-389.

[Hong, 2007] HONG, Z. R., MAENNIG, B., LESSMANN, R., PFEIFFER, M., LEO, K. & SIMON, P. 2007, Improved efficiency of zinc phthalocyanine/C-60 based photovoltaic cells via nanoscale interface modification. *Applied Physics Letters,* 90**,** 3.

[Hörmann, 2011a] HÖRMANN, U., WAGNER, J., GRUBER, M., OPITZ, A. & BRÜTTING, W. 2011a, Approaching the ultimate open circuit voltage in thiophene based single junction solar cells by applying diindenoperylene as acceptor. *Phys. Status Solidi RRL,* 5**,** 241-243.

[Hörmann, 2011b] HÖRMANN, U., WAGNER, J., GRUBER, M., OPITZ, A. & BRÜTTING, W. 2011b, Approaching the ultimate open circuit voltage in thiophene based single junction solar cells by applying diindenoperylene as acceptor. *Phys. Stat. Sol. -R,* 5**,** 241-243.

[Hrudey, 2006a] HRUDEY, P. C. P., SZETO, B. & BRETT, M. J. 2006a, Strong circular Bragg phenomena in self-ordered porous helical nanorod arrays of Alq3. *Applied Physics Letters,* 88**,** 251106.

[Hrudey, 2006b] HRUDEY, P. C. P., WESTRA, K. L. & BRETT, M. J. 2006b, Highly ordered organic Alq3 chiral luminescent thin films fabricated by glancing-angle deposition. *Advanced Materials,* 18**,** 224-228.

[Hrudey, 2006c] HRUDEY, P. C. P., WESTRA, K. L. & BRETT, M. J. 2006c, Highly ordered organic Alq3 chiral luminescent thin films fabricated by glancing-angle deposition. *Adv. Mater.,* 18**,** 224-228.

[Huang, 2009] HUANG, Y. L., CHEN, W., HUANG, H., QI, D. C., CHEN, S., GAO, X. Y., PFLAUM, J. & WEE, A. T. S. 2009, Ultrathin films of diindenoperylene on graphite and SiO2. *The Journal of Physical Chemistry C,* 113**,** 9251-9255.

[Huckel, 1931] HUCKEL, E. 1931, Quantum contributions to the benzene problem. *Zeitschrift Fur Physik,* 72**,** 310-337.

[Hwang, 2009] HWANG, J., WAN, A. & KAHN, A. 2009, Energetics of metal-organic interfaces: New experiments and assessment of the field. *Materials Science & Engineering R-Reports,* 64**,** 1-31.

[Ibach, 2006] IBACH, H. 2006. *Physics of Surfaces and Interfaces,* Heidelberg, Germany, Springer-Verlag Berlin.

[Itaka, 2006] ITAKA, K., YAMASHIRO, M., YAMAGUCHI, J., HAEMORI, M., YAGINUMA, S., MATSUMOTO, Y., KONDO, M. & KOINUMA, H. 2006, High-mobility C60 field-effect transistors fabricated on molecular- wetting controlled substrates. *Advanced Materials,* 18**,** 1713-1716.

[Jenekhe, 1984] JENEKHE, S. A. 1984, Effects of solvent mass transfer on flow of polymer solutions on a flat rotating disk. *Industrial & Engineering Chemistry Fundamentals,* 23**,** 425-432.

[Jørgensen, 2008] JØRGENSEN, M., NORRMAN, K. & KREBS, F. C. 2008, Stability/degradation of polymer solar cells. *Sol. Energ. Mat. Sol. Cells,* 92**,** 686-714.

[Jukes, 2004] JUKES, P. C., MARTIN, S. J., HIGGINS, A. M., GEOGHEGAN, M., JONES, R. A. L., LANGRIDGE, S., WEHRUM, A. & KIRCHMEYER, S. 2004, Controlling the surface composition of poly(3,4-ethylene dioxythiophene)–poly(styrene sulfonate) blends by heat treatment. *Advanced Materials,* 16**,** 807-811.

[Jurchescu, 2004] JURCHESCU, O. D., BAAS, J. & PALSTRA, T. T. M. 2004, Effect of impurities on the mobility of single crystal pentacene. *Applied Physics Letters,* 84**,** 3061.

[Kahn, 2003a] KAHN, A., KOCH, N. & GAO, W. 2003a, Electronic structure and electrical properties of interfaces between metals and π-conjugated molecular films. *Journal of Polymer Science Part B: Polymer Physics,* 41**,** 2529-2548.

[Kahn, 2003b] KAHN, A., KOCH, N. & GAO, W. Y. 2003b, Electronic structure and electrical properties of interfaces between metals and pi-conjugated molecular films. *Journal of Polymer Science Part B-Polymer Physics,* 41**,** 2529-2548.

[Kakuta, 2007] KAKUTA, H., HIRAHARA, T., MATSUDA, I., NAGAO, T., HASEGAWA, S., UENO, N. & SAKAMOTO, K. 2007, Electronic Structures of the Highest Occupied Molecular Orbital Bands of a Pentacene Ultrathin Film. *Phys. Rev. Lett.,* 98.

[Kambersky, 1961] KAMBERSKY, V., MALEK, Z., ONDRIS, M. & FRAIT, Z. 1961, Dependence of uniaxial magnetic anisotropy in evaporated films on angle of incidence. *Czechoslovak Journal of Physics,* 11**,** 171.

[Kaminska, 2005] KAMINSKA, K., AMASSIAN, A., MARTINU, L. & ROBBIE, K. 2005, Growth of vacuum

evaporated ultraporous silicon studied with spectroscopic ellipsometry and scanning electron microscopy. *Journal of Applied Physics,* 97**,** 8.

[Karabacak, 2003] KARABACAK, T., SINGH, J. P., ZHAO, Y. P., WANG, G. C. & LU, T. M. 2003, Scaling during shadowing growth of isolated nanocolumns. *Physical Review B,* 68**,** 5.

[Kearns, 1960] KEARNS, D. R., TOLLIN, G. & CALVIN, M. 1960, Electrical properties of organic solids. II. effects of added electron acceptor on metal‐free phthalocyanine. *J. Chem. phys.,* 32**,** 1020-1025.

[Kerp, 1998] KERP, H. R., DONKER, H., KOEHORST, R. B. M., SCHAAFSMA, T. J. & VAN FAASSEN, E. E. 1998, Exciton transport in organic dye layers for photovoltaic applications. *Chem. Phys. Lett.,* 298.

[Kido, 1998] KIDO, J. & MATSUMOTO, T. 1998, Bright organic electroluminescent devices having a metal-doped electron-injecting layer. *Appl. Phys. Lett.,* 73**,** 2866-2868.

[Kietzke, 2006] KIETZKE, T., EGBE, D. A. M., HORHÖLD, H.-H. & NEHER, D. 2006, Comparative study of M3EH-PPV-based bilayer photovoltaic devices. *Macromolecules,* 39**,** 4018-4022.

[Kim, 2012] KIM, D. H., JEON, Y. P., LEE, S. H., LEE, D. U., KIM, T. W. & HAN, S. H. 2012, Enhancement of the power conversion efficiency for organic photovoltaic devices due to an embedded rugged nanostructural layer. *Organic Electronics,* 13**,** 1068-1072.

[Kirchmeyer, 2005] KIRCHMEYER, S. & REUTER, K. 2005, Scientific importance, properties and growing applications of poly(3,4-ethylenedioxythiophene). *Journal of Materials Chemistry,* 15**,** 2077-2088.

[Knorr, 1959] KNORR, T. & HOFFMAN, R. 1959, Dependence of geometric magnetic anisotropy in thin iron films. *Phys. Rev.,* 113**,** 1039-1046.

[Koch, 2007a] KOCH, N. 2007a, Organic electronic devices and their functional interfaces. *Chemphyschem : a Eur. J. Chem. Phys. & Phys. Chem.,* 8**,** 1438-55.

[Koch, 2005] KOCH, N., DUHM, S., RABE, J. P., VOLLMER, A. & JOHNSON, R. L. 2005, Optimized hole injection with strong electron acceptors at organic-metal interfaces. *Physical Review Letters,* 95**,** 237601.

[Koch, 2002] KOCH, N., GHIJSEN, J., JOHNSON, R. L., SCHWARTZ, J., PIREAUX, J. J. & KAHN, A. 2002, Physisorption-like Interaction at the Interfaces Formed by Pentacene and Samarium. *The Journal of Physical Chemistry B,* 106**,** 4192-4196.

[Koch, 2003] KOCH, N., KAHN, A., GHIJSEN, J., PIREAUX, J.-J., SCHWARTZ, J., JOHNSON, R. L. & ELSCHNER, A. 2003, Conjugated organic molecules on metal versus polymer electrodes: Demonstration of a key energy level alignment mechanism. *Applied Physics Letters,* 82**,** 70-72.

[Koch, 2000] KOCH, N., PAIRLEITNER, R., LE, Q. T., FORSYTHE, E. W., GAO, Y. & LEISING, G. 2000, Photoemission spectroscopic investigation on the interface formation of a ladder-type poly(para-phenylene) with aluminum. *Appl. Phys. Lett.,* 76**,** 3738-3740.

[Koch, 2007b] KOCH, N., VOLLMER, A., DUHM, S., SAKAMOTO, Y. & SUZUKI, T. 2007b, The effect of fluorination on pentacene/gold interface energetics and charge reorganization energy. *Advanced Materials,* 19**,** 112-116.

[Koch, 2007c] KOCH, N., VOLLMER, A. & ELSCHNER, A. 2007c, Influence of water on the work function of conducting poly(3,4-ethylenedioxythiophene)/poly(styrenesulfonate). *Applied Physics*

Letters, 90**,** -.

[Koch, 2007d] KOCH, N., VOLLMER, A. & ELSCHNER, A. 2007d, Influence of water on the work function of conducting poly(3,4-ethylenedioxythiophene)/poly(styrenesulfonate). *Applied Physics Letters,* 90**,** 043512.

[Koch, 2006] KOCH, N., VOLLMER, A., SALZMANN, I., NICKEL, B., WEISS, H. & RABE, J. P. 2006, Evidence for temperature-dependent electron band dispersion in pentacene. *Physical Review Letters,* 96**,** 156803.

[Koma, 1995] KOMA, A. 1995, Molecular beam epitaxial growth of organic thin films. *Progress in Crystal Growth and Characterization of Materials,* 30**,** 129-152.

[Koma, 1985] KOMA, A., SUNOUCHI, K. & MIYAJIMA, T. 1985, Fabrication of ultrathin heterostructures with van der waals epitaxy. *J. Vac. Sci.& Technol. B,* 3**,** 724-724.

[Koster, 2005] KOSTER, L. J. A., MIHAILETCHI, V. D., RAMAKER, R. & BLOM, P. W. M. 2005, Light intensity dependence of open-circuit voltage of polymer : fullerene solar cells. *Applied Physics Letters,* 86**,** 3.

[Kowarik, 2008a] KOWARIK, S., GERLACH, A., HINDERHOFER, A., MILITA, S., BORGATTI, F., ZONTONE, F., SUZUKI, T., BISCARINI, F. & SCHREIBER, F. 2008a, Structure, morphology, and growth dynamics of perfluoro-pentacene thin films. *Physica Status Solidi-Rapid Research Letters,* 2**,** 120-122.

[Kowarik, 2008b] KOWARIK, S., GERLACH, A. & SCHREIBER, F. 2008b, Organic molecular beam deposition: fundamentals, growth dynamics, and in situ studies. *Journal of Physics-Condensed Matter,* 20**,** 12.

[Kowarik, 2009] KOWARIK, S., GERLACH, A., SELLNER, S., CAVALCANTI, L., KONOVALOV, O. & SCHREIBER, F. 2009, Real-time X-ray diffraction measurements of structural dynamics and polymorphism in diindenoperylene growth. *Applied Physics A,* 95**,** 233-239.

[Kowarik, 2006] KOWARIK, S., GERLACH, A., SELLNER, S., SCHREIBER, F., CAVALCANTI, L. & KONOVALOV, O. 2006, Real-time observation of structural and orientational transitions during growth of organic thin films. *Phys. Rev. Lett.,* 96**,** 125504.

[Krellner, 2007] KRELLNER, C., HAAS, S., GOLDMANN, C., PERNSTICH, K. P., GUNDLACH, D. J. & BATLOGG, B. 2007, Density of bulk trap states in organic semiconductor crystals: Discrete levels induced by oxygen in rubrene. *Physical Review B,* 75**,** 245115.

[Kroto, 1985] KROTO, H. W., KROTO, H. W., O'BRIEN, S. C., CURL, R. F. & SMALLEY, R. E. 1985, C60: Buckminsterfullerene. *Nature* 318.

[Kurrle, 2008] KURRLE, D. & PFLAUM, J. 2008, Exciton diffusion length in the organic semiconductor diindenoperylene. *Applied Physics Letters,* 92**,** 133306.

[Landau, 1933] LANDAU, L. D. 1933, Electron motion in crystal lattices. *Phys. Z. Sowjet.,* 3**,** 664.

[Langevin, 1903] LANGEVIN, P. 1903, The recombination and mobilities of ions in gases. *Annales De Chimie Et De Physique,* 28**,** 433-530.

[Lawrence, 1988] LAWRENCE, C. J. 1988, The mechanics of spin coating of polymer films. *Physics of Fluids (1958-1988),* 31**,** 2786-2795.

[Li, 2007] LI, Z. Q., PODZOROV, V., SAI, N., MARTIN, M. C., GERSHENSON, M. E., DI VENTRA, M. & BASOV, D. N. 2007, Light quasiparticles dominate electronic transport in molecular crystal field-effect transistors. *Phys. Rev. Lett.,* 99.

[Lintymer, 2003] LINTYMER, J., GAVOILLE, J., MARTIN, N. & TAKADOUM, J. 2003, Glancing angle deposition to modify microstructure and properties of sputter deposited chromium thin films. *Surface & Coatings Technology,* 174**,** 316-323.

[Lo, 2010] LO, M. F., NG, T. W., LAI, S. L., WONG, F. L., FUNG, M. K., LEE, S. T. & LEE, C. S. 2010, Operation stability enhancement in organic photovoltaic device by a metal doped organic exciton blocking layer. *Applied Physics Letters,* 97**,** 3.

[Lo, 2013] LO, M. F., NG, T. W., MO, H. W. & LEE, C. S. 2013, Direct Threat of a UV-Ozone Treated Indium-Tin-Oxide Substrate to the Stabilities of Common Organic Semiconductors. *Advanced Functional Materials,* 23**,** 1718-1723.

[Lu, 2013] LU, G., BLAKESLEY, J., HIMMELBERGER, S., PINGEL, P., FRISCH, J., LIEBERWIRTH, I., SALZMANN, I., OEHZELT, M., DI PIETRO, R., SALLEO, A., KOCH, N. & NEHER, D. 2013, Moderate doping leads to high performance of semiconductor/insulator polymer blend transistors. *Nat Commun,* 4**,** 1588.

[Lunt, 2009] LUNT, R. R., GIEBINK, N. C., BELAK, A. A., BENZIGER, J. B. & FORREST, S. R. 2009, Exciton diffusion lengths of organic semiconductor thin films measured by spectrally resolved photoluminescence quenching. *J. Appl. Phys.,* 105**,** -.

[Lunt, 2011] LUNT, R. R., OSEDACH, T. P., BROWN, P. R., ROWEHL, J. A. & BULOVIC, V. 2011, Practical roadmap and limits to nanostructured photovoltaics. *Adv Mater,* 23**,** 5712-27.

[Lüssem, 2013] LÜSSEM, B., RIEDE, M. & LEO, K. 2013, Doping of organic semiconductors. *physica status solidi (a),* 210**,** 9-43.

[Ma, 2005] MA, W., YANG, C., GONG, X., LEE, K. & HEEGER, A. J. 2005, Thermally Stable, Efficient Polymer Solar Cells with Nanoscale Control of the Interpenetrating Network Morphology. *Adv. Funct. Mater.,* 15**,** 1617-1622.

[Maennig, 2001] MAENNIG, B., PFEIFFER, M., NOLLAU, A., ZHOU, X., LEO, K. & SIMON, P. 2001, Controlled p-type doping of polycrystalline and amorphous organic layers: Self-consistent description of conductivity and field-effect mobility by a microscopic percolation model. *Physical Review B,* 64**,** art. no.-195208.

[Marcus, 1993] MARCUS, R. A. 1993, Electron transfer reactions in chemistry. Theory and experiment. *Reviews of Modern Physics,* 65**,** 599-610.

[Mas-Torrent, 2004] MAS-TORRENT, M., HADLEY, P., BROMLEY, S. T., RIBAS, X., TARRÉS, J., MAS, M., MOLINS, E., VECIANA, J. & ROVIRA, C. 2004, Correlation between crystal structure and mobility in organic field-effect transistors based on single crystals of tetrathiafulvalene derivatives. *Journal of the American Chemical Society,* 126**,** 8546-8553.

[Masahiko, 1989] MASAHIKO, H., HIROYUKI, S., AKIRA, Y. & ANTHONY, F. G. 1989, Epitaxial growth of organic thin films by organic molecular beam epitaxy. *Japanese Journal of Applied Physics,* 28**,** L306.

[Masumoto, 2008] MASUMOTO, Y. & MORI, T. 2008, Application of organic bathocuproine-based alloy film to organic light-emitting diodes. *Thin Solid Films,* 516**,** 3350-3356.

[Meerheim, 2006] MEERHEIM, R., WALZER, K., PFEIFFER, M. & LEO, K. 2006, Ultrastable and efficient red organic light emitting diodes with doped transport layers. *Applied Physics Letters,* 89**,** -.

[Meiss, 2010] MEISS, J., HUMMERT, M., ZIEHLKE, H., LEO, K. & RIEDE, M. 2010, Organic solar cells with very high fill factor and voltage using tetrapropyl-tetraphenyl-diindenoperylene as green

donor. *physica status solidi (RRL) - Rapid Research Letters,* 4**,** 329-331.

[Melzer, 2004] MELZER, C., KOOP, E. J., MIHAILETCHI, V. D. & BLOM, P. W. M. 2004, Hole Transport in Poly(phenylene vinylene)/Methanofullerene Bulk-Heterojunction Solar Cells. *Advanced Functional Materials,* 14**,** 865-870.

[Mendez, 2013] MENDEZ, H., HEIMEL, G., OPITZ, A., SAUER, K., BARKOWSKI, P., OEHZELT, M., SOEDA, J., OKAMOTO, T., TAKEYA, J., ARLIN, J. B., BALANDIER, J. Y., GEERTS, Y., KOCH, N. & SALZMANN, I. 2013, Doping of organic semiconductors: impact of dopant strength and electronic coupling. *Angew Chem Int Ed Engl,* 52**,** 7751-5.

[Menke, 2014] MENKE, S. M. & HOLMES, R. J. 2014, Exciton diffusion in organic photovoltaic cells. *Energy Environ. Sci.,* 7**,** 469-469.

[Messier, 1997] MESSIER, R. 1997, Engineered sculptured nematic thin films. *J. Vac. Sci. & Technolog. A: Vac., Surf., and Films,* 15**,** 2148.

[Meyer zu Heringdorf, 2001a] MEYER ZU HERINGDORF, F.-J., REUTER, M. C. & TROMP, R. M. 2001a, Growth dynamics of pentacene thin films. 412.

[Meyer zu Heringdorf, 2001b] MEYER ZU HERINGDORF, F.-J., REUTER, M. C. & TROMP, R. M. 2001b, Growth dynamics of pentacene thin films. *Nature,* 412**,** 517-520.

[Meyerhofer, 1978] MEYERHOFER, D. 1978, Characteristics of resist films produced by spinning. *J. Appl. Phys.,* 49**,** 3993-3997.

[Mihailetchi, 2004] MIHAILETCHI, V. D., KOSTER, L. J. A., HUMMELEN, J. C. & BLOM, P. W. M. 2004, Photocurrent generation in polymer-fullerene bulk heterojunctions. *Physical Review Letters,* 93**,** 216601.

[Miller, 1960] MILLER, A. & ABRAHAMS, E. 1960, Impurity conduction at low concentrations. *Phys. Rev.,* 120**,** 745-755.

[Mityashin, 2012] MITYASHIN, A., OLIVIER, Y., VAN REGEMORTER, T., ROLIN, C., VERLAAK, S., MARTINELLI, N. G., BELJONNE, D., CORNIL, J., GENOE, J. & HEREMANS, P. 2012, Unraveling the mechanism of molecular doping in organic semiconductors. *Adv Mater,* 24**,** 1535-9.

[Moses, 2006] MOSES, D., SOCI, C., CHI, X. & RAMIREZ, A. P. 2006, Mechanism of carrier photogeneration and carrier transport in molecular crystal tetracene. *Phys. Rev. Lett.,* 97.

[Nakhodkin, 1972] NAKHODKIN, N. G. & SHALDERVAN, A. I. 1972, Effect of vapor incidence angles on profile and properties of condensed films. *Thin Solid Films,* 10**,** 109-&.

[Nelson, 2003] NELSON, J. 2003. *The Physics of Solar Cells*, Imperial College Press.

[Nenashev, 2011] NENASHEV, A. V., BARANOVSKII, S. D., WIEMER, M., JANSSON, F., ÖSTERBACKA, R., DVURECHENSKII, A. V. & GEBHARD, F. 2011, Theory of exciton dissociation at the interface between a conjugated polymer and an electron acceptor. *Physical Review B,* 84**,** 035210.

[Nicolai, 2012] NICOLAI, H. T., KUIK, M., WETZELAER, G. A. H., DE BOER, B., CAMPBELL, C., RISKO, C., BRÉDAS, J. L. & BLOM, P. W. M. 2012, Unification of trap-limited electron transport in semiconducting polymers. *Nat Mater,* 11**,** 882-887.

[Niederhausen, 2012] NIEDERHAUSEN, J., AMSALEM, P., WILKE, A., SCHLESINGER, R., WINKLER, S., VOLLMER, A., RABE, J. P. & KOCH, N. 2012, Doping of C-60 (sub)monolayers by Fermi-level pinning induced electron transfer. *Physical Review B,* 86**,** 5.

[Nieuwenh.Jm, 1966] NIEUWENH.JM & HAANSTRA, H. B. 1966, Microfractography of thin films. *Philips Tech. Rev.,* 27**,** 87.

[Nilsson, 2007] NILSSON, S., BERNASIK, A., BUDKOWSKI, A. & MOONS, E. 2007, Morphology and Phase Segregation of Spin-Casted Films of Polyfluorene/PCBM Blends. *Macromolecules,* 40**,** 8291-8301.

[Nollau, 2000a] NOLLAU, A., PFEIFFER, M., FRITZ, T. & LEO, K. 2000a, Controlled n-type doping of a molecular organic semiconductor: Naphthalenetetracarboxylic dianhydride (NTCDA) doped with bis(ethylenedithio)-tetrathiafulvalene (BEDT-TTF). *Journal of Applied Physics,* 87**,** 4340-4343.

[Nollau, 2000b] NOLLAU, A., PFEIFFER, M., FRITZ, T. & LEO, K. 2000b, Controlled n-type doping of a molecular organic semiconductor: Naphthalenetetracarboxylic dianhydride (NTCDA) doped with bis(ethylenedithio)-tetrathiafulvalene (BEDT-TTF). *J. Appl. Phys.,* 87**,** 4340-4343.

[Noriega, 2013] NORIEGA, R., RIVNAY, J., VANDEWAL, K., KOCH, F. P., STINGELIN, N., SMITH, P., TONEY, M. F. & SALLEO, A. 2013, A general relationship between disorder, aggregation and charge transport in conjugated polymers. *Nat Mater,* 12**,** 1038-44.

[Oh, 2011] OH, J. Y., JANG, W. S., LEE, T. I., MYOUNG, J.-M. & BAIK, H. K. 2011, Driving vertical phase separation in a bulk-heterojunction by inserting a poly(3-hexylthiophene) layer for highly efficient organic solar cells. *Applied Physics Letters,* 98**,** 023303.

[Olthof, 2012] OLTHOF, S., MEHRAEEN, S., MOHAPATRA, S. K., BARLOW, S., COROPCEANU, V., BRÉDAS, J.-L., MARDER, S. R. & KAHN, A. 2012, Ultralow Doping in Organic Semiconductors: Evidence of Trap Filling. *Physical Review Letters,* 109.

[Onsager, 1938] ONSAGER, L. 1938, Initial Recombination of Ions. *Phys. Rev.,* 54**,** 554-557.

[Opitz, 2010a] OPITZ, A., WAGNER, J., BRU, X, TTING, W., SALZMANN, I., KOCH, N., MANARA, J., PFLAUM, J., HINDERHOFER, A. & SCHREIBER, F. 2010a, Charge Separation at Molecular Donor–Acceptor Interfaces: Correlation Between Morphology and Solar Cell Performance. *Selected Topics in Quantum Electronics, IEEE Journal of,* 16**,** 1707-1717.

[Opitz, 2010b] OPITZ, A., WAGNER, J., BRÜTTING, W., SALZMANN, I., KOCH, N., MANARA, J., PFLAUM, J., HINDERHOFER, A. & SCHREIBER, F. 2010b, Charge separation at molecular donor–acceptor interfaces: correlation between morphology and solar cell performance. *J. Select. Topics Quantum Electron.,* 16**,** 1707.

[Ostroverkhova, 2006] OSTROVERKHOVA, O., COOKE, D. G., HEGMANN, F. A., ANTHONY, J. E., PODZOROV, V., GERSHENSON, M. E., JURCHESCU, O. D. & PALSTRA, T. T. M. 2006, Ultrafast carrier dynamics in pentacene, functionalized pentacene, tetracene, and rubrene single crystals. *Applied Physics Letters,* 88**,** -.

[Parthasarathy, 2001] PARTHASARATHY, G., SHEN, C., KAHN, A. & FORREST, S. R. 2001, Lithium doping of semiconducting organic charge transport materials. *Journal of Applied Physics,* 89**,** 4986.

[Peumans, 2000] PEUMANS, P., BULOVIC, V. & FORREST, S. R. 2000, Efficient photon harvesting at high optical intensities in ultrathin organic double-heterostructure photovoltaic diodes. *Applied Physics Letters,* 76**,** 2650-2652.

[Peumans, 2004] PEUMANS, P. & FORREST, S. R. 2004, Separation of geminate charge-pairs at donor–acceptor interfaces in disordered solids. *Chemical Physics Letters,* 398**,** 27-31.

[Peumans, 2003a] PEUMANS, P., UCHIDA, S. & FORREST, S. R. 2003a, Efficient bulk heterojunction photovoltaic cells using small-molecular-weight organic thin films. *Nature,* 425**,** 158-162.

[Peumans, 2003b] PEUMANS, P., UCHIDA, S. & FORREST, S. R. 2003b, Efficient bulk heterojunction

photovoltaic cells using small-molecular-weight organic thin films. *Nature,* 425**,** 158-162.

[Pfeiffer, 1998] PFEIFFER, M., BEYER, A., FRITZ, T. & LEO, K. 1998, Controlled doping of phthalocyanine layers by cosublimation with acceptor molecules: A systematic Seebeck and conductivity study. *Applied Physics Letters,* 73**,** 3202-3204.

[Pfuetzner, 2011] PFUETZNER, S., MICKEL, C., JANKOWSKI, J., HEIN, M., MEISS, J., SCHUENEMANN, C., ELSCHNER, C., LEVIN, A. A., RELLINGHAUS, B., LEO, K. & RIEDE, M. 2011, The influence of substrate heating on morphology and layer growth in C-60:ZnPc bulk heterojunction solar cells. *Organic Electronics,* 12**,** 435-441.

[Pimpinelli, 1998] PIMPINELLI, A. & VILLAIN, J. 1998. *Physics of Crystal Growth*, Cambridge University Press.

[Pingel, 2013] PINGEL, P. & NEHER, D. 2013, Comprehensive picture of p-type doping of P3HT with the molecular acceptor F_{4}TCNQ. *Physical Review B,* 87.

[Pingel, 2012] PINGEL, P., SCHWARZL, R. & NEHER, D. 2012, Effect of molecular p-doping on hole density and mobility in poly(3-hexylthiophene). *Applied Physics Letters,* 100.

[Pingel, 2010] PINGEL, P., ZHU, L. Y., PARK, K. S., VOGEL, J. O., JANIETZ, S., KIM, E. G., RABE, J. P., BREDAS, J. L. & KOCH, N. 2010, Charge-Transfer Localization in Molecularly Doped Thiophene-Based Donor Polymers. *Journal of Physical Chemistry Letters,* 1**,** 2037-2041.

[Potscavage, 2008] POTSCAVAGE, W. J., YOO, S. & KIPPELEN, B. 2008, Origin of the open-circuit voltage in multilayer heterojunction organic solar cells. *Applied Physics Letters,* 93**,** 193308.

[Powell, 1975] POWELL, R. C. & SOOS, Z. G. 1975, Singlet exciton energy transfer in organic solids. *Journal of Luminescence,* 11**,** 1-45.

[Ramsdale, 2002] RAMSDALE, C. M., BARKER, J. A., ARIAS, A. C., MACKENZIE, J. D., FRIEND, R. H. & GREENHAM, N. C. 2002, The origin of the open-circuit voltage in polyfluorene-based photovoltaic devices. *Journal of Applied Physics,* 92**,** 4266-4270.

[Reddy, 2009] REDDY, V. S., KARAK, S., RAY, S. K. & DHAR, A. 2009, Photovoltaic properties of pentacene/[6,6]-phenyl C61 butyric acid methyl ester based bilayer hetero-junction solar cells. *Journal of Physics D: Applied Physics,* 42.

[Reimer, 1998] REIMER, L. 1998. *Scanning electron microscopy: Physics of image formation and microanalysis,* Berlin Heidelberg New York, Springer-Verlag.

[Reineke, 2009] REINEKE, S., LINDNER, F., SCHWARTZ, G., SEIDLER, N., WALZER, K., LUSSEM, B. & LEO, K. 2009, White organic light-emitting diodes with fluorescent tube efficiency. *Nature,* 459**,** 234-U116.

[Rentenberger, 2006] RENTENBERGER, S., VOLLMER, A., ZOJER, E., SCHENNACH, R. & KOCH, N. 2006, UV／ozone treated Au for air-stable, low hole injection barrier electrodes in organic electronics. *Journal of Applied Physics,* 100**,** -.

[Riede, 2008] RIEDE, M., MUELLER, T., TRESS, W., SCHUEPPEL, R. & LEO, K. 2008, Small-molecule solar cells-status and perspectives. *Nanotechnology,* 19**,** 424001.

[Rivnay, 2011] RIVNAY, J., NORIEGA, R., NORTHRUP, J. E., KLINE, R. J., TONEY, M. F. & SALLEO, A. 2011, Structural origin of gap states in semicrystalline polymers and the implications for charge transport. *Physical Review B,* 83**,** 121306.

[Robbie, 1995] ROBBIE, K. 1995, Fabrication of thin films with highly porous microstructures. *J. Vac. Sci. & Technolog. A: Vac., Surf., and Films,* 13**,** 1032.

[Robbie, 1997] ROBBIE, K. & BRETT, M. J. 1997, Sculptured thin films and glancing angle deposition: Growth mechanics and applications. *J. Vac. Sci. Technol. A,* 15**,** 1460-1465.

[Robbie, 1996] ROBBIE, K., BRETT, M. J. & LAKHTAKIA, A. 1996, Chiral sculptured thin films. *Nature Mater.,* 384.

[Rubel, 2008] RUBEL, O., BARANOVSKII, S. D., STOLZ, W. & GEBHARD, F. 2008, Exact solution for hopping dissociation of geminate electron-hole pairs in a disordered chain. *Physical Review Letters,* 100**,** 196602.

[Ruiz, 2003a] RUIZ, R., NICKEL, B., KOCH, N., FELDMAN, L. C., HAGLUND, R. F., KAHN, A., FAMILY, F. & SCOLES, G. 2003a, Dynamic scaling, island size distribution, and morphology in the aggregation regime of submonolayer pentacene films. *Physical Review Letters,* 91**,** 136102.

[Ruiz, 2003b] RUIZ, R., NICKEL, B., KOCH, N., FELDMAN, L. C., HAGLUND, R. F., KAHN, A. & SCOLES, G. 2003b, Pentacene ultrathin film formation on reduced and oxidized Si surfaces. *Physical Review B,* 67**,** 125406.

[Salzmann, 2008] SALZMANN, I., DUHM, S., OPITZ, R., JOHNSON, R. L., RABE, J. P. & KOCH, N. 2008, Structural and electronic properties of pentacene-fullerene heterojunctions. *J. Appl. Phys.,* 104**,** -.

[Salzmann, 2012a] SALZMANN, I., HEIMEL, G., DUHM, S., OEHZELT, M., PINGEL, P., GEORGE, B. M., SCHNEGG, A., LIPS, K., BLUM, R. P., VOLLMER, A. & KOCH, N. 2012a, Intermolecular Hybridization Governs Molecular Electrical Doping. *Physical Review Letters,* 108.

[Salzmann, 2012b] SALZMANN, I., MOSER, A., OEHZELT, M., BREUER, T., FENG, X., JUANG, Z.-Y., NABOK, D., DELLA VALLE, R. G., DUHM, S., HEIMEL, G., BRILLANTE, A., VENUTI, E., BILOTTI, I., CHRISTODOULOU, C., FRISCH, J., PUSCHNIG, P., DRAXL, C., WITTE, G., MÜLLEN, K. & KOCH, N. 2012b, Epitaxial growth of π-stacked perfluoropentacene on graphene-coated quartz. *ACS Nano,* 6**,** 10874-10883.

[Sano, 1979] SANO, H. & TACHIYA, M. 1979, Partially diffusion‐controlled recombination. *J. Chem. phys.,* 71**,** 1276-1282.

[Sariciftci, 1993] SARICIFTCI, N. S., BRAUN, D., ZHANG, C., SRDANOV, V. I., HEEGER, A. J., STUCKY, G. & WUDL, F. 1993, Semiconducting polymer‐buckminsterfullerene heterojunctions: Diodes, photodiodes, and photovoltaic cells. *Appl. Phys. Lett.,* 62**,** 585-587.

[Sariciftci, 1992] SARICIFTCI, N. S., SMILOWITZ, L., HEEGER, A. J. & WUDL, F. 1992, Photoinduced electron transfer from a conducting polymer to buckminsterfullerene. *Science,* 258**,** 1474-1476.

[Schreiber, 2004] SCHREIBER, F. 2004, Organic molecular beam deposition: Growth studies beyond the first monolayer. *physica status solidi (a),* 201**,** 1037-1054.

[Schroder, 2006] SCHRODER, D. K. 2006. *Semiconductor Material and Device Characterization,3rd*, A John Wiley & Sons, Inc.

[Schuenemann, 2013] SCHUENEMANN, C., PETRICH, A., SCHULZE, R., WYNANDS, D., MEISS, J., HEIN, M. P., JANKOWSKI, J., ELSCHNER, C., ALEX, J., HUMMERT, M., EICHHORN, K.-J., LEO, K. & RIEDE, M. 2013, Diindenoperylene derivatives: A model to investigate the path from molecular structure via morphology to solar cell performance. *Org. Electron.,* 14**,** 1704-1714.

[Schwoerer, 2005] SCHWOERER, M. & WOLF, H. C. 2005. *Organic Molecular Solids,* Weinheim, Wiley-VCH Verlag GmbH&Co.

[Sen, 2008] SEN, S., BARDAKCI, B., YAVUZ, A. G. & GOK, A. U. 2008, Polyfuran/zeolite LTA composites and adsorption properties. *European Polymer Journal,* 44**,** 2708-2717.

[Senthilarasu, 2007] SENTHILARASU, S., HAHN, Y. B. & LEE, S. H. 2007, Structural analysis of zinc phthalocyanine (ZnPc) thin films: X-ray diffraction study. *Journal of Applied Physics,* 102**,** 6.

[Seungkeun, 2009] SEUNGKEUN, C., POTSCAVAGE JR, W. J. & BERNARD, K. 2009, Area-scaling of organic solar cells. *J. Appl. Phys.,* 106.

[Sheraw, 2003] SHERAW, C. D., JACKSON, T. N., EATON, D. L. & ANTHONY, J. E. 2003, Functionalized pentacene active layer organic thin-film transistors. *Advanced Materials,* 15**,** 2009-2011.

[Sirringhaus, 2003] SIRRINGHAUS, H. 2003, Organic semiconductors: An equal-opportunity conductor. *Nat. Mater.,* 2.

[Smith, 1960] SMITH, D. O., COHEN, M. S. & WEISS, G. P. 1960, Oblique-incident anisotropy in evaporated permalloy films. *J. Appl. Phys.,* 31**,** 1755-1762.

[Smith, 2010] SMITH, J., HAMILTON, R., MCCULLOCH, I., STINGELIN-STUTZMANN, N., HEENEY, M., BRADLEY, D. D. C. & ANTHOPOULOS, T. D. 2010, Solution-processed organic transistors based on semiconducting blends. *Journal of Materials Chemistry,* 20**,** 2562-2574.

[Snaith, 2002] SNAITH, H. J., ARIAS, A. C., MORTEANI, A. C., SILVA, C. & FRIEND, R. H. 2002, Charge generation kinetics and transport mechanisms in blended polyfluorene photovoltaic devices. *Nano Letters,* 2**,** 1353-1357.

[Snaith, 2006] SNAITH, H. J., SCHMIDT-MENDE, L., GRATZEL, M. & CHIESA, M. 2006, Light intensity, temperature, and thickness dependence of the open-circuit voltage in solid-state dye-sensitized solar cells. *Physical Review B,* 74**,** 6.

[Søndergaard, 2013] SØNDERGAARD, R. R., HÖSEL, M. & KREBS, F. C. 2013, Roll-to-roll fabrication of large area functional organic materials. *J. Polym. Sci., Part B: Polym. Phys.,* 51**,** 16-34.

[Steindamm, 2012] STEINDAMM, A., BRENDEL, M., TOPCZAK, A. K. & PFLAUM, J. 2012, Thickness dependent effects of an intermediate molecular blocking layer on the optoelectronic characteristics of organic bilayer photovoltaic cells. *Applied Physics Letters,* 101**,** -.

[Stübinger, 2001] STÜBINGER, T. & BRÜTTING, W. 2001, Exciton diffusion and optical interference in organic donor–acceptor photovoltaic cells. *J. Appl. Phys.,* 90**,** 3632.

[Sugiyama, 2000] SUGIYAMA, K., ISHII, H., OUCHI, Y. & SEKI, K. 2000, Dependence of indium-tin-oxide work function on surface cleaning method as studied by ultraviolet and x-ray photoemission spectroscopies. *Journal of Applied Physics,* 87**,** 295-298.

[Sukanek, 1985] SUKANEK, P. C. 1985, Spin coating. *Journal of Imaging Technology,* 11**,** 184-190.

[Sun, 2009] SUN, J., JUNG, B. J., LEE, T., BERGER, L., HUANG, J., LIU, Y., REICH, D. H. & KATZ, H. E. 2009, Tunability of mobility and conductivity over large ranges in poly(3,3'''-didodecylquaterthiophene)/insulating polymer composites. *ACS Appl Mater Interfaces,* 1**,** 412-9.

[Svensson, 2003] SVENSSON, M., ZHANG, F., VEENSTRA, S., VERHEES, W., HUMMELEN, J., KROON, J., INGANÄ, O. & ANDERSSON, M. 2003, High-performance polymer solar cells of an alternating polyfluorene copolymer and a fullerene derivative. *Adv. Mater.,* 15**,** 988.

[Sze, 1981] SZE, S. M. 1981. *Physics of semiconductor devices, 2nd ed.,* New York, Wiley.

[Sze, 2007] SZE, S. M. 2007. *Physics of Semiconductor Devices, 3rd,* New Jersey, John Wiley& Sons, Inc.

[Tait, 1993] TAIT, R. N., SMY, T. & BRETT, M. J. 1993, Modeling and characterizatioin of columnar

growth in evaporated-films. *Thin Solid Films,* 226**,** 196-201.

[Tang, 1979] TANG, C. W. 1979. Multilayer organic photovoltaic elements. US Patents.

[Tang, 1986] TANG, C. W. 1986, Two-layer organic photovoltaic cell. *Appl. Phys. Lett.,* 48**,** 183.

[Tang, 1975] TANG, C. W. & ALBRECHT, A. C. 1975, Photovoltaic effects of metal – chlorophyll - a – metal sandwich cells. *J. Chem. Phys.,* 62**,** 2139-2149.

[Terao, 2007] TERAO, Y., SASABE, H. & ADACHI, C. 2007, Correlation of hole mobility, exciton diffusion length, and solar cell characteristics in phthalocyanine/fullerene organic solar cells. *Applied Physics Letters,* 90**,** -.

[Thompson, 2008] THOMPSON, B. C. & FRECHET, J. M. J. 2008, Organic photovoltaics - Polymer-fullerene composite solar cells. *Angewandte Chemie-International Edition,* 47**,** 58-77.

[Torrance, 1980] TORRANCE, J. B., MAYERLE, J. J., BECHGAARD, K., SILVERMAN, B. D. & TOMKIEWICZ, Y. 1980, Comparison of 2 isostructural organic-compounds, one metallic and the other insulating. *Phys. Rev. B,* 22**,** 4960-4965.

[Tress, 2011a] TRESS, W., PETRICH, A., HUMMERT, M., HEIN, M., LEO, K. & RIEDE, M. 2011a, Imbalanced mobilities causing S-shaped IV curves in planar heterojunction organic solar cells. *Applied Physics Letters,* 98**,** -.

[Tress, 2011b] TRESS, W., PFUETZNER, S., LEO, K. & RIEDE, M. 2011b, Open circuit voltage and IV curve shape of ZnPc:C60 solar cells with varied mixing ratio and hole transport layer. *Journal of Photonics for Energy,* 1**,** 011114-011114-11.

[Tripathi, 2006] TRIPATHI, A. K. & PFLAUM, J. 2006, Correlation between ambipolar transport and structural phase transition in diindenoperylene single crystals. *Applied Physics Letters,* 89**,** -.

[Tunc, 2012] TUNC, A. V., DE SIO, A., RIEDEL, D., DESCHLER, F., DA COMO, E., PARISI, J. & VON HAUFF, E. 2012, Molecular doping of low-bandgap-polymer:fullerene solar cells: Effects on transport and solar cells. *Organic Electronics,* 13**,** 290-296.

[Turak, 2011] TURAK, A., NGUYEN, M., MAYE, F., HEIDKAMP, J., LIENERTH, P., WRACHTRUP, J. & DOSCH, H. 2011, Nanoscale engineering of exciton dissociating interfaces in organic photovoltaics. *J. Nano Res.,* 14.

[United Nations Environment Programme (UNEP)] UNITED NATIONS ENVIRONMENT PROGRAMME (UNEP), E. I. I. O. G. E. Y. B. <uyb_2013_new.pdf>.

[van der Drift, 1967] VAN DER DRIFT, A. 1967. *Evolutionary selection a principle governing growth orientation in vapour-deposition layers*, Philips Res. Rep.

[van der Holst, 2009] VAN DER HOLST, J. J. M., VAN OOST, F. W. A., COEHOORN, R. & BOBBERT, P. A. 2009, Electron-hole recombination in disordered organic semiconductors: Validity of the Langevin formula. *Phys. Rev. B,* 80**,** 235202.

[Van Dijken, 2011] VAN DIJKEN, J. G., FLEISCHAUER, M. D. & BRETT, M. J. 2011, Controlled nanostructuring of CuPc thin films via glancing angle deposition for idealized organic photovoltaic architectures. *J. Mater. Chem.,* 21**,** 1013-1019.

[Vandewal, 2009] VANDEWAL, K., TVINGSTEDT, K., GADISA, A., INGANAS, O. & MANCA, J. V. 2009, On the origin of the open-circuit voltage of polymer-fullerene solar cells. *Nature Materials,* 8**,** 904-909.

[Venables, 1984] VENABLES, J. A., SPILLER, G. D. T. & HANBUCKEN, M. 1984, Nucleation and growth of

thin films. *Reports on Progress in Physics,* 47**,** 399.

[Vogel, 2006a] VOGEL, M., DOKA, S., BREYER, C., LUX-STEINER, M. C. & FOSTIROPOULOS, K. 2006a, On the function of a bathocuproine buffer layer in organic photovoltaic cells. *Applied Physics Letters,* 89**,** 163501.

[Vogel, 2006b] VOGEL, M., DOKA, S., BREYER, C., LUX-STEINER, M. C. & FOSTIROPOULOS, K. 2006b, On the function of a bathocuproine buffer layer in organic photovoltaic cells. *Applied Physics Letters,* 89**,** -.

[Volmer, 1921] VOLMER, M. 1921, Crystal formation by directed steam molecules. *Zeitschrift Fur Physik,* 5**,** 31-34.

[Wagner, 2010] WAGNER, J., GRUBER, M., HINDERHOFER, A., WILKE, A., BRÖKER, B., FRISCH, J., AMSALEM, P., VOLLMER, A., OPITZ, A., KOCH, N., SCHREIBER, F. & BRÜTTING, W. 2010, High fill factor and open circuit voltage in organic photovoltaic cells with diindenoperylene as donor material. *Adv. Funct. Mater.,* 20**,** 4295-4303.

[Wagner, 2012] WAGNER, J., GRUBER, M., WILKE, A., TANAKA, Y., TOPCZAK, K., STEINDAMM, A., HÖRMANN, U., OPITZ, A., NAKAYAMA, Y., ISHII, H., PFLAUM, J., KOCH, N. & BRÜTTING, W. 2012, Identification of different origins for s-shaped current voltage characteristics in planar heterojunction organic solar cells. *J. Appl. Phys.,* 111**,** 054509.

[Walzer, 2007] WALZER, K., MAENNIG, B., PFEIFFER, M. & LEO, K. 2007, Highly Efficient Organic Devices Based on Electrically Doped Transport Layers. *Chemical Reviews,* 107**,** 1233-1271.

[Wang, 2006] WANG, S. D., KANAI, K., OUCHI, Y. & SEKI, K. 2006, Bottom contact ambipolar organic thin film transistor and organic inverter based on C60/pentacene heterostructure. *Organic Electronics,* 7**,** 457-464.

[Wannier, 1937] WANNIER, G. H. 1937, The Structure of Electronic Excitation Levels in Insulating Crystals. *Phys. Rev.,* 52**,** 191-197.

[Warta, 1985] WARTA, W. & KARL, N. 1985, Hot holes in naphthalene: High, electric-field-dependent mobilities. *Phys. Rev. B,* 32**,** 1172-1182.

[Wilke, 2013] WILKE, A. 2013, *Electronic properties of interfaces in molecular organic photovoltaic cells.* Ph.D., Humboldt-Universität zu Berlin.

[Wilke, 2011] WILKE, A., AMSALEM, P., FRISCH, J., BRÖKER, B., VOLLMER, A. & KOCH, N. 2011, Electric fields induced by energy level pinning at organic heterojunctions. *Applied Physics Letters,* 98**,** 123304.

[Wilke, 2012] WILKE, A., ENDRES, J., HORMANN, U., NIEDERHAUSEN, J., SCHLESINGER, R., FRISCH, J., AMSALEM, P., WAGNER, J., GRUBER, M., OPITZ, A., VOLLMER, A., BRUTTING, W., KAHN, A. & KOCH, N. 2012, Correlation between interface energetics and open circuit voltage in organic photovoltaic cells. *Applied Physics Letters,* 101.

[Witte, 2005] WITTE, G., LUKAS, S., BAGUS, P. S. & WÖLL, C. 2005, Vacuum level alignment at organic/metal junctions: “Cushion” effect and the interface dipole. *Applied Physics Letters,* 87**,** -.

[Witten, 1981] WITTEN, T. A. & SANDER, L. M. 1981, Diffusion-limited aggregation, a kinetic critical phenomenon. *Phys. Rev. Lett.,* 47**,** 1400-1403.

[Wojcik, 2009] WOJCIK, M. & TACHIYA, M. 2009, Accuracies of the empirical theories of the escape probability based on Eigen model and Braun model compared with the exact extension of

Onsager theory. *The Journal of Chemical Physics,* 130**,** -.

[Xiao, 2013] XIAO, X., ZIMMERMAN, J. D., LASSITER, B. E., BERGEMANN, K. J. & FORREST, S. R. 2013, A hybrid planar-mixed tetraphenyldibenzoperiflanthene/C70 photovoltaic cell. *Applied Physics Letters,* 102**,** -.

[Yamamoto, 1979] YAMAMOTO, Y., YOSHINO, K. & INUISHI, Y. 1979, Electrical-properties of phthalocyanine halogen complexes. *J. Phys. Soc. Japan,* 47**,** 1887-1891.

[Yang, 2004] YANG, F., SHTEIN, M. & FORREST, S. R. 2004, Controlled growth of a molecular bulk heterojunction photovoltaic cell. *Nature Mater.,* 4**,** 37-41.

[Yang, 2005] YANG, F., SHTEIN, M. & FORREST, S. R. 2005, Controlled growth of a molecular bulk heterojunction photovoltaic cell. *Nature Materials,* 4**,** 37-41.

[Yim, 2008] YIM, K.-H., WHITING, G. L., MURPHY, C. E., HALLS, J. J. M., BURROUGHES, J. H., FRIEND, R. H. & KIM, J.-S. 2008, Controlling Electrical Properties of Conjugated Polymers via a Solution-Based p-Type Doping. *Advanced Materials,* 20**,** 3319-3324.

[You, 2013a] YOU, J., CHEN, C. C., HONG, Z., YOSHIMURA, K., OHYA, K., XU, R., YE, S., GAO, J., LI, G. & YANG, Y. 2013a, 10.2% power conversion efficiency polymer tandem solar cells consisting of two identical sub-cells. *Adv. Mater.,* 25**,** 3973-8.

[You, 2013b] YOU, J., DOU, L., YOSHIMURA, K., KATO, T., OHYA, K., MORIARTY, T., EMERY, K., CHEN, C. C., GAO, J., LI, G. & YANG, Y. 2013b, A polymer tandem solar cell with 10.6% power conversion efficiency. *Nat Commun,* 4**,** 1446.

[Yu, 1995] YU, G., GAO, J., HUMMELEN, J. C., WUDL, F. & HEEGER, A. J. 1995, Polymer photovoltaic cells: Enhanced efficiencies via a network of internal donor-acceptor heterojunctions. *Science,* 270**,** 1789-1791.

[Yu, 2011] YU, S. W., KLIMM, C., SCHÄFER, P., RABE, J. P., RECH, B. & KOCH, N. 2011, Organic photovoltaic cells with interdigitated structures based on pentacene nanocolumn arrays. *Org. Electron.,* 12**,** 2180-2184.

[Zade, 2006] ZADE, S. S. & BENDIKOV, M. 2006, From oligomers to polymer: Convergence in the HOMO-LUMO gaps of conjugated oligomers. *Organic Letters,* 8**,** 5243-5246.

[Zen, 2004] ZEN, A., PFLAUM, J., HIRSCHMANN, S., ZHUANG, W., JAISER, F., ASAWAPIROM, U., RABE, J. P., SCHERF, U. & NEHER, D. 2004, Effect of molecular weight and annealing of poly(3-hexylthiophene)s on the performance of organic field-effect transistors. *Advanced Functional Materials,* 14**,** 757-764.

[Zeng, 2010] ZENG, W. J., YONG, K. S., KAM, Z. M., ZHU, F. R. & LI, Y. N. 2010, Effect of blend layer morphology on performance of ZnPc: C-60-based photovoltaic cells. *Applied Physics Letters,* 97**,** 3.

[Zhang, 2006] ZHANG, F., MAMMO, W., ANDERSSON, L. M., ADMASSIE, S., ANDERSSON, M. R. & INGANÄS, O. 2006, Low-bandgap alternating fluorene copolymer/methanofullerene heterojunctions in efficient near-infrared polymer solar cells. *Adv. Mater.,* 18**,** 2169-2173.

[Zhang, 2007a] ZHANG, J., SALZMANN, I., ROGASCHEWSKI, S., RABE, J. P., KOCH, N., ZHANG, F. & XU, Z. 2007a, Arrays of crystalline C60 and pentacene nanocolumns. *Appl. Phys. Lett.,* 90**,** 193117.

[Zhang, 2007b] ZHANG, J., SALZMANN, I., ROGASCHEWSKI, S., RABE, J. P., KOCH, N., ZHANG, F. & XU, Z. 2007b, Arrays of crystalline C60 and pentacene nanocolumns. *Applied Physics Letters,* 90**,** -.

[Zhang, 2010] ZHANG, Y. & BLOM, P. W. M. 2010, Enhancement of the hole injection into regioregular

poly(3-hexylthiophene) by molecular doping. *Applied Physics Letters,* 97**,** 083303.

[Zhang, 2009] ZHANG, Y., DE BOER, B. & BLOM, P. W. M. 2009, Controllable Molecular Doping and Charge Transport in Solution-Processed Polymer Semiconducting Layers. *Advanced Functional Materials,* 19**,** 1901-1905.

[Zhao, 2002] ZHAO, Y. P., YE, D. X., WANG, G. C. & LU, T. M. 2002, Novel nano-column and nano-flower arrays by glancing angle deposition. *Nano lett.,* 2**,** 351-354.

[Zheng, 2009a] ZHENG, Y., BEKELE, R., OUYANG, J. & XUE, J. 2009a, Organic photovoltaic cells with vertically aligned crystalline molecular nanorods. *Organic Electronics,* 10**,** 1621-1625.

[Zheng, 2009b] ZHENG, Y., BEKELE, R., OUYANG, J. M. & XUE, J. G. 2009b, Organic photovoltaic cells with vertically aligned crystalline molecular nanorods. *Org. Electron.,* 10**,** 1621-1625.

[Zhou, 2002] ZHOU, X., PFEIFFER, M., HUANG, J. S., BLOCHWITZ-NIMOTH, J., QIN, D. S., WERNER, A., DRECHSEL, J., MAENNIG, B. & LEO, K. 2002, Low-voltage inverted transparent vacuum deposited organic light-emitting diodes using electrical doping. *Applied Physics Letters,* 81**,** 922-924.

[Zhou, 2012] ZHOU, Y., TAIMA, T., MIYADERA, T., YAMANARI, T., KITAMURA, M., NAKATSU, K. & YOSHIDA, Y. 2012, Glancing angle deposition of copper iodide nanocrystals for efficient organic photovoltaics. *Nano Lett.,* 12**,** 4146-4152.

[Zhu, 2009] ZHU, X. Y., YANG, Q. & MUNTWILER, M. 2009, Charge-transfer excitons at organic semiconductor surfaces and interfaces. *Accounts of Chemical Research,* 42**,** 1779-1787.

[Ziroff, 2010] ZIROFF, J., FORSTER, F., SCHÖLL, A., PUSCHNIG, P. & REINERT, F. 2010, Hybridization of organic molecular orbitals with substrate states at interfaces: PTCDA on silver. *Physical Review Letters,* 104**,** 233004.

Selbstständigkeitserklärung

Hiermit erkläre ich eidesstatlich, dass ich die Dissertation selbständig und nur unter Verwendung der angegebenen Hilfen und Zitate angefertigt zu haben.
Desweiteren besitze ich keinen weiteren Doktortitel und habe mich nicht anderweitig um einen weiteren Doktortitel beworben.
Ferner erkläre ich, dass ich die Promotionsordnung der Mathematisch-Naturwissenschaftlichen Fakultät I der Humboldt-Universität gelesen und zur Kenntnis genommen habe.

Shuwen Yu
Berlin, 3.09.2014